UNIVERSITÀ
DEGLI STUDI
FIRENZE

*Università degli Studi di Firenze*
*Scuola di Ingegneria*
*DIEF* - Department of Industrial Engineering

PhD School: *Energetica e Tecnologie Industrali ed Ambientali Innovative*
Scientific Area: ING-IND/08 - *Macchine a Fluido*

# Investigation of the Aero-Thermal Aspects of Combustor/Turbine Interaction in Gas Turbines

**PhD Candidate**: Ing. Massimiliano Insinna

**Tutor**: Prof. Ing. Francesco Martelli

**Co-Tutor**: Dr. Ing. Simone Salvadori

**Advisor**: Prof. Ing. Franz Heitmeir

**PhD Course Coordinator**: Prof. Ing. Maurizio De Lucia

XXVII PhD School Cycle - 2012-2014

*Alla mia Famiglia*

# Acknowledgements

I wish to thank Prof. Francesco Martelli for having supported my PhD activity and for the precious suggestions provided during all the research period. I would like to express sincere thanks to Dr. Simone Salvadori, whose continuous support has been fundamental for reaching the results presented in this work. Moreover, I wish to thank Prof. Franz Heitmeir for revising the manuscript and for the useful advices provided.

Special thanks go to Eng. Duccio Griffini with whom I have collaborated for obtaining some of the results presented in this thesis. Moreover, Dr. Alessandro Mattana, Dr. Alessandro Cappelletti, Dr. Adriano Spadi, Dr. Alessandro Marini, Dr. Chiara Bernardini, Eng. Stefano Vagnoli and all the other members of the "TCR" research group of the Department of Industrial Engineering of the University of Florence are sincerely acknowledged for the help and friendship demonstrated in all these years.

*Quel giorno, non so proprio perchè, decisi di andare a correre un po'. Perciò corsi fino alla fine della strada. E una volta lì pensai di correre fino la fine della città. E una volta lì pensai di correre attraverso la contea di Greenbow. Poi mi dissi: visto che sono arrivato fino a qui, tanto vale correre attraverso il bellissimo stato dell' Alabama, e così feci. Corsi attraverso tutta l'Alabama. E non so proprio perchè, continuai ad andare. Corsi fino all' oceano. E una volta lì mi dissi: visto che sono arrivato fino a qui, tanto vale girarmi e continuare a correre. Quando arrivai ad un altro oceano mi dissi: visto che sono arrivato fino a qui, tanto vale girarmi di nuovo e continuare a correre ...*

*Forrest Gump*

# Abstract

Lean-burn combustion technology has been identified to be the key methodology for gas turbine combustion systems to achieve legislative requirements for $NO_x$ emissions. Currently it is a mature technology in the power generation field but is still on development for aero engines. Combustors on which this type of combustion is implemented are characterized, in general, by high swirl numbers to provide adequate flame stabilization and strong reduction, or total absence, of dilution jets upstream to the turbine entry section. Such characteristics make the aero-thermal field on the combustor/turbine interface very "aggressive", being characterized by temperature non-uniformities, residual swirl and high turbulence intensity.

Given the growing interest in the topic by industry, the present thesis aims to investigate, from a numerical point of view, the aero-thermal aspects that characterize combustor/turbine interaction. Despite a large number of studies has been dedicated in scientific literature in the past, especially concerning hot streaks migration in turbine stages, comprehensive studies of the combustor/turbine interaction are still very limited.

The first part of the work is dedicated to the development and validation of a CFD methodology oriented to the integrated study of combustor and turbine. Such method is also applied to a case of interaction between an annular combustion chamber and a high-pressure vane row.

In the second part of the work, the impact of non-uniformities that characterize combustor exit flow, is investigated on film cooled high-pressure vanes by means of conjugate heat transfer simulations.

Results point out the need of integrated studies for the correct reproduction of the actual working conditions at which components are subjected to, evidencing aspects related to both aerodynamics and heat transfer that are not predictable without considering components interaction.

# Contents

# List of Figures

# List of Tables

# Nomenclature

### Acronyms

| | |
|---|---|
| $ACARE$ | Advisory Council for Aviation Research and Innovation in Europe |
| $BR$ | Blowing Ratio [−] |
| $CFD$ | Computational Fluid Dynamics |
| $CFL$ | Courant-Friedrichs-Lewy number |
| $CHT$ | Conjugate Heat Transfer |
| $DES$ | Detached Eddy Simulation |
| $DR$ | Density Ratio [−] |
| $EOTDF$ | Enhanced Overall Temperature Distortion Factor |
| $FACTOR$ | Full Aerothermal Combustor-Turbine interactiOns Research |
| $FFT$ | Fast Fourier Transform |
| $GCI$ | Grid Convergence Index |
| $GMRES$ | Generalized Minimum RESidual method |
| $HPT$ | High-Pressure Turbine |
| $HTC$ | Heat Transfer Coefficient $[W/(m^2K)]$ |
| $ILPF$ | Isentropic Light Piston Facility |
| $ILU$ | Incomplete LU factorization |
| $LSRR$ | Large Scale Rotating Rig |
| $LE$ | Leading Edge |
| $LES$ | Large Eddy Simulation |
| $MPI$ | Message Passing Interface |
| $MUSCL$ | Monotone Upstream-centered Schemes for Conservative Laws |
| $NGV$ | Nozzle Guide Vane |
| $NRBC$ | Non-Reflecting Boundary Conditions |
| $NSCBC$ | Navier-Stokes Characteristic Boundary Conditions |
| $PS$ | Pressure Side |
| $RANS$ | Reynolds-Averaged Navier-Stokes equations |
| $RQL$ | Rich-Quench-Lean |

| | |
|---|---|
| $RTDF$ | Radial Temperature Distortion Factor |
| $SAS$ | Scale Adaptive Simulation |
| $SILOET$ | Strategic Investment in Low-Carbon Engine Technology |
| $SIMPLE$ | Semi-Implicit Method for Pressure-Linked Equations |
| $SS$ | Suction Side |
| $SST$ | Shear Stress Transport |
| $TATEF$ | Turbine Aero Thermal External Flows |
| $TRF$ | Turbine Research Facility |
| $TTF$ | Turbine Test Facility |
| $URANS$ | Unsteady Reynolds-Averaged Navier-Stokes equations |
| $WCTF$ | Warm Core Turbine Facility |

**Letters**

| | | |
|---|---|---|
| $A$ | Area | $[m^2]$ |
| $a$ | Sound speed | $[m/s]$ |
| $\mathbf{B}$ | Backward set of information | *see text* |
| $C, L$ | Chord | $[m]$ |
| $c$ | Progress variable | $[-]$ |
| $c_p$ | Specific heat at constant pressure | $[J/(kg \cdot K)]$ |
| $d$ | Trailing edge diameter | $[m]$ |
| $D$ | Generic dimension | $[m]$ |
| $Da$ | Damköhler's number | $[-]$ |
| $E$ | Total internal energy | $[J/kg]$ |
| $e$ | Specific internal energy | $[J/kg]$ |
| $e_i$ | i-th component of unit vector | $[-]$ |
| $\mathbf{F}$ | Forward set of information | *see text* |
| $\mathbf{F_{ce}}$ | Centrifugal action | $[N/m^3]$ |
| $\mathbf{F_{co}}$ | Coriolis action | $[N/m^3]$ |
| $\mathbf{f}$ | Convective terms | *see text* |
| $f$ | Mixture fraction | $[-]$ |
| $f'$ | Mixture fraction variance | $[-]$ |
| $G_\theta$ | Axial flux of tangential momentum | $[m^5/s^2]$ |
| $G_x$ | Axial flux of axial momentum | $[m^4/s^2]$ |
| $\mathbf{g}$ | Diffusive terms | *see text* |
| $H$ | Specific total enthalpy | $[J/kg]$ |
| $H$ | Height | $[m]$ |
| $h$ | Specific static enthalpy | $[J/kg]$ |
| $H^*$ | Height of throat section | $[m]$ |
| $K$ | Jacobian matrix | |
| $k$ | Turbulent kinetic energy | $[m^2/s^2]$ |

| | | |
|---|---|---|
| $M$ | Blowing ratio | $[-]$ |
| $M$ | Mach number | $[-]$ |
| $M$ | Ratio between modeled and total $k$ | $[-]$ |
| $\dot{m}$ | Mass flow rate | $[kg/s]$ |
| $p, P$ | Pressure | $[Pa]$ |
| $Pr$ | Prandtl number | $[-]$ |
| $\mathbf{Q}$ | Vector of conservative variables | *see text* |
| $Q$ | Thermal power | $[W]$ |
| $\dot{q}$ | Thermal flux | $[W/m^2]$ |
| $\mathbf{R}$ | Residuals vector | *see text* |
| $R$ | Specific gas constant | $[J/(kg \cdot K)]$ |
| $R$ | Radius | $[m]$ |
| $r$ | Radial coordinate | $[m]$ |
| $Re$ | Reynolds number | $[m]$ |
| $\mathbf{S}$ | Vector of source terms | *see text* |
| $S$ | Magnitude of the strain rate tensor | $[s^{-1}]$ |
| $Sc$ | Schmidt number | $[-]$ |
| $S_N$ | Swirl number | $[-]$ |
| $s$ | curvilinear coordinate | $[m]$ |
| $T$ | Temperature | $[K]$ |
| $t$ | Time | $[s]$ |
| $Tu$ | Turbulence level | $[\%]$ |
| $u, v, w, V, U$ | Flow velocity | $[m/s]$ |
| $U_t$ | Turbulent flame speed | $[m/s]$ |
| $V$ | Cell volume | $[m^3]$ |
| $x_i, x, y, z$ | Spatial coordinates | $[m]$ |
| $Y$ | Mass fraction | $[-]$ |
| $y^+$ | Non-dimensional wall distance | $[-]$ |

**Greek Letters**

| | | |
|---|---|---|
| $\gamma$ | specific heat ratio | $[-]$ |
| $\delta_{ik}$ | Kronecker's delta | $[-]$ |
| $\epsilon$ | Turbulence dissipation rate | $[m^2/s^3]$ |
| $\eta$ | Film cooling effectiveness | $[-]$ |
| $\theta$ | Non-dimensional temperature | $[-]$ |
| $\lambda$ | turbulent length scale | $[m]$ |
| $\mu$ | Dynamic viscosity | $[kg/(m \cdot s)]$ |
| $\nu$ | Cinematic viscosity | $[m^2/s]$ |
| $\xi$ | Loss coefficient | $[-]$ |
| $\rho$ | Density | $[kg/m^3]$ |

| | | |
|---|---|---|
| $\tau_{ik}$ | $i$,$k$ element of the viscous stress tensor | $[Pa]$ |
| $\Phi$ | Equivalence ratio | $[-]$ |
| $\vec{\omega}$ | Vorticity vector | $[s^{-1}]$ |
| $\omega$ | Specific turbulence dissipation rate | $[s^{-1}]$ |

**Subscripts**

| | |
|---|---|
| 0 | stagnation quantity |
| 1 | referred to inlet section |
| 2 | referred to outlet section |
| $aw$ | adiabatic wall |
| $air$ | referred to air |
| $ax$ | in axial direction |
| $b$ | bulk |
| $BP$ | referred to bypass transition |
| $burnt$ | referred to combustion products |
| $cc$ | referred to combustion chamber |
| $crit$ | critical |
| $des$ | in design conditions |
| $eff$ | effective |
| $fuel$ | referred to fuel |
| $in$ | inlet |
| $is$ | isentropic |
| $L$ | referred to laminar quantity |
| $m, main$ | referred to main flow |
| $max$ | maximum |
| $min$ | minimum |
| $mod$ | modeled |
| $mwa$ | mass-weighted average |
| $NAT$ | referred to natural transition |
| $n.d.$ | non-dimensional |
| $ox$ | referred to oxidizer |
| $rec$ | recovery |
| $red$ | reduced |
| $ref$ | reference quantity |
| $res$ | resolved |
| $rms$ | root-mean-square |
| $s.a.$ | spanwise averaged |
| $sw$ | referred to swirler |
| $T, t$ | referred to turbulent quantity |

| | |
|---|---|
| $t.a.$ | tangentially averaged |
| $tot$ | total |
| $unburnt, u$ | referred to unburned mixture |
| $w, wall$ | referred to the wall |
| $x$ | in x direction |

**Superscripts**

| | |
|---|---|
| $L$ | left state |
| $R$ | right state |
| $T$ | transposed |

**Symbols**

| | |
|---|---|
| $\overline{[\,]}$ | Average |
| $\tilde{[\,]}$ | Tensor |

# Introduction and motivations of the work

The development of gas turbines has been driven in the last years by the need of increased performance and efficiency, but also by emissions regulations. In particular, these latter are become more and more restrictive, imposing the introduction of new technologies. Combustors have been object of research, especially with the aim of reducing $NO_x$ emissions, in the fields of heavy-duty gas turbines and aero engines. Lean-burn combustion technology has been identified to be the key methodology for combustion systems to achieve legislative requirements for $NO_x$ emissions. It is by now a mature technology for gas turbines dedicated to power generation but is still on development for aero engines. In this latter context, significant emissions reductions have been requested by the ACARE (Advisory Council for Aviation Research and Innovation in Europe), that imposed in 2002 a reduction of the $NO_x$ emissions of $-80\%$ by 2020 compared to 2000 [1]. This objective has been recently further reduced to $-90\%$ by 2050 [2]. Such very demanding objectives enforced the study of lean-burn combustion systems also in aero engines.

Lean combustion technology operates with an excess of air in order to significantly reduce flame temperature with respect to traditional Rich-Quench-Lean (RQL) systems, reducing the $NO_x$ production due to the thermal mechanism (named also Zeldovich mechanism). Up to 70% of the total air flow has to be premixed with fuel before entering the reaction zone within the combustion chamber. Therefore, cooling flow must be

reduced accordingly to provide sufficient air for mixing. Such air splitting leads to a different combustor layout with respect to RQL combustors, leading to more compact volumes with high swirl numbers in order to guarantee an adequate flame stabilization. No use is made of dilution jets, or however they are very limited. In this way the strong swirl imposed by the burners persists up to the first turbine stage. All these characteristics make the aero-thermal field on the interface between combustion chamber and high-pressure turbine very aggressive. In order to fill the lack of knowledge of the actual working conditions at which components are subjected to, it is necessary to introduce integrated analysis of combustor and high-pressure turbine.

In this context, Computational Fluid Dynamics (CFD) represents a powerful instrument that supports researchers and designers in understanding aerodynamic and thermal issues, reducing the need of expensive experimental activities, at least in the early parts of the design process.

Motivated by the aforementioned necessity, this thesis presents numerical investigations of the aero-thermal aspects that characterize the interaction between combustion chamber and first stage of high-pressure turbine. The activity has been divided into two parts. The first one is dedicated to the development, validation and application of a methodology for the integrated CFD simulation of combustor and turbine. The second part is aimed to study the effects of combustor non-uniformities on cooled high-pressure vanes by means of conjugate heat transfer simulations that allow the prediction of local temperature of metal components. Before the two aforementioned parts, a literature review is proposed in the first Chapter of the thesis. It is aimed to characterize the interface between combustor and turbine from an aero-thermal point of view and to provide an overview of the physical phenomena involved.

# Chapter 1

# Literature review

## Contents



In this first chapter, an overview of the aero-thermal aspects that characterize the interaction between combustion chamber and high-pressure turbine is proposed. The final part of the chapter is dedicated to a review of the current numerical methodologies used for the integrated study of combustion chamber and high-pressure turbine.

Before to treat the various aspects in detail, it is appropriate to give a first, rough, characterization of the flow field at the exit of a modern gas turbine combustion chamber. It is, in general, characterized by:

- total temperature non-uniformities
- residual swirl
- high turbulence level
- total pressure non-uniformities

All these aspects will be treated in this chapter of the thesis, trying to give qualitative and quantitative characterizations. The information collected from the scientific literature will be useful for the studies proposed in this work in order to give a characterization of the aero-thermal field of the combustor/turbine interface.

Combustor/turbine interaction is a relatively new topic in turbomachinery research and covers many aspects of the physics of gas turbine operation. Some of these aspects, like temperature non-uniformities, were studied singularly in a considerable number of papers published in the past twenty five years. Nevertheless, only in the last few years researchers started to analyze the problem in its entirety, approaching the comprehension of the actual physical phenomena which result from the simultaneous presence of all the aspects listed above. Following this "fragmentation" of the scientific literature, the results of the published research are analyzed in the following sections.

## 1.1 Characterization of the aero-thermal field on the combustor/turbine interface

### 1.1.1 Combustor exit temperature non-uniformities and hot streak transport in turbine stages

One of the aspects that makes combustor/turbine interaction a challenging topic in gas turbine research is the difficulty in dealing with an experimental campaign under actual working conditions. Experimental tests aimed to determining the temperature field at the combustor exit section on full-scale geometries, at the machine design point, are extremely difficult and expensive. For these reasons, scientific papers that

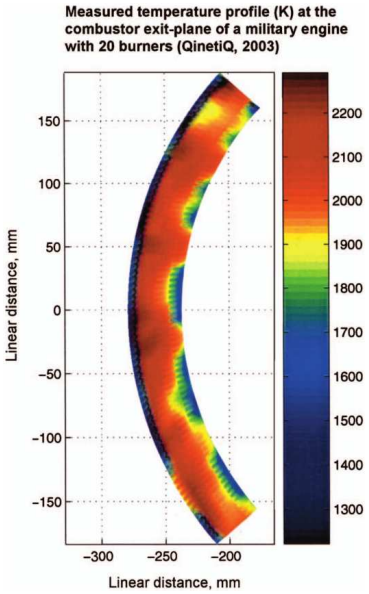


Figure 1.1: Combustor exit temperature field of a military engine, from Povey et al. [3].

shown temperature profiles at the inlet of the high-pressure turbine are a very limited number. An overview of the characteristics of a temperature field established downstream of gas turbine combustors is given in the follow.

Figure 1.1 shows the time average temperature field measured at the exit section of a typical modern military engine, equipped with 20 burners [3]. Thermal field is characterized by maximum temperature peaks over 2200 $K$, while the coldest regions, located near hub and casing, are even below 1500 $K$. Hot spots are present due to the tangential temperature gradients generated by the discrete number of fuel injection points and to the presence of dilution jets [3] (no other information is provided by the authors about the type of combustion system). Strong radial gradients are caused by the liner cooling, even if the coverage provided by the

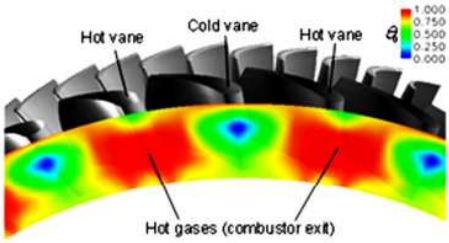


Figure 1.2: Non-dimensional temperature distribution at the inlet of the high-pressure turbine experimentally measured by Mitsubishi Heavy Industries (Ong and Miller [4]).

coolant seems to be not sufficient to avoid hight temperature zones near the endwalls. Figure 1.1 allows also to note that, for this particular case, the strongest tangential temperature gradients are located near hub.

Figure 1.2 shows an example of non-dimensional total temperature profile, which definition is given in equation 1.1.

$$\theta_0 = \frac{T_0 - T_{0,min}}{T_{0,max} - T_{0,min}} \tag{1.1}$$

It has been obtained from experimental measurements on a heavy-duty Mitsubishi gas turbine; the image is taken from the work by Ong and Miller [4]. In this case, the machine layout strongly influences the temperature map. The machine is equipped with a can-annular combustor, where multiple flame tubes are positioned circumferentially within an annular casing and are connected with the turbine inlet section through transition pieces. The well defined hot spots are clearly visible from Figure 1.2, where the cold spots are also observable. As stated by Ong and Miller [4], such cold spots are generated by leakage of compressor exit flow close to the flanges of the transition pieces. The can-annular combustor arrangement, therefore, leads to have alternate “hot” and “cold” vanes.

Another representative total temperature distribution downstream of a new generation lean-burn combustor for aero engines, presented by

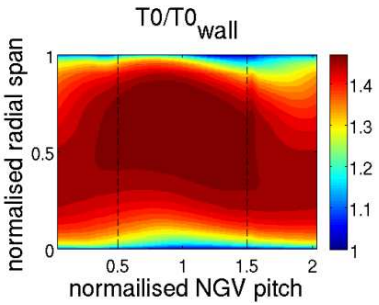


Figure 1.3: Turbine total temperature inlet profile used by Shahpar and Caloni [5] on the SILOET test case.

Shahpar and Caloni [5], is reported in Figure 1.3. Such temperature profile has been used within the SILOET (Strategic Investment in Low-carbon Engine Technology) programme by Rolls-Royce. The stagnation temperature, obtained from a numerical simulation, is normalized with respect to a reference wall temperature. Distribution of hot and cold zones is similar, for certain aspects, to the one reported in Figure 1.1. In this case, temperature gradients are mainly in radial direction, due to the combustor liner cooling, but a marked hot spot is observable in the region at normalized pitchwise coordinate between 0.5 and 1.5.

Due to the difficulty of experimental testing in actual engine conditions, some research groups approach the problem of characterizing the turbine inlet temperature profile by means of tests under similitude conditions or through the development of "combustor simulators". For both these approaches, the flow is non-reactive and the exit temperature non-uniformity is studied by reproducing a hot spot through electric heaters or by means of the use of non-reacting tracers. For this latter approach, the mass transfer analogy is used to derive a non-dimensional temperature distribution.

Cha et al. [6] present the experimental study of a RQL aero engine combustion chamber, tested in similitude conditions, without fuel injection. The test rig includes the full annular liner with burners and injec-

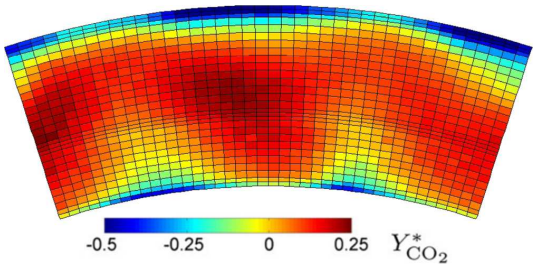


Figure 1.4: Distribution of a non-reacting tracer measured experimentally by Cha et al. [6] at the exit secion of an aeronautical combustor in similitude conditions.

tion systems. Since a cold flow test is considered, $CO_2$ is used as non-reactive tracer in order to reproduce the hot fluid distribution within the combustion chamber. Figure 1.4 reports the corrected $CO_2$ concentration, obtained on a section positioned on the combustor-turbine interface plane, at which the boundary conditions are normally specified during the numerical simulation of the high-pressure turbine. A wavy-shaped hot streak is present on the investigated plane, with the maximum peaks located about at the mean radius of the channel. The cold zones are positioned along the endwalls and are more extended near casing. Figure 1.5

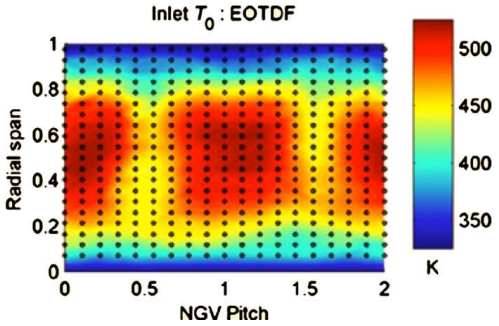


Figure 1.5: Non-dimensional temperature distribution measured downstream of the hot streak generator proposed by Qureshi et al. [7].

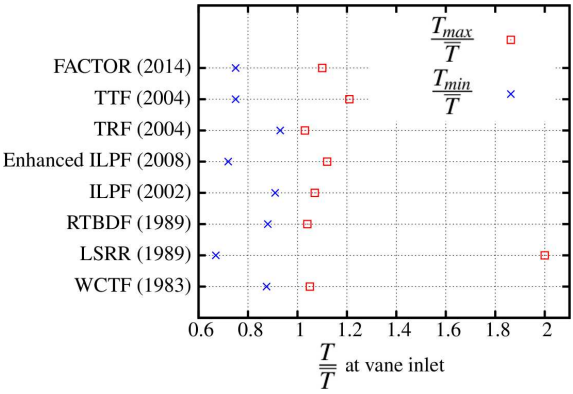


Figure 1.6: Overview of the maximum and minimum non-dimensional temperature peaks in different hot streaks generators; adapted from Koupper et al. [8].

reports the total temperature distribution obtained by Qureshi et al. [7] downstream of a hot streak generator. The map covers two NGV pitches and shows clearly the presence of well defined hot spots, positioned centrally in radial direction. In this case, the cold fluid covers very well the endwalls without presenting the tangential gradients evidenced in Figures 1.1, 1.3 and 1.4.

An interesting summary of the most important facilities equipped with hot streaks generators, installed in various laboratories, is given by Koupper et al. [8]. Figure 1.6 reports maximum and minimum non-dimensional temperature peaks reached in each hot streak generator; temperature is non-dimensionalized using its average value. The facilities considered are the following:

- FACTOR (Full Aerothermal Combustor-Turbine interactiOns Research) test rig; Koupper et al. [8]
- TTF (Turbine Test Facility); Mathison et al. [9] and Dunn and Mathison [10]
- TRF (Turbine Research Facility); Barringer et al. [11]

- ILPF (Isentropic Light Piston Facility) with enhanced Overall Temperature Distortion Factor described by Povey and Qureshi [12], which temperature profile is the same reported in Figure 1.5
- ILPF (Isentropic Light Piston Facility); Hilditch et al. [13]
- RTBDF; Shang et al. [14]
- LSRR (Large Scale Rotating Rig); Joslyn and Dring [15]
- WCTF (Warm Core Turbine Facility); Stabe et al. [16]

All the temperature distortions are in the range $0.73 < T/\overline{T} < 1.21$ except the LSRR case, that is characterized by a wider temperature interval $0.68 < T/\overline{T} < 2.0$. Amongst the listed ones, the three most recent facilities are also the more representative of modern aero engines. In particular, the test rig of the FACTOR European project, currently under investigation, is aimed to simulate the flow exiting from a new generation lean-burn, effusion-cooled, aero engine annular combustion chamber.

In order to summarize the qualitative and quantitative aspects emerged from the analysis of the temperature field treated above, it is worth to remark some aspects:

- The most intense temperature gradients are mainly directed radially.
- Actual combustor geometries leads to have remarkable tangential non-uniformities near the endwalls. The presence of tangential gradients in the center of the height of the channel is strongly dependent from the combustor architecture.
- Hot streaks coming from actual geometries tend to be pretty distorted. The same is not true for the profile shown in Figure 1.5, coming from the hot streaks generator presented in the work by Povey and Qureshi [12], where well defined hot spots are present. Nevertheless, this consideration can not be generalized to all the hot streaks generators.

- In quantitative terms, the most representative hot streaks generators aimed to reproduce aero engines combustors, are characterized by $0.73 < T/\overline{T} < 1.21$.

After discussing the characteristics of temperature profiles at the inlet of the high-pressure turbine, it is appropriate to treat what are the effects of the distorted thermal filed on turbine operation. The topic of the effects of temperature non-uniformities coming from the combustor and their migration in HPT has been largely treated in literature since 1989, when two studies by Butler et al. [17] and Rai and Dring [18] investigated experimentally and numerically the argument. Their study were conducted on a single-stage axial turbine working with air, where the inlet hot spots was reproduced by means of circular spots of heated air seeded with $CO_2$. The main findings can be summarized as follow. The stator flow filed is not affected by the presence of a total temperature distortion without total pressure non-uniformities, in agreement with the so-called *substituion principle* proposed by Munk and Prim [19]. It has been formulated for a steady isentropic flow in absence of volume forces but can be extended, as a first approximation, for the analysis of the flow outside of the boundary layer in stator rows. For a given geometry and a defined inlet total pressure field, streamlines, Mach number and static pressure field are not influenced by the inlet total temperature field. On the contrary, the rotor flow field is strongly affected by the hot streak and a *segregation effect* is created. The hot fluid migrates through the pressure side of the blades, as shown in Figure 1.7, while the cold fluid along the suction side. These preferential migrations of hot and cold fluid, further confirmed by Dorney et al. [20], are caused by the difference of velocity angles in the relative frame. The segregation effect is explained schematically in Figure 1.8. This mechanism has been evidenced for the first time by Kerrebrock and Mikolajczack [22] treating the wake transport inside compressors but can be used to explain the preferential migration of hot fluid through the pressure side of the rotor blades. Looking at Figure 1.8, taken from the work by Martelli et al. [21], the "design" velocity triangle at the rotor inlet section is char-

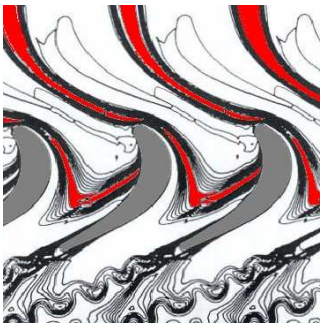

Figure 1.7: Preferential migration of hot fluid through the pressure side of the blades, from Rai and Dring [18].

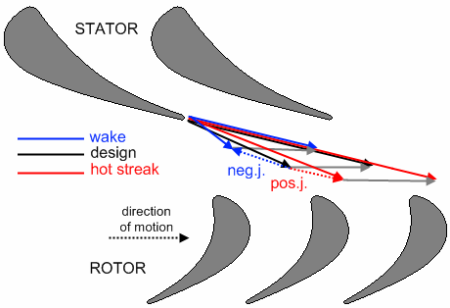


Figure 1.8: Schematic of the segregation effect, from Martelli et al. [21].

acterized by a certain relative inflow angle that guarantees the optimal incidence on the blades. The wake flow has obviously a reduced velocity and the relative velocity vector is directed more axially. The contrary happens for the hot fluid. Recalling the substitution principle, the hot streak having the same absolute total pressure of the surrounding fluid, but reduced density, has an higher absolute velocity and a higher relative tangential component. The opposite happens for the hot fluid, similarly to the wake flow. Once made these consideration, it is evident that the hot fluid impacts on the blades with positive incidence and vice versa for the cold fluid. Comparing the velocity triangles of the hot and cold

fluid with the design one, it is possible to identify two "sleep velocity", called respectively "positive jet" and "negative jet" in Figure 1.8. Such sleep velocity are the aerodynamic effects to which the rotor blades are subjected to in the relative frame.

From a thermal point of view, the preferential migration of the hot fluid through the pressure side leads to the formation of a hot spot on this latter that can not be predicted considering uniform inlet flow conditions. For this reason, the migration of the hot spot originated from the combustion chamber needs to be taken into account during the thermal design process, in order to guarantee appropriate safety margins.

Two important aspects of a gas turbine layout are the ratio between number of burners and high-pressure vanes and the relative circumferential positioning between burners and vane passages. These parameters, that are selected by designers during the early parts of the machine design, have been the subject of the study performed by He et al. [23]. The study has been conducted, by means of numerical simulations, on the research high-pressure turbine stage MT1, designed by Rolls-Royce. The stage is composed by 32 vanes and 60 rotor blades. The authors tested two different relative alignments between vanes and hot spots with two different numbers of these latter. Figures 1.9(a) and 1.9(b) show respectively the hot spot alignment with leading edge and vane passage. Figure 1.10 reports the two different hot spots counts used, with hot spot-to-vane ratios of $1:4$ and $1:1$. The shape of the inlet total temperature distortions is sinusoidal in both radial and tangential directions and is characterized by the ratio $T_{0,max}/T_{0,min} = 1.5$. Results have shown that, for the $1:1$ case, the rotor blade thermal load is strongly dependent from the hot streak/NGV clocking, while the aerodynamic forcing is almost independent from it. On the contrary, for the $1:4$ case, clocking has a very little effect in determining the adiabatic blade temperature while the unsteady forcing on the rotor blades is at least five times higher than for the $1:1$ case. Although such results have been obtained with theoretical total temperature inlet distributions, without considering any other type of flow distortion coming from the combustor, they give very important

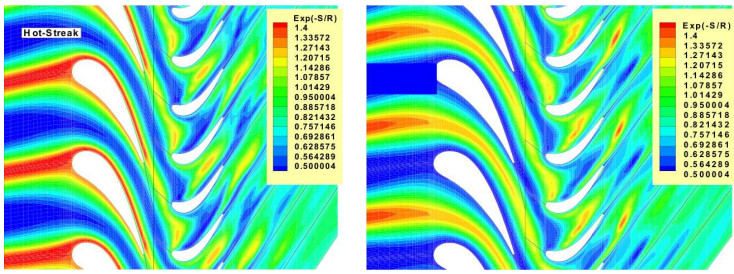


**(a)** hot streaks aligned to the leading edges **(b)** hot streaks aligned to the passages

Figure 1.9: Relative alignment between hot streaks and vanes [23]; entropy contours are shown.

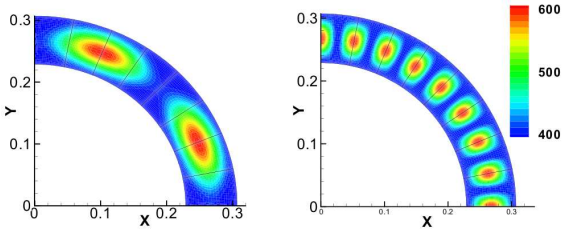


Figure 1.10: Temperature contours that shows hot spots with two different circumferential length scales [23].

information concerning the necessity of considering combustor/turbine interaction during aero-thermal design of the machine.

### 1.1.2 Residual swirl on the turbine inlet section

Modern low emission combustion chambers make use of strong swirl flows in order to provide an adequate flame stabilization. A high swirl number is imposed to the flow by means of appropriate systems located in the burners. The definition of swirl number $S_N$, typically used to

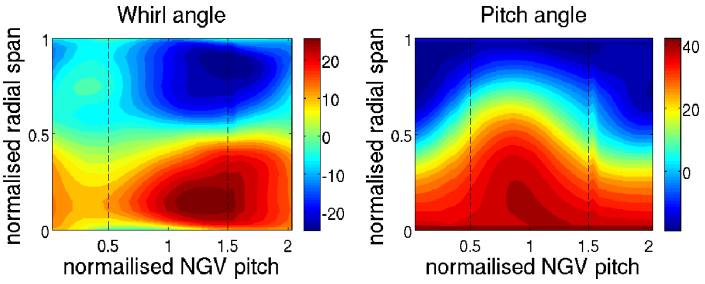


**(a)** whirl angle (°) **(b)** pitch angle (°)

Figure 1.11: Whirl and pitch angle distributions downstream of a lean-burn combustor reported by Shahpar and Caloni [5].

characterize swirling flows, is given in equation 1.2

$$S_N = \frac{G_\theta}{R_{sw} G_x} \tag{1.2}$$

where $G_\theta$ is the axial flux of tangential momentum, $R_{sw}$ is the outer radius of the duct from which swirl is originated and $G_x$ is the axial flux of the axial momentum. Swirl numbers higher than 0.6 are often adopted in modern combustors. The intensity of the tangential velocity component makes swirl persist downstream, up to the nozzle guide vanes of the high-pressure turbine. This is particularly significant for lean-burn combustors, where two aspects contribute to maintain swirl up to the combustor exit section. The first aspect is certainly the fact of using very high swirl numbers and the other is connected to the absence, or more in general, to the reduction of dilution jets, that would contribute to dissipate swirl.

Figure 1.11, taken from the work by Shahpar and Caloni [5], reports the whirl and pitch angles distributions, obtained numerically on the outlet section of a new generation lean-burn aero engine combustor. As it is possible to observe, in support to what stated above, an organized flow distortion is present, indicating that combustor swirl is conserved up to the exit. For this particular case the maximum and minimum whirl

Figure 1.12: Swirl generator used in the work by Qureshi et al. [24].

angles are respectively $+25°$ near hub and $-25°$ near casing, while the pitch angle ranges from $0°$ near casing to $40°$ near hub.

Against this background, some works in the scientific literature have investigated the effects of swirl on the aero-thermal behaviour of the high pressure turbine. In the follow, some of the results are reported and discussed.

Qureshi et al. [24], in the Oxford Turbine Research Facility, used the annular device reported in Figure 1.12, constituted by 16 swirl generator. Each of them is composed by 6 stationary flat-plate vanes inclined by an angle of $40°$ with respect to the axial direction. The generated swirl have been experimentally measured and is reported in Figure 1.13 in the form of vector plot and yaw angle distributions at 20% and 80% of the radial position. Figure 1.13(b) quantifies the swirl intensity in proximity of the endwalls, which is characterized by maximum and minimum peaks of yaw angle respectively equal to about $50°$ and $-50°$. Qureshi et al. [24] applied such swirl profile to the inlet section of the MT1 high-pressure turbine stage, investigating experimentally and numerically what are its effects. The ratio between vanes and swirlers is $1 : 2$ (16 swirlers and 32 vanes), while the rotor counts 60 blades. Results have shown that the vane aerodynamics is considerably altered by swirl, resulting in relevant changes in the rotor incidence, up to $+4°$ from midspan to tip and $-6°$ near hub with respect to the uniform inlet case. Such incidence changes

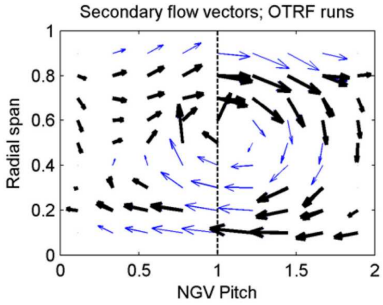


**(a)** swirl vectors

**(b)** yaw angle at 20% and 80% of the span

Figure 1.13: Swirl profile obtained by Qureshi et al. [24] through the swirl generator of Figure 1.12.

modify the structure of the flow pattern within the rotor itself, impacting also on heat transfer along the casing, where experiments with inlet swirl have shown an increment of 20% of the Nusselt number with respect to the uniform case. In terms of Nusselt number along the rotor surface, an increase between 7% and 13% have been observed on the suction side. It is attributed by the authors to the enhanced turbulence intensity with inlet swirl. Along the pressure side, an increment of the Nusselt number of about 8% near hub and up to 40% near tip have been observed. Such significant increase in the upper part of the blade is mainly due to increased secondary flows due to swirl, that enhance tip leakage flow.

Schmid and Schiffer [25] studied a linear cascade of nozzle guide vanes by means of numerical simulations, including inlet swirl vortices in a $1:1$ ratio with respect to the vane counts. They considered three different swirl numbers, equal to 0.6, 0.8 and 1, as well as three different swirl orientations (clockwise, counter clockwise and counter rotating). Results have shown that an increase of the swirl intensity is accompanied by a strong increase of the total pressure loss coefficient, that ranges from $+25\%$ of the value obtained with axial flow for $S_N = 0.6$, up to $+35\%$ for $S_N = 1$. Moreover, remarkable effects of the swirl orientation have

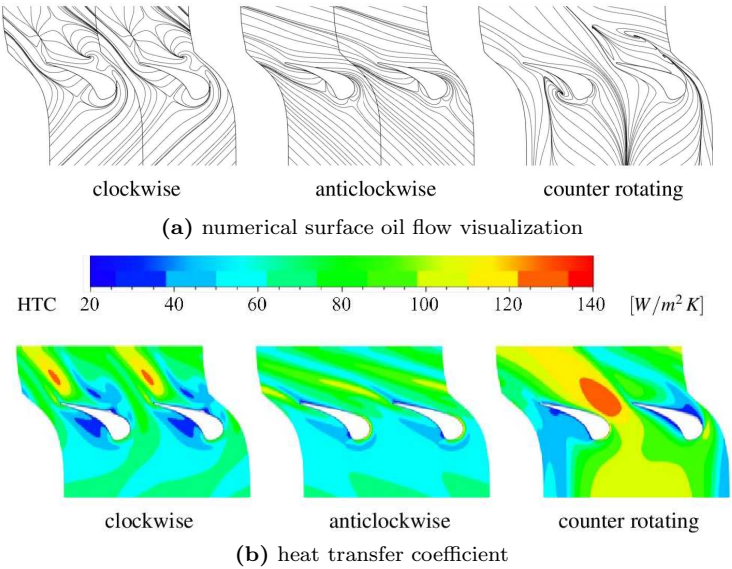


**(a)** numerical surface oil flow visualization

**(b)** heat transfer coefficient

Figure 1.14: Effects of swirl orientation on the hub of a nozzle guide vane; adapted from the work by Schmid and Schiffer [25].

also been observed. Figure 1.14 reports a "numerical surface oil flow visualization" along the hub of the cascade, allowing to observe very different flow features for the three reported cases. When the swirling flow near hub is almost orthogonal to the vane orientation (clockwise case), the saddle point of the streamlines impacting on the vane surface is moved through the pressure side. The opposite happens for the counter clockwise case, for which the saddle point is moved along the suction side. A different situation occurs when alternate swirl directions are used for the adjacent vanes (counter rotating case). In this case, the flow features are very different from the two aforementioned cases and the two vanes works very differently one from the other. Figure 1.14(b) shows how the complex flow feature created, especially in the clockwise and the counter rotating cases, generates local increases of the heat transfer coefficient that could be potentially deleterious for the metal component from the

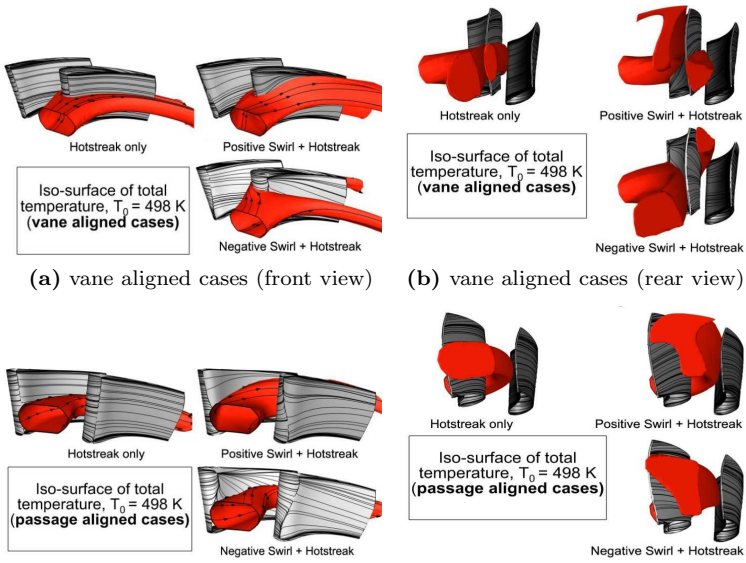


**(a)** vane aligned cases (front view) **(b)** vane aligned cases (rear view)

**(c)** passage aligned cases (front view) **(d)** passage aligned cases (rear view)

Figure 1.15: Effects of swirl orientation and alignment in determining hot spot migration from the work by Khanal et al. [26].

thermal point of view.

Khanal et al. [26] investigated numerically the hot streak transport in the MT1 high-pressure turbine stage with the contemporaneous presence of an inlet swirl and a hot spot centered on the swirl core. They considered two different relative alignments between swirl and vanes: swirl aligned to the vane leading edge and aligned with the passage. Moreover, for each of these cases they considered also positive and negative swirl directions. A case with the hot spot only, without swirl, is also taken into account for each of the alignments. The behaviours of the hot streak transport are reported in Figure 1.15. Swirl is responsible for determining the radial migration of the hot streak inside the vane passages, going to affect the temperature distortion on the inlet section

of the downstream rotor. In fact, for all the cases shown in Figure 1.15, the shape of the hot streak is very different from the case without swirl. In particular, considering the vane aligned cases, when a positive swirl is used, highest temperatures are found near casing on the pressure side and near hub on the suction side. The opposite happens for negative swirl. When the passage aligned cases are considered, the positive swirl tends to redistribute the hot streak in pitchwise direction inside the passage in the medium/high part of the span, while the hot fluid is confined in the center of the passage in the lower part of the channel. A similar behaviour is found for the negative swirl case, even if the region near casing results less thermally loaded and the hot streak less extended in pitchwise direction with respect to the positive swirl case. Khanal et al. [26] individuated the passage aligned case with negative swirl as the less impacting from the aero-thermal point of view, offering the lower heating of the rotor tip and the lower loss coefficient of the nozzle guide vane.

Until now there has been talk about uncooled components of the turbine but it is worth to consider swirl effects on cooling systems. Scientific literature is very limited in this field. Two interesting works have been presented by Giller and Schiffer [27] and Hong et al. [28]. They studied the effects of swirl in determining the performance of a leading edge cooling system.

Giller and Schiffer [27] considered a linear cascade of high-pressure vanes with two rows of cooling holes positioned along the leading edge. They investigated two different configurations, considering holes with and without upward inclination. One of the most relevant aspects observed is that, with swirl, the shape of the stagnation line does no longer follow the leading edge line but is twisted. This behaviour is visible also in Figure 1.15. The twisting of the stagnation line means that the locus of points with high pressure is moved along pressure and suction side, depending on the spanwise position and on the direction of rotation of the swirl. Consequently, since the coolant stagnation pressure is approximately the same for all the channels fed by the same plenum, at all the spanwise positions, the pressure ratio across each channel is modified. In this way

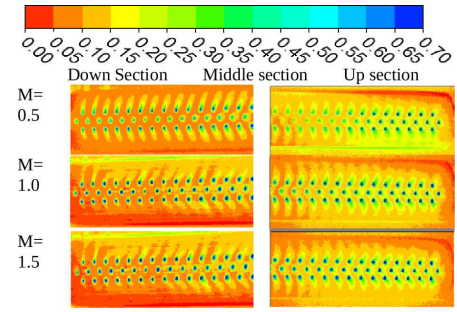


**(a)** axial inlet flow

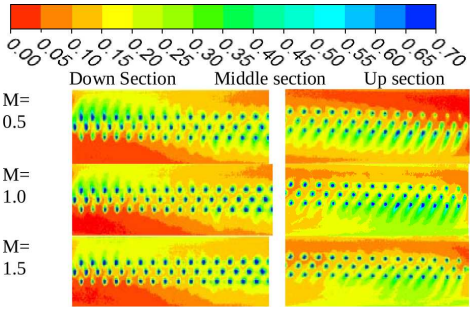


**(b)** swirled inlet flow

Figure 1.16: Effect of swirl in determining the adiabatic effectiveness on a cooled leading edge model by Hong et al. [28].

all the cooling system parameters are changed with respect to the case with axial flow, leading to altered mass flow repartition, different blowing ratio and, consequently, different cooling effectiveness.

Similar conclusions are drawn in the work by Hong et al. [28], where a cooled leading edge model is investigated. According to what observed by Giller and Schiffer [27], the adiabatic effectiveness is strongly influenced by swirl. This is observable in Figures 1.16(a) and 1.16(b), where the adiabatic film cooling effectiveness for axial inlet flow is compared with the one obtained with inlet swirl. The distorted behaviour clearly appears from Figure 1.16(b), evidencing scarcely covered zones, especially near

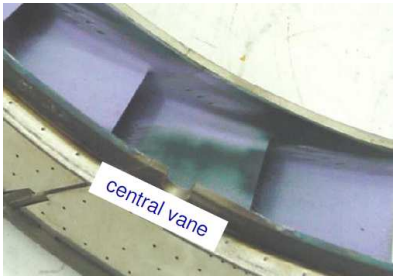


**(a)** sector

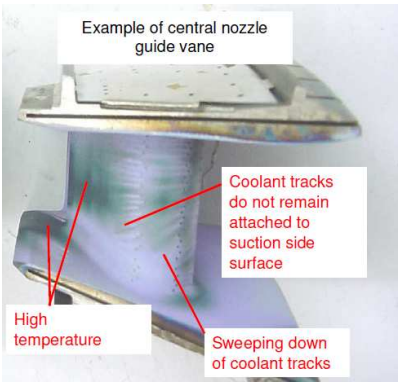


**(b)** central vane


**(c)** non-central vane

Figure 1.17: Images taken from the work by Turrel et al. [29], showing high temperature zones on a sector of nozzle guide vanes.

the endwalls.

Figure 1.17, taken from the work by Turrel et al. [29], shows the vanes located downstream of a low emission can combustor. Images, obtained experimentally by means of temperature-sensitive paint, allow to visualize the high temperature zones on the metal components. Figure 1.17(a) shows how the suction side of the vane located centrally, and aligned with the combustor burner, is subjected to a higher thermal load with respect to the adjacent part. A detail of the coolant tracks on the central vane is reported in Figure 1.17(b). As indicated in the image,

coolant is deflected downward in the lower part of the vane, while in the central part of the span, coolant does not reach to remain attached to the surface, leaving uncovered zones. A very different behavior is shown in Figure 1.17(c) for a non-central vane, on which coolant seems to remain attached, without leaving significant unprotected zones. Turrel et al. [29] attribute a similar behavior to the effect of swirl. The core of the residual swirl is, in fact, aligned with the central vane, causing the significant "off-design" behavior of the cooling system.

### 1.1.3 Turbulence intensity and length scale on the turbine inlet section

The topic of turbulence on the inlet section of the high pressure turbine has been subject of discussion in the years. Researchers agreed to say that a "high" turbulence intensity is present downstream of the combustion chamber even if the actual value of the turbulence fluctuations and their length scale are emerging only from recent studies, thanks to the increased attention on the topic of combustor/turbine interaction.

In 1999, Radomsky and Thole [30] provided a review of the existing literature, individuating the turbulence level downstream of various types of combustion chambers between 9% and 30%. Moreover, nevertheless only a few information are present concerning the turbulence length scale, Radomsky and Thole [30] indicated an interval between 0.1 and 0.14 times the vane pitch.

A significant recent contribution in understanding the characteristics of turbulence on the interface between combustor and turbine has been given by Cha et al. [31]. They studied experimentally a test rig including actual engine hardware, composed by an RQL annular combustion chamber with a downstream row of nozzle guide vanes. Figure 1.18(a) reports the turbulence intensity measured on the combustor/turbine interface plane. Extended zones with high turbulence intensity, up to 35%, are present in the central part of the channel height. Figure 1.18(b) reports the distribution of turbulence length scale, normalized with the vane chord, on the same measurement plane. Peaks of non-dimensional

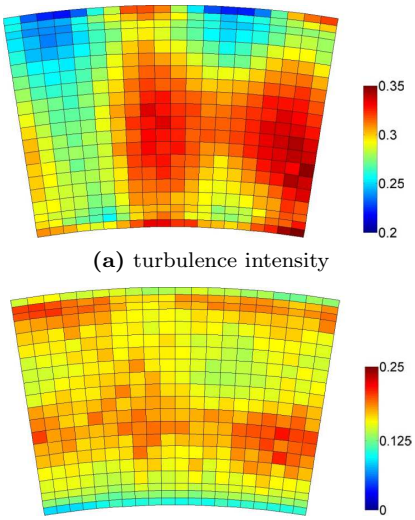


**(a)** turbulence intensity

**(b)** turbulence length scale normalized with respect to the vane chord

Figure 1.18: Turbulence characteristics obtained by Cha et al. [31] downstream of an actual RQL combustor during a cold flow test.

length scale up to 0.25 are present, while extended zones at about 0.17 are observable.

In terms of turbulence level, similar results to the ones found by Cha et al. [31], have been obtained by Koupper et al. [8] with LES simulations of a hot streak generator representative of a lean burn effusion cooled combustor for aero engines. Turbulence level peaks observed are between 35% and 40% and are located in the central parts of the height of the channel.

Radomsky and Thole [30] demonstrated experimentally that the turbulence level of the flow at the turbine entrance does not decay significantly through the nozzle guide vanes but rather remains quite high. Local increases of the turbulent kinetic energy have been observed in the regions characterized by strong curvature of the streamlines, like outside

the boundary layer along the most convex region the suction side and near the stagnation points. High turbulence intensity of the flow within the vane passages leads, in addition to anticipate transition of the boundary layer, also to enhance significantly the heat transfer coefficient, as shown by Radomsky and Thole [30].

### 1.1.4 Total pressure non-uniformities at the combustor exit

Due to the complexity of the flow field inside a combustion chamber, it might seem reasonable to suppose the presence of total pressure non-uniformities on its exit section. Some works report a map of stagnation pressure downstream combustion chambers or hot streak generators. Two examples are shown in Figure 1.19. Figure 1.19(a) shows the experimentally measured total pressure downstream of the hot streak generator whose temperature distortion has been reported in Figure 1.5. Figure 1.19(b) instead shows the stagnation pressure obtained numerically downstream of the lean burn combustor whose temperature distortion has been shown in Figure 1.3. despite a qualitative difference of the maps, both the distributions are characterized by a very narrow range of variation, with the maximum non-uniformity lower than 1.4%. In the case of Figure 1.19(a) it is not possible to observe organized structures due to the low resolution of the experiments. On the contrary, the case in Figure 1.19(b) allows to distinguish some aspects. The zone with the lower total pressure is located in the central part of the channel height and is coincident with the swirl core (see Figure 1.11(a)). Moreover, it is possible to hypothesize that the high total pressure bands positioned near the endwalls are due to the coolant flow injected upstream to protect the liner walls. A behavior quite similar to the one shown in Figure 1.19(b) has been observed also by Hall et al. [32] on a hot streak generator, both in qualitative and quantitative terms.

After this analysis it is possible to conclude that stagnation pressure non-uniformity, on the combustor/turbine interface, are much less important than the temperature distortions and, as a first approximation, it

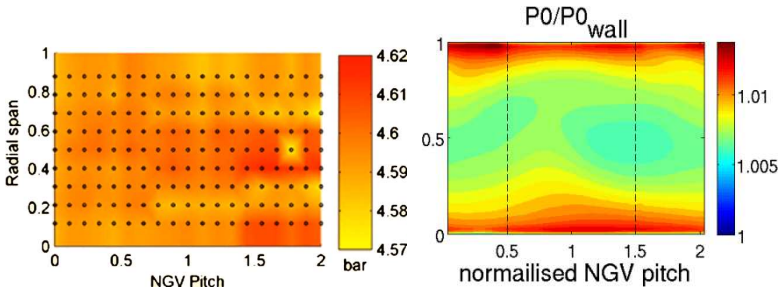


**(a)** from Qureshi et al. [7] **(b)** from Shahpar and Caloni [5]

Figure 1.19: Typical total pressure non-uniformities.

does not constitute a primary aspect of the interaction between combustor and high-pressure turbine.

## 1.2 Numerical approaches for the study of combustor/turbine interaction

As previously stated, experimental investigation of combustor/turbine interaction is very complex and expensive. In fact, if the combustor is of annular type, it is difficult to reproduce an adequate periodicity between each sector without considering a considerable angular extension of the investigated section. This means to handle high mass flow rates of reacting flow at high pressure. Therefore, such kind of experimentation is difficult to sustain and the role of numerical predictions becomes crucial in understanding real working conditions of components.

A very small number of scientific works are available in the open literature concerning numerical investigations of combustor/turbine interaction. One of the main reasons is probably the need of powerful computational resources, that have been developed only in recent years. Another reason, in author opinion, is that the need of studying combustor/turbine interaction emerges because of the necessity to go more and more in detail in the comprehension of the aero-thermal aspects of

the components operation. The trust for this studies has been particularly strong in the last years, when emission regulations have become more restrictive and manufacturers needed to work hard on combustion chambers, leading to the study of lean burn combustion also in aero engines. The modern design for low emission means that the exit section of combustion chambers is characterized by an aggressive aero-thermal flow field, making necessary the simulation of combustor/turbine interaction in order to ensure components reliability.

The massive development of computer science in the last years has opened the way to numerical simulations for "multi-component" studies. The possibilities have been prospected in some US publications by Stanford researchers, in particular in the work by Shankaran et al. [33] in 2001 and from the work by Schlüter et al. [34] in 2003. This latter describes, for the first time, the development of a system aimed to simulate, through CFD, an entire turbomachinery by using jointly the URANS approach for compressor and turbine and the LES approach for the combustion chamber. Further developments of the work have been presented in the papers by Schlüter et al. [35], Kim et al. [36], Schlüter et al. [37, 38] and Medic et al. [39, 40].

In particular, Medic et al. [39] describes the simulation of a sector of 20° of an entire Pratt & Whitney turbofan engine using the integrated approach described above, including fan, compressor, combustor and turbine. This represent at the moment the most advanced work present in the open literature concerning the integration of turbomachinery components from the point of view of the aero-thermal analysis.

The method developed by the Stanford researchers is based on the use of different CFD solvers, each of them dedicated to a specific computational domain: the first URANS solver for fan and compressor, the LES solver for the combustion chamber and the second URANS solver for the turbine. Therefore two interfaces are present, the first one between compressor and combustor and the second one between combustor and turbine. The exchanges of information between each solver ensure the communications through the two interfaces and the convergence of the

system.

A different approach has been proposed in the works by Klapdor [41] and Klapdor et al. [42], where the interaction between combustor and high-pressure vanes has been studied by means of a single CFD solver through the RANS approach. In this case a single domain contains all the components under investigation.

A further numerical study of the combustor/turbine interaction has been addressed by Collado Morata [43]. She considered a multi-solver methodology, similar to the one proposed by the Stanford researchers, for integrated LES simulations of the combustion chamber and RANS simulations of the downstream turbine. In this case, different computational domains, characterized by the presence of an overlapped region, are considered.

To summarize, two main strategies are adopted by researchers for multi-component studies:

1. Single CFD solver that resolves the reactive flow through combustor and turbine. In this case a single computational grid, including combustion chamber and turbine, is considered.

2. The computational domain is divided into multiple sub-domains and hence multiple grids. Each of these is handled by a specific CFD solver. A mechanism for the exchange of information across the domain interfaces ensures spatial and temporal consistency between the solutions in the sub-domains and synchronization of the solvers.

The two approaches are characterized by benefits and disadvantages. First of all it must be considered that resolving the reactive flow across combustor and turbine using a single code is difficult from the points of view of accuracy and stability. In fact, Mach number varies strongly passing from the combustion chamber, where a nearly-incompressible subsonic flow is present, to the turbine, where a compressible high-Mach number flow is present. Even if substantial improvements have been done in the last years, difficultly a CFD solver is contemporary accurate and numerically stable in both these regimes. For this reason the use of

a specific solver for each component can provide the necessary accuracy and stability in its specific field. Moreover, it is worth to underline that solvers oriented for turbomachinery applications, are often not able to consider reactive flow, where multiple chemical species are transported. Similarly, a code that have been developed for the study of combustors, it is often not able to manage moving grids like the ones necessary to resolve the flow in rotating components. Considering these aspects, it is possible to state that the second strategy allows to use pre-existing codes with only minor modifications.The first one is difficultly applicable without massive modifications of pre-existing codes, not specifically developed for the study of combustor/turbine interaction.

Another practical aspects that can drive the selection of the multi-solver approach consists in the treatment of computational meshes. In fact, a lot of solvers for turbomachinery applications are "structured", i.e. they can treat only structured grids. This choice reduces computational costs with respect to unstructured grids but, having hypothesized that the solver is able to manage combustion, it would make difficult to include the combustion chamber in the computational domain because of its geometrical complexity. Due to the presence of a lot of geometric features, like injection holes, swirler, cooling systems, etc. unstructured grids are in fact more appropriate, ensuring relative ease in spatial discretization.

From a modeling point of view, another aspect favors the choice of separating the computational domain into sub-domains. Considering the characteristics of the flow field within these two components, it is possible to identify different needs in term of turbulence modeling. In fact, the combustion chamber is characterized by a mainly "unguided" flow with large-scale turbulence and strong unsteadiness while, within the turbine, a wall-bounded flow is present. For the first one the most appropriate strategies for turbulence modeling consists in scale-resolving methods like LES, SAS or DES. Such methodologies are currently not applicable at industrial level for the study of turbine stages, where RANS or URANS approaches with eddy viscosity turbulence models are the most used and relatively reliable. It is quite evident that a "hybrid" approach that

merges the two methodologies, has a better applicability in the case of multiple solvers rather than with a single one.

It can therefore be concluded that, having pre-existing CFD codes, the most direct approach is the multi-solver one. This is the case of this thesis, as will be described later in the text in Chapter 2.

# Part I

# Integrated CFD simulations of combustor and turbine

# Chapter 2

# Development of a numerical methodology for the study of combustor/turbine interaction

**Contents**



As underlined in the previous sections, the numerical study of combustor/turbine interaction requires integrated approaches. In the present

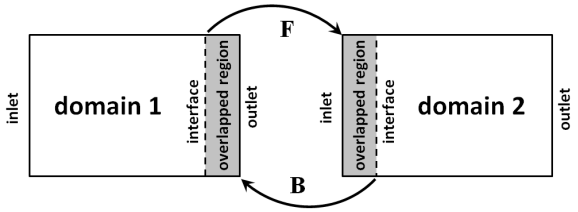


Figure 2.1: Schematic representation of the computational domains with overlapped regions; the exchange of information is also represented.

Chapter, a methodology for CFD simulation of coupled domains of combustion chamber and high-pressure turbine is described. Initially, a general description of the methods is given, then numerical methods for steady and unsteady simulations are presented.

## 2.1 General description of the approach for integrated CFD simulations

At the end of Chapter 1, an overview of the current approaches adopted for the CFD simulation of combustor/turbine interaction has been given. Benefits and disadvantages of the existing methodologies have been underlined. When pre-existing codes, dedicated respectively to combustion and aerodynamics in turbine stages, are used, the most direct and logical choice is using the "multi-code" strategy. This latter consists in dividing the computational domain into two sub-domains, separating combustor from turbine. In this way it is possible to benefit from the specificities of each single solver.

In the present work, a multi-code strategy similar to the one presented by Collado Morata [43], with partially overlapped domains, has been chosen for the integrated CFD simulations. A schematic representation of the division of the computational domain is reported in Figure 2.1. Two sub-domains are considered, called respectively "domain 1" and "domain 2". They share a common volume, depicted in gray, where the computational grids are overlapped and there is not, in general, a $1:1$

correspondence of the nodes, i.e. grids are not conformal. On the initial and final sections of the overlapped region in each sub-domain, two interfaces are present, as depicted in Figure 2.1. For the first domain, the first interface corresponds to the inlet section of the second domain, while the outlet section of the first domain corresponds with the second interface of the second domain. Across the interfaces the exchange of data between the two sub-domains happens. Two data set are exchanged as schematically depicted in Figure 2.1: the first one (**F**) forward from the first interface in the first sub-domain to the inlet section of the second sub-domain, while the second one (**B**) is exchanged backward from the second interface in the second sub-domain to the outlet section of the first sub-domain. As will be described later, as a function of the coupling methodology adopted, the data set **F** can contain different variables (a simple set of boundary conditions or conservative variables) while **B** always contains a static pressure map.

In order to give generality to the methodology, an approach based on non-conformal grids has been developed. An example of overlapped, non-conformal, hybrid unstructured grids is shown in Figure 2.2(a). To explain how exchanges of the data sets happen (Figure 2.2(b)), let's take into consideration the passage of **F**, the same is valid for **B**. First of all it is necessary to extract **F** from the first sub-domain. In the case of hybrid unstructured grids, the most general one, the grid nodes are not aligned on a plane (or a line, if the domains are two-dimensional like in the case of Figure 2.2(b)) corresponding to the inlet section of the second sub-domain. For this reason, it is necessary to project the required variables, stored in the centers of the cells crossed by the plane, on the plane itself. Then, it is possible to interpolate the variables from the plane extracted previously, to the inlet of the second sub-domain. To obtain an accurate passage of the variables, the interpolation uses, for a given point on the inlet of the second sub-domain, only the four nearest points located on the extracted plane and considers a weighted average based on the square of the inverse distance. The same procedure is used also to exchange **B** from the second sub-domain to the first one.

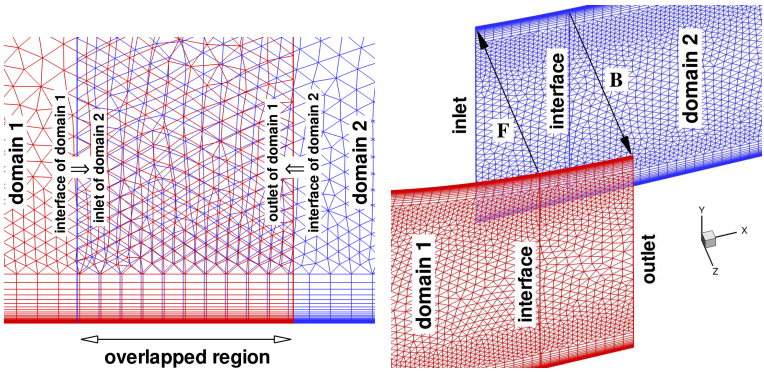


**(a)** overlapped hybrid unstructured grids

**(b)** data exchange

Figure 2.2: Schematic representations of the data exchange between overlapped domains; a two-dimensional case is shown for clarity.

## 2.2 Steady and unsteady methodologies: synchronization of the solvers

The method developed for the integrated study of combustor and turbine can be used both in steady and unsteady simulations. It is based on the iterative exchange of data between the CFD codes that manages the sub-domains and, for this reason, synchronization routines are needed to ensure that solvers proceed coordinately. The working principle which is the basis of the synchronization is slightly different in the case of steady simulations with respect to unsteady simulations. In the first case the only advance in iterations is required, while in the second one the advancement in iterations corresponds to an advancement in physical time. The synchronization process of both the cases is explained in the follow.

### 2.2.1 Steady methodology

The method is based on an iterative exchange of information between the two sub-domains. In the case of steady simulations, in order to reach

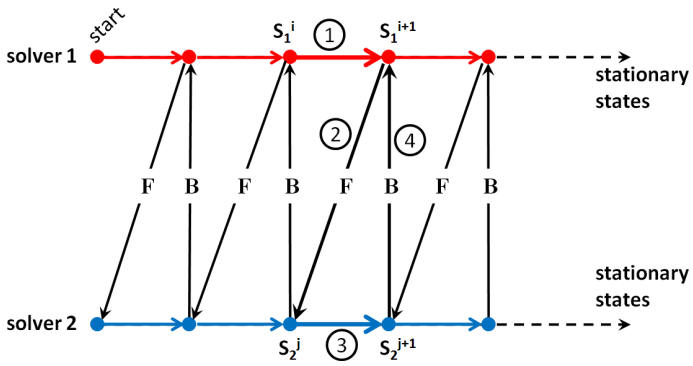


Figure 2.3: Steady synchronization process.

a converged state where continuity is ensured between all the quantities in the two sub-domains, a certain number of cycles is required. Figure 2.3 explains how these cycles happen and shows the sequence of the data exchanges. Solvers evolves through a series of stationary states, since time is not a variable of the computation. Looking at Figure 2.3, the i-th cycle can be summarized in the following four steps:

1. solver 1 is initially at the state $S_1^i$ and, after receiving the feedback **B** from solver 2, starts to iterate until to reach the steady state $S_1^{i+1}$; solver 2 waits

2. solver 1 passes **F** to solver 2

3. solver 2 is initially at the steady state $S_2^j$ and, after receiving **F** from solver 1, starts to iterate until to reach the steady state $S_2^{j+1}$; solver 1 waits

4. solver 2 passes **B** to solver 1 and the cycle restarts.

This scheme of synchronization is similar to the so-called "staggered scheme" proposed by Collado Morata [43] for the LES/RANS coupling, except for the difference that, in the present case, no advancement in time is required since simulations are steady. During the convergence

process each solver executes, separately from the other, a defined number of numerical iterations to evolve from one stationary state to the next one, in order to converge to a solution that ensure consistency in space between the two sub-domains. It is worth to underline that the number of numerical iterations executed for each cycle can be different from one solver to the other, in order to consider that solvers can be characterized also by very different convergence rates.

### 2.2.2 Unsteady methodology

When unsteady simulations are executed, consistency in space must be ensured in both space and time, taking into account that solvers can also advance in time with different time steps. In the case solvers run with the same time step ($\Delta t_1 = \Delta t_2$), the synchronization scheme, reported in Figure 2.4(a), is very similar to the one used for steady simulations. The only difference is that, now, solvers do no more advance through stationary states but in physical time. The four operations executed during each cycle are identical to the ones described for the steady case.

The case with $\Delta t_1 \neq \Delta t_2$ is slightly different. Considering Figure 2.4(b), where a case with $\Delta t_1 = \Delta t_2/4$ is reported, it must be considered that data exchange should happens when solvers are at the same physical time. For the case shown in Figure 2.4(b), the operations performed are the following:

1. solver 1 is initially at the state $S_1^i$, that corresponds to the time $t = t^i$, and, after receiving the feedback **B** from solver 2, starts to advance in time until to reach the state $S_1^{i+4}$, that corresponds to the time $t = t^{i+4}$; solver 2 waits

2. solver 1 passes **F** to solver 2. **F** contains time averaged data, taken on a moving window which amplitude can also be larger than the time interval $t^{i+4} - t^i$

3. solver 2 is initially at the state $S_2^j$, that corresponds to the time $t = t^j = t^i$ and, after receiving the time averaged **F** from solver 1,

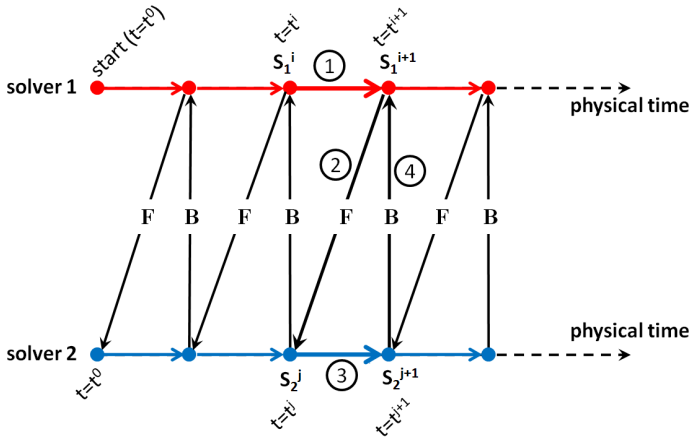


**(a)** case with $\Delta t_1 = \Delta t_2$

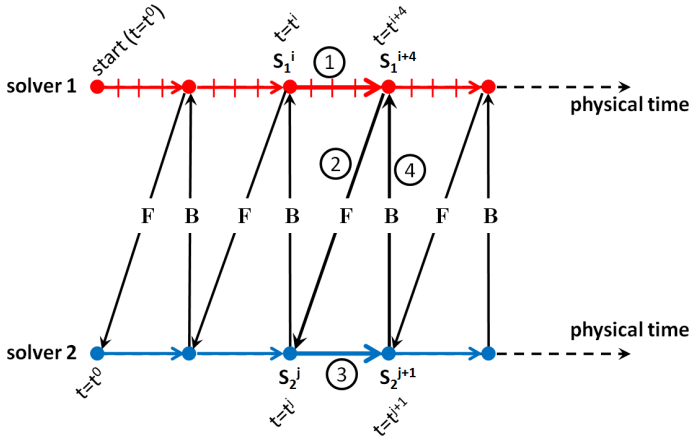


**(b)** case with $\Delta t_1 \neq \Delta t_2$ (example with $\Delta t_1 = \Delta t_2/4$)

Figure 2.4: Unsteady synchronization process.

advances in time until to reach the state $S_2^{j+1}$, that corresponds to the time $t = t^{j+1} = t^{i+4}$; solver 1 waits

4. solver 2 passes **B** to solver 1 and the cycle restarts.

The procedure has been explained for the particular case with $\Delta t_1 = \Delta t_2/4$ but it can be easily extended to the general case with $\Delta t_1 \neq \Delta t_2$. The reason why a case with $\Delta t_1 \neq \Delta t_2$ should be considered is that, advanced turbulence models like DES, SAS or LES can be applied for the resolution of the combustor domain. In such cases, in order to obtain an adequate time resolution for the turbulent structures, the time step will be, in general, lower than in the turbine domain where such methods are not practically applicable and URANS is a almost forced choice at the moment.

## 2.3 CFD solvers used

In this section a description of the CFD codes that have been used are described. Two CFD solvers have been considered for the activities presented in this thesis: an in-house code and a commercial one. The in-house code is called HybFlow and is developed at the department of Industrial Engineering of the university of Florence. The commercial code chosen is ANSYS® Fluent. A description of the two codes is given in the following.

### 2.3.1 The HybFlow code

The HybFlow code has been developed at the Department of Industrial Engineering of the University of Florence [44, 45]. It is a CFD solver written in the Fortran language, able to numerically resolve the Navier-Stokes equations in discretized form. HybFlow is based on the finite volumes approach and is able to manage both two-dimensional and three-dimensional domains. The solver treats unstructured grids, composed by elements of various geometry: hexahedrons, prisms, pyramids end tetrahedrons. This kind of grids has the advantage of allowing a rapid spatial discretization also in cases of very complex domains, for which structured meshes are difficult to realize. Moreover, contrary to what happens for structured grids, it allows the local imposition of a controlled mesh resolution, without propagating the effects through large

zones of the domain, where it would be unnecessary.

The code is parallelized by means of the use of the MPI libraries; a preprocessor allows to obtain a proper domain decomposition distributing the various partitions to parallel CPUs.

Both (U)RANS and LES methodologies are implemented in the code, however only the Reynolds-Averaged formulations of HybFlow are used in this thesis. The HybFlow solver is used only in absence of reacting flows, for this motivation, in the context of the integrated simulations described previously, it is oriented to resolve the second computational domain (see Figure 2.1), i.e. the turbine domain.

**Navier-Stokes equations in conservative form**

The HybFlow solver is based on the compressible Navier-Stokes equations written in their conservative form:

$$\frac{\partial \mathbf{Q}}{\partial t} + \frac{\partial \mathbf{f}_k}{\partial x_k} = \frac{\partial \mathbf{g}_k}{\partial x_k} + \mathbf{S} \qquad k = 1, 2, 3 \tag{2.1}$$

This vector formalism[1] allows also to include the transport equations relative to turbulence modeling. Focusing the attention on the Navier-Stokes equations, $\mathbf{Q}$ is the vector containing the solution in terms of $\rho$, $\rho u_k$, $\rho E$, where $E$ is the specific internal total energy; $\mathbf{Q} = [\rho, \rho u_1, \rho u_2, \rho u_3, \rho E]^T$. The system of equations 2.1 expresses the conservation laws for mass, momentum and energy, where different terms appear: unsteady, convective, diffusive and source. The convective and diffusive terms are respectively defined as follows:

$$\mathbf{f}_k = \begin{pmatrix} \rho u_k \\ \rho u_1 u_k + p\delta_{1k} \\ \rho u_2 u_k + p\delta_{2k} \\ \rho u_3 u_k + p\delta_{3k} \\ \rho E u_k + p u_k \end{pmatrix} \qquad \mathbf{g}_k = \begin{pmatrix} 0 \\ \tilde{\tau}_{1k} \\ \tilde{\tau}_{2k} \\ \tilde{\tau}_{3k} \\ \tilde{\tau}_{kh} u_h - \tilde{q}_k \end{pmatrix} \tag{2.2}$$

[1] In the follow, if not differently specified, the bold character will indicates vector quantities.

where $\tilde{\tau}_{kh}$ represents the generic element of the viscous stress tensor, while $\tilde{q}_k$ is the generic component of the conductive thermal flux. If a moving frame of reference is chosen, e.g. for rotating blade rows, the same formalism is adopted, but total quantities are the relative ones. The source term vector is given by:

$$\mathbf{S} = \begin{pmatrix} 0 \\ \mathbf{F}_{ce} + \mathbf{F}_{co} \\ \mathbf{F}_{ce} \cdot \mathbf{u} \end{pmatrix}, \qquad \begin{matrix} \mathbf{F}_{ce} = -\rho \boldsymbol{\Omega} \wedge (\boldsymbol{\Omega} \wedge \mathbf{R}) \\ \mathbf{F}_{co} = -2\rho(\boldsymbol{\Omega} \wedge \mathbf{u}) \end{matrix} \tag{2.3}$$

where $\mathbf{F}_{ce}$ and $\mathbf{F}_{co}$ indicates respectively centrifugal and Coriolis forces. Supposing that $x_1$ is the axis of rotation of the machine, it follows that.

$$\mathbf{S} = \begin{pmatrix} 0 \\ 0 \\ \rho\Omega^2 x_2 + 2\rho\Omega u_3 \\ \rho\Omega^2 x_3 - 2\rho\Omega u_2 \\ \rho\Omega^2 (x_2 u_2 + x_3 u_3) \end{pmatrix} \tag{2.4}$$

Finally, the thermodynamic relation between pressure, temperature (passing through the specific total internal energy) and density is imposed through the ideal gas equation of state.

$$p = \rho(\gamma - 1)\left(E - \frac{u^2}{2}\right) \tag{2.5}$$

**Spatial discretization**

As stated above, the solver uses the finite volumes method. Equations described in the previous section are integrated on each volume element of the grid. Thanks to the divergence theorem, spatial derivatives are converted into fluxes across the control surfaces of each element of the computational grid. Equations 2.1 assume the form:

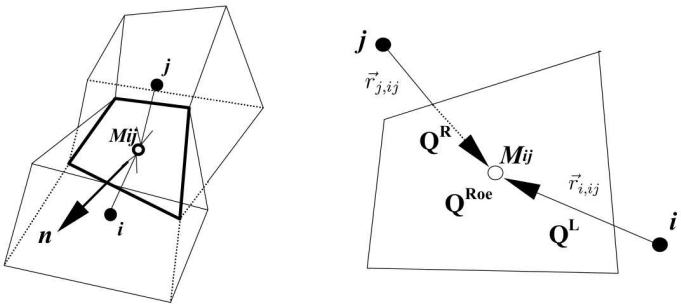


Figure 2.5: Spatial discretization.

$$\frac{\partial Q_i}{\partial t} + \frac{1}{V_i} \sum_{j=ne(i)} \overline{F}(Q_{ij}, \vec{n}_{ij}, \Delta A_{ij}) = \\ = \frac{1}{V_i} \sum_{j=ne(i)} \overline{G}(\nabla Q_{ij}, \vec{n}_{ij}, \Delta A_{ij}) \tag{2.6}$$

where $j = ne(i)$ the set of elements that share a face with the i-th element, $V_i$ is the element volume, $Q_{ij}$ the solution on the face, $\vec{n}_{ij}$ and $\Delta A_{ij}$ are respectively the normal and the area of the face shared between the elements. Functions $\overline{F}$ and $\overline{G}$ represents the numerical approximation of the fluxes of the vectors $\mathbf{f}$ and $\mathbf{g}$ of equations 2.1, through the faces of the considered element. Calculation of the fluxes across a face is performed using the MUSCL (*Monotone Upstream-centered Schemes for Conservation Laws*) scheme, using the solution stored in the center of the cells that share the same face. Concerning the discretization of the convective flux, it can be subdivided into two phases: reconstruction and evolution. The first one is necessary to define the states $Q^L$ and $Q^R$ on the two portions divided by the face, while the evolution phase allows to update the solution on the face center, indicated with $M_{ij}$ in Figure 2.5

In this second phase it is hypothesized that the evolution of the solution $Q_{M,ij}$ in the medium point is described by a Riemann problem[2],

[2]It is a initial value problem for the one-dimensional Euler equations, with the

characterized by the interaction of two initial states, equal to $Q^L$ and $Q^R$. This allows, in the evolution phase to take into account the direction of propagation of the characteristic waves across the face. The solution used for the Riemann problem is the approximated one proposed by Roe, for which fluxes are calculated as follows:

$$\begin{aligned}&\overline{F}(Q_{ij}, \vec{n}_{ij}, \Delta A_{ij}) = \\ &= \frac{1}{2}\left[F(Q_i^L, \vec{n}_{ij}, \Delta A_{ij}) + F(Q_j^R, \vec{n}_{ij}, \Delta A_{ij})\right] + \\ &- \frac{1}{2}|K(Q_{ij}, \vec{n}_{ij}, \Delta A_{ij})|\Delta Q_R^L\end{aligned} \tag{2.7}$$

The convective flux of equation 2.7 is:

$$F(Q, \vec{n}, \Delta A) = f_k n_k \cdot \Delta A \tag{2.8}$$

while $K$ is the Jacobian matrix, defined by:

$$K(Q, \vec{n}, \Delta A) = \left[\frac{\partial f_k}{\partial Q} n_k\right] \Delta A \tag{2.9}$$

In the Roe scheme, the average state $Q_{ij}$ is calculated by averaging the solution as follows:

$$\begin{aligned}\chi &= \sqrt{\frac{\rho_R}{\rho_L}} \quad , \quad \rho_{ij} = \rho_L \cdot \chi \\ u_{1,ij} &= (u_{1,R} \cdot \chi + u_{1,L})/(1+\chi) \\ u_{2,ij} &= (u_{2,R} \cdot \chi + u_{2,L})/(1+\chi) \\ u_{3,ij} &= (u_{1,R} \cdot \chi + u_{1,L})/(1+\chi) \\ H_{ij} &= (H_R \cdot \chi + H_L)/(1+\chi)\end{aligned} \tag{2.10}$$

where $H$ is the specific total enthalpy.

Let's now clarify how the calculation of $Q_L$ and $Q_R$ is performed. The

initial condition constituted by a step between two states, which remains constant on the left and the right of the step. In the case of the finite volume method, the step is located in correspondence of the face shared by two adjacent cells.

following interpolation is considered:

$$Q_L = Q_i + \Phi_i \nabla Q_i \cdot \vec{r}_{i,ij} \quad , \quad Q_R = Q_j + \Phi_j \nabla Q_j \cdot \vec{r}_{j,ij} \tag{2.11}$$

where $\nabla Q_i$ and $\nabla Q_j$ are respectively the solution gradients in the cell centers $i$ and $j$, while $\vec{r}_{i,ij}$ and $\vec{r}_{j,ij}$ are the vectors that connects the cells centers with the center of the common face (see Figure 2.5). The coefficients $\Phi_i$ e $\Phi_j$, that assumes values between 0 and 1, are called "slope limiters" and are introduced to ensure solution monotonicity also in presence of strong non-linear phenomena like shocks. The accuracy of the numerical scheme decreases from second order to first order when such coefficients goes to zero, making the scheme more dissipative. The value of the $\Phi$ coefficients is based on what follows. Given the element $i$, for all the elements adjacent to it ($j = ne(i)$) the following calculation is performed:

$$(\phi_i)_j = \begin{cases} \min\left(1, \frac{\overline{Q}_j^{max} - Q_i}{Q_L - Q_i}\right) & \text{per} \quad Q_L - Q_i > 0 \\ \min\left(1, \frac{\overline{Q}_j^{min} - Q_i}{Q_L - Q_i}\right) & \text{per} \quad Q_L - Q_i < 0 \\ 1 & \text{per} \quad Q_L - Q_i = 0 \end{cases} \tag{2.12}$$

then $\Phi_i$ is defined by:

$$\Phi_i = \min[(\phi_i)_1, (\phi_i)_2, (\phi_i)_3, \ldots, (\phi_i)_{j=ne(i)}] \tag{2.13}$$

This limiting approach results sensitive to the solution gradients and is necessary to control its effect in the regions where, even if strong gradients are present, solution is continuous; this is to avoid a deterioration of the accuracy. To do this, it is necessary to measure the pressure variation across through two contiguous elements. Limiting is only actuated when such variation overcome an imposed threshold, otherwise $\Phi_i$ and $\Phi_j$ are assume equal to 1. The solution gradients can be calculated in HybFlow with two different schemes. The first one based on the divergence theorem (Green-Gauss) and the second one based on a least squares methodology.

**Implicit time-marching**

The steady solution of the equations is calculated through an implicit time-marching procedure. The system of equations to be resolved is representable as:

$$\frac{\partial \mathbf{Q}}{\partial t} + \mathbf{R}(\mathbf{Q}) = 0 \tag{2.14}$$

where $\mathbf{Q}$ is the solution vector, including all the values referred to the cells centers, while $\mathbf{R}$ is the residuals vector[3]. The implicit method leads to write the system 2.14 in the form:

$$\frac{\Delta \mathbf{Q}^n}{\Delta t^n} = -\mathbf{R}(\mathbf{Q}^{n+1}) \qquad \Delta \mathbf{Q}^n = \mathbf{Q}^{n+1} - \mathbf{Q}^n \ , \ \Delta t^n = t^{n+1} - t^n \tag{2.15}$$

Expressing the residuals vector through a first order approximation, centered at the time $t^n$, it is possible to obtain:

$$\underbrace{\left[\frac{\mathbf{I}}{\Delta t} + \frac{\partial \mathbf{R}(\mathbf{Q})}{\partial \mathbf{Q}}\right]^n}_{\mathbf{A}} \Delta \mathbf{Q}^n = -\mathbf{R}(\mathbf{Q}^n) \tag{2.16}$$

where $\mathbf{I}$ is the identity matrix and $\frac{\partial \mathbf{R}(\mathbf{Q})}{\partial \mathbf{Q}}$ is the Jacobian matrix of the residuals vector with respect to the solution. The solver is based on a numerical approach for the calculation of the Jacobian matrix that consists in considering that a not null $ij$ block with dimensions $5 \times 5$ exists only for $i$ and $j$ corresponding to contiguous elements. Each of these blocks can be calculated numerically as follows:

$$\frac{\partial \mathbf{R}_i(\mathbf{Q})}{\partial \mathbf{Q}_j} \approx \left[\frac{\mathbf{R}_i(\mathbf{Q} + \epsilon \vec{e}_h) - \mathbf{R}_i(\mathbf{Q})}{\epsilon}\right]_{h=h_1(j),h_2(j)} \tag{2.17}$$

where $h_1(j)$ and $h_2(j)$ are the initial and final indexes of the solution vector, corresponding to the element $j$ within the overall $\mathbf{Q}$ vector, $\vec{e}_h$ the corresponding unit vector and $\epsilon$ an arbitrarily small number.

The resolving scheme used in the code performs a main loop, on all

[3] If relative motions between the elements are not present the source term $\mathbf{S}$ is not present.

the grid faces, composed by the following steps:

1. calculate the numerical flux 2.7 using the solutions stored in the cell centers of the adjacent elements that share the face
2. by using $\epsilon$, alternatively perturb left and right states of the face
3. calculate fluxes with the perturbed solutions
4. calculate derivative as differences between perturbed and unperturbed fluxes
5. update the blocks of the jacobian matrix with the derivatives calculated at the previous step

The matrix $A$ indicate in the linear system of equation 2.16, for unstructured grids, results to be sparse and not symmetric. Its inversion is then particularly computationally demanding and can be unstable for high values of $\Delta t$. For the inversion, HybFlow makes use of the Generalized Minimal RESidual method (GMRES), with a ILU(0) type preconditioning. The time step of the method is defined by:

$$\Delta t = \mathrm{CFL} \cdot \frac{\Delta}{V + a} \tag{2.18}$$

where $\Delta$ is the characteristic dimension of the element, $V$ the velocity magnitude and $a$ the sound speed. $\Delta t$ assumes different values as a function of the local solution. The CFL number can be selected by the user or defined according to the following law:

$$\mathrm{CFL}^{n+1} = \mathrm{CFL}^{n} \cdot \left( \frac{|\Delta Q|^{n-1}}{|\Delta Q|^{n}} \right)^{sp} \tag{2.19}$$

From this latter it is possible to note how, when the solution tends to the converged one, CFL is automatically increased. This allows to have stability in the initial phases of the computation and to benefit from an increased convergence rate in the final parts of the simulation. Moreover, the exponent *sp*, generally equal to 1, can be reduced in order to obtain a better stabilization in the initial phases.

**Unsteady approach**

The HybFlow solver uses the dual time-stepping method for time-dependent problems. It offers the advantage, with respect to explicit schemes, to make the time step selection independent from stability criteria. With the dual time-stepping approach, the numerical derivative $\left(\frac{\partial}{\partial \tau}\right)$ is added to the physical system 2.1, obtaining the system:

$$\frac{\partial \mathbf{Q}_i}{\partial \tau} + \left[\frac{\partial \mathbf{Q}_i}{\partial t} + \mathbf{R}_i(\mathbf{Q}) - \mathbf{S}_i(\mathbf{Q})\right] = 0 \tag{2.20}$$

Defining a vector of "unsteady residuals" like:

$$\mathbf{R}_i^*(\mathbf{Q}) = -\left[\frac{\Delta \mathbf{Q}_i}{\Delta t} + \mathbf{R}_i(\mathbf{Q}) - \mathbf{S}_i(\mathbf{Q})\right] \tag{2.21}$$

equations assume the same form of the ones that describe a steady problem:

$$\frac{\partial \mathbf{Q}_i}{\partial \tau} = \mathbf{R}_i^*(\mathbf{Q}) \tag{2.22}$$

The physical time derivative is approximated by using a backward second order derivative:

$$\frac{\Delta \mathbf{Q}_i^{n+1}}{\Delta t} = \frac{3\mathbf{Q}_i^{n+1} - 4\mathbf{Q}_i^n + \mathbf{Q}_i^{n-1}}{2\Delta t} \tag{2.23}$$

The similitude with a steady problem allows using the time-marching method also in this case to obtain the convergence of the numerical unsteady term $\left(\frac{\partial \mathbf{Q}}{\partial \tau}\right)$. When a defined criterion on the convergence of the unsteady residual is satisfied, the physical solution at the time $n+1$ is updated.

### 2.3.2 ANSYS® Fluent

The commercial code ANSYS® Fluent is also used in the context of the integrated simulations and a general and concise description is given in the following. For detailed information about Fluent, see [46].

It is a finite volume unstructured CFD code, able to resolve two or

three dimensional problems, in which different numerical schemes and physical models are implemented. Both pressure-based and density-based solvers are present, respectively more suitable for low and high Mach number flows. Different schemes of spatial discretization are available, as well as different type of gradients discretization and time discretization.

Turbulence can be modeled using both the RANS approach and some scale-resolving methodologies. RANS turbulence models includes fully turbulent models like Spalart-Allmaras, $k$-$\epsilon$ and its variants, $k$-$\omega$ and its variants and the Reynolds stress model. Transitional models are also available, like the transitional versions of the SST model and the $k_T$-$k_L$-$\omega$. Different scale resolving methods are implemented in the code, like: LES, DES and SAS.

The code is also able to manage flows with multiple chemical species and combustion. In particular, concerning this latter, the three main categories of fuel mixing can be modeled: premixed, non-premixed and partially-premixed combustion. Different types treatments for the chemistry of reacting flows in gaseous phase can be chosen as well as different kinds of approaches for the interaction between turbulence and chemistry.

More detailed descriptions of the applied models will be given treating the specific applications proposed in the continuation of the thesis.

## 2.4 Exchange of variables between solvers

In 2001, Shankaran et al. [33] formulated a classification of the possible ways to couple different CFD solvers, in increasing hierarchy of complexity:

- *loosely coupled systems:* the presence of interfaces can be treated by each solver through only boundary conditions
- *moderately coupled systems:* the primary or primitive variables at the interface are exchanged between the codes
- *tightly coupled systems:* in addition to the primary variables, fluxes are also exchanged across the interface

- *simultaneously coupled systems:* the algorithmic variables of codes are directly exchanged.

It is quite clear that the first approach, based on the only boundary conditions is the most direct one and it is the most easy to implement. The opposite happens for the last methods listed, where the algorithmic variables are exchanged and modifications in the codes are required. In this thesis, only the first two methodologies are considered, depending on what solvers are used.

The loosely coupled methods is chosen when a coupling between different instances of the ANSYS® Fluent solver are considered to resolve the sub-domains. Instead, the moderately coupled method is used when the sub-domains are resolved jointly by ANSYS® Fluent and HybFlow.

### 2.4.1 RANS/RANS and URANS/URANS coupling

As previously described in section 2.1, two data sets are exchanged between the solvers: forward (**F**) and backward (**B**). This exchange is executed in every case, regardless of the fact that the simulation is steady or unsteady. However, depending from what solvers are used (Fluent/Fluent or Fluent/HybFlow), the content of **F** changes while **B** is always constituted by a static pressure map.

#### Loosely coupled methodology

As stated before, when two independent instances of ANSYS® Fluent are used to solve the sub-domains, the loosely coupled methodology is considered. This means that the interfaces are treated simply through the imposition of boundary conditions. In such case, the two data sets assume the following content:

$$\mathbf{F} = \{p_0, e_1, e_2, e_3, T_0, k, \omega\} \qquad \mathbf{B} = \{p\} \tag{2.24}$$

where $p_0$ is the stagnation pressure, $e_i$ with $i = 1, 2, 3$, are the components of the unit vector indicating the flow direction, $T_0$ is the stagnation

temperature, $k$ is the turbulent kinetic energy and $\omega$ its specific dissipation rate. Concerning these last two quantities, here we suppose that in both the sub-domains a $k-\omega$ based two-equations turbulence closure is used. However this is not binding since, with the RANS approach, an algebraic relation between $\omega$ or $\epsilon$ and $k$ can be used to derive an universal value of the turbulent length scale that could eventually be imposed in the second sud-domain if a different turbulence closure is used, provided that a two equation eddy viscosity model is used. It is worth to underline that all the exchanged quantities are functions of the spatial coordinates.

It should be noted how, regardless from the type of information exchanged, conditions imposed along the other boundaries, not involved in the coupling process, must be chosen in order to ensure a well-posed problem in both the sub-domains.

The implementation of the data interpolation and the management of code synchronization has been done respectively through "user-defined functions[4]" [47] and Scheme scripting [48], with which is possible to introduce external routines in the commercial software.

### Moderately coupled methodology

When the sub-domains are solved using jointly ANSYS® Fluent and HybFlow, the moderately coupled approach is used. In this case, the two data sets exchanged assume the following content:

$$\mathbf{F} = \{\rho, \rho u, \rho v, \rho w, \rho e_0, \rho k, \rho\omega\} \qquad \mathbf{B} = \{p\} \tag{2.25}$$

where $\rho$ is density, $u$,$v$ and $w$ are the components of the velocity vectors and $e_0$ is the total internal energy. In this way, the conservative variables are passed from the first solver to HybFlow where RANS equation in conservative form are solved. The same considerations done for the loosely coupled approach concerning turbulence quantities are valid also in this case.

When the data set $\mathbf{F}$ is provided by Fluent to Hybflow, an interpo-

[4]Functions written in C language and compiled directly within ANSYS® Fluent

lation is firstly done along the inlet section of the domain, as previously explained in section 2.1. After that, the information contained in **F** is directly used to calculate fluxes along the inlet faces, in a similar way it is done for internal faces of the computational grid. The only difference with respect to internal faces is that a first order approximation in space is adopted on the inlet interface, since no information upstream of the corresponding interface section for the first solver are provided.

### 2.4.2 SAS/URANS coupling

The flow field inside a gas turbine combustion chamber is intrinsically characterized by strong unsteadiness and large scale turbulence. In that context, the so-called "scale resolving methods" guarantees substantial improvements with respect to the classical (U)RANS approach in reproducing the turbulent field. The SAS method (Scale Adaptive Simulation), formulated by Menter and Egorov [49], is an advanced URANS approach able to reproduce spectral content for unstable flows. The model is based on the transport of the von Karman length scale in the framework of a URANS simulation, based on which it is possible to adjust the turbulence model to resolved structures, resulting in a LES-like behavior in the unsteady regions of the flow field, without altering the RANS behavior in stable regions. Transport equations resolved by the SAS model are the same of the SST $k-\omega$ model by Menter [50] except for the fact that an additional source term is introduced in the transport equation of turbulence dissipation [46, 49] in order to allow the local adaptation to small turbulence scales, up to a lower limit imposed by the local grid size.

By controlling the local grid size, it is possible to obtain LES-like behaviors in the regions of the flow characterized by unsteadiness like, for example, wakes or recirculating zones and to obtain a typical RANS solution in regions where turbulence scales do not need to be resolved. For this reason, the SAS approach represents an interesting alternative to LES at industrial level, limiting the high computational costs imposed by this latter. In view of the study of combustor/turbine interaction, the SAS approach is retained interesting for the application to the computa-

tional domain of combustion chamber.

Similarly to the (U)RANS/(U)RANS coupling methodology described previously, the SAS/URANS method is based on the same scheme of variable passage between sub-domains. Also the approaches that can be used are the loosely coupled one or the moderately coupled one. However, some differences are present with respect to the (U)RANS/(U)RANS case. First of all, recalling Figure 2.4(b) where the synchronization process is illustrated, since the first solver advances in time with a smaller time step with respect to the second one, **F** must contain appropriately averaged quantities. As mentioned before, SAS is able to provide a resolution of the small scale turbulence but the same is not valid for URANS. It follows that the time step used in the two sub-domains must be chosen taking into account this aspect. The ratio between the two time steps is obviously dependent from the specific case analyzed an is not possible to generalize. However, it is worth to underline the importance of selecting an adequate strategy to calculate the time averaged quantities of the data set **F** to be passed to the URANS solver.

Lets consider the generic signal (for example a velocity signal in a turbulent flow field obtained with the SAS method) represented by the solid line in Figure 2.6 and lets analyze two different average signals, representative of the condition to be passed to the URANS solver. Supposing to use a moving average, the selection of its amplitude is crucial. For the signal of Figure 2.6, composed by about 700 discrete points, if a moving average based on 50 points is chosen, the high-frequency content is reduced with respect to the original signal. Increasing the amplitude of the moving windows to 200 points, the high-frequency fluctuations of the original signal are considerably filtered out. The moving average acts like a low-pass filter, allowing the determination of the type of fluctuations that are passed from SAS to RANS. The appropriate amplitude should not allow turbulence high-frequencies to pass to the URANS domain, and contemporaneously should allow to the main unsteadiness to be transmitted to the URANS domain. An appropriate choice for the time amplitude of the moving window is to guarantee that it is of the

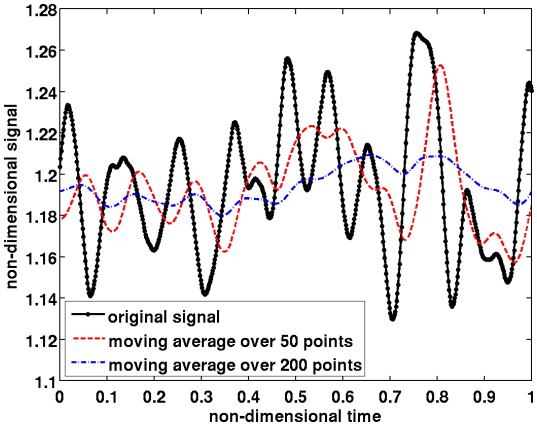


Figure 2.6: Effect of the amplitude of the moving average.

same order of the turbulence integral time scale [43].

Another crucial aspect is represented by the passage of the turbulence quantities from SAS to URANS. A solution of a scale adaptive simulation contains both "resolved" and "modeled" turbulent kinetic energy. The first one is linked to the velocity fluctuations of the solution, while the second one is a transported scalar that contributes to the effective viscosity. Obviously, in the LES-like regions, resolved turbulence is the main contribute while the opposite happens in the URANS regions. In the present approach, the resolved part of turbulent kinetic energy is calculated as follows:

$$k_{res} = \frac{1}{2}\left(u_{rms}^2 + v_{rms}^2 + w_{rms}^2\right) \tag{2.26}$$

where

$$u_{rms} = \sqrt{\frac{\sum_{j=i-N}^{j=i}\left(u_j - \overline{u}\right)^2}{N+1}} \tag{2.27}$$

assumed $i - N$ the index of the time step at which the moving window starts and $i$ the index of the time step correspondent to the end of the

moving window. With this notation, the average is calculated at the time step $i$ of the SAS simulation, on $N+1$ samples (separated by $N$ time steps):

$$\overline{u} = \frac{\sum_{j=i-N}^{j=i} u_j}{N+1} \tag{2.28}$$

Therefore, being $\Delta t$ the time step of the SAS solver, $N\Delta t$ is the time amplitude of the moving window. Analogous expressions can be derived in the other directions for $v_{rms}$ and $w_{rms}$.

The total turbulent kinetic energy takes into account the resolved one and the modeled one through a simple addition:

$$k_{tot} = k_{res} + k_{mod} \tag{2.29}$$

where the $k_{mod}$ contribution is the turbulent kinetic energy handled by the transport equation of the SST model in the RANS regions.

Pope [51] gives a practical criterion to determine the local quality (in space and time) of turbulence resolution:

$$M(\vec{x},t) = \frac{k_{mod}(\vec{x},t)}{k_{res}(\vec{x},t) + k_{mod}(\vec{x},t)} \tag{2.30}$$

$M$ ranges from 0 to 1 and, according to Pope [51], if $M \leq 0.2$ the turbulence resolution is adequate to LES. Depending on the grid spacing and the time step, some zones of the SAS domain could be characterized by values of $M$ close to unity, meaning that a RANS solution is obtained. Since the value of $k_{tot}$ is calculated in the SAS domain and used in the URANS one, the approach is general, but obviously it is appropriate to maintain $M \leq 0.2$ in the zones of interest of the SAS domain.

For the loosely coupled methodology the quantities exchanged by the solvers are

$$\mathbf{F} = \left\{\overline{p_0}, \overline{e_1}, \overline{e_2}, \overline{e_3}, \overline{T_0}, k_{tot}, \omega\right\} \qquad \mathbf{B} = \{p\} \tag{2.31}$$

where the overlined quantities are averaged on the moving window and $k_{tot}$ is calculated as previously described. For the treatment of turbulence specific dissipation rate $\omega$ the following approximation is introduced. Af-

ter obtaining the coupled RANS/RANS solution on the two domains (needed to start the SAS/URANS coupled computation), the obtained field of $\omega$ at the inlet section of the URANS domain is frozen and maintained constant (but not uniform) during all the SAS/URANS computation. This is a simplifying assumption that avoids the complex calculation of the local dissipation rate during the computation. Such approach is similar the one used by Collado Morata [43] for the LES/RANS coupled simulation of a turbulent pipe flow, where a fixed distribution of the length scale, based on theoretical considerations, was assumed. Despite the approximation, the methodology used for the treatment of $\omega$ allows the imposition of an appropriate distribution of turbulence dissipation at the inlet of the URANS domain also in cases where theoretical formulations of the length scale are not available (e.g. on the combustor/turbine interface).

# Chapter 3

# Validation of the numerical methodology

**Contents**



Methodologies described in the previous Chapter has been validated on some test cases in order to assess their correct implementation and the adequacy of the results provided. Results of such validations are presented in the next sections. The following test cases are considered:

- Sajben transonic diffuser: used to validate the steady RANS/RANS coupling methodology

- Vortex shedding downstream a linear cascade: used for the URANS/URANS coupling methodology
- Turbulent pipe flow: validation of the SAS/URANS coupling

## 3.1 Sajben transonic diffuser

The transonic diffuser experimentally studied by Salmon et al. [52] has been used to validate the steady RANS/RANS coupling methodology. This test case is quite common in literature concerning validation of CFD codes and a considerable amount of data can be found in [53]. The Sajben diffuser has been considered also by Klapdor [41] for the validation of a novel solver oriented to the study of combustor/turbine interaction.

### 3.1.1 Description of the test case

The two-dimensional computational domain is shown in Figure 3.1(a). The channel is defined by a lower straight wall and an upper shaped wall that makes the passage converging-diverging. The throat section, whose height is $H^* = 44mm$, is located at $x/H^* = 0$. The computational domain extends from $x/H^* = -4.04$ to $x/H^* = 8.65$. As shown in Figure 3.1, when coupled simulations are considered, the domain is divided into two partially overlapped domains. The first one is extended from the inlet section up $x/H^* = -0.65$ while the second one has its inlet section at $x/H^* = -1$ and arrives up to $x/H^* = 8.65$. The axial extension of the overlapped region is equal to $0.35H^*$. Computational grids, generated with the commercial software Centaur$^{TM}$ [54] are shown in Figure 3.1(b). As it is possible to observe, grids are hybrid unstructured and non-conformal in the overlapped region. The presence of 30 prismatic layers is enforced at the wall in order to obtain a better discretization of the boundary layer. The height of the first prismatic layer ensures $y^+ < 1$ along all the surfaces, compatibly with the integration of turbulence quantities up to the wall, without using wall functions. Since the flow is characterized by the presence of a shock in the diverging part of

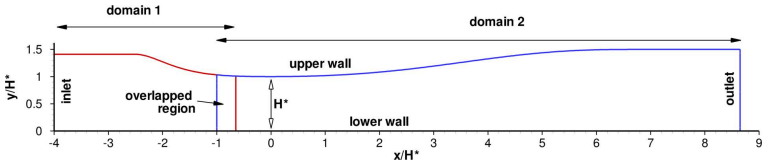


**(a)** domain

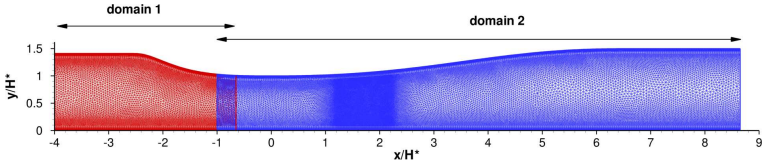


**(b)** grid

Figure 3.1: Computational domain and grid of the Sajben diffuser test case.

the channel, grid has been refined in the region where such shock was expected, in order to improve the resolution of the flow where strong gradients are present.

A grid sensitivity analysis has been performed in order to define the optimal grid resolution. The final grid of the entire domain (without subdivisions) is composed by about $75k$ elements. The two sub-domains, used for the coupled simulations, have been generated with the same grid parameters used for the entire domain and are respectively composed by about $16k$ and $62k$ elements.

The so-called "weak shock case" [53] has been selected as operating point. Boundary conditions corresponding to it are reported in Table 3.1. Values of 5% and $H^*/20$ has been assumed respectively for turbulence intensity and length scale. Steady RANS simulations have been performed using the $k-\omega$ turbulence model by Wilcox [55]. In order to assess the effectiveness of the coupling methodologies, four simulations have been performed. Two coupled simulations, Fluent/HybFlow and Fluent/Fluent, have been compared with two simulations where the whole domain has been resolved once with HybFlow and once with ANSYS®

| | | |
|---|---|---|
| inlet total pressure | 1.344 | [bar] |
| inlet total temperature | 277.8 | [K] |
| outlet static pressure | 1.107 | [bar] |
| inlet turbulence level | 5 | [%] |
| inlet turbulence length scale | $H^*/20$ | [m] |

Table 3.1: Boundary conditions used for the Sajben diffuser test case (weak shock case).

Fluent. The Fluent/HybFlow coupled simulation has been performed exchanging conservative variables from the first sub-domain to the second one (moderately coupled methodology explained in section 2.4), while the Fluent/Fluent coupling has been performed with the loosely coupled methodology. Concerning the coupled simulations, 10 coupling cycles, each one composed by 200 numerical iterations, have been used to reach convergence starting from decoupled solutions. The pressure-based solver has been used in all the domains resolved with ANSYS Fluent® , while HybFlow is density-based.

### 3.1.2 Results

Before to compare the results of the coupled simulations with experimental data and simulations performed on the entire domain, it is worth to make some comments on the convergence process of the coupled simulations. Figure 3.2 shows the progressive reduction of the mass-flow imbalance between the outlet section of the first sub-domain and the inlet section of the second one. The mass flow rates reported are referred to a width of the channel of $1mm$ since the domains have been extruded in normal direction in order to obtain a quasi-3D domain. Figure 3.2(a) is relative to the Fluent/HybFlow computation, while Figure 3.2(b) is relative to the Fluent/Fluent run. In both the cases the mass imbalance is almost entirely removed in four coupling cycles, even if with a different dynamic. In fact, in the Fluent/HybFlow case the mass imbalance is not reduced monotonically, differently from the Fluent/Fluent case. This can be attributed to the nature of the HybFlow solver and more in detail

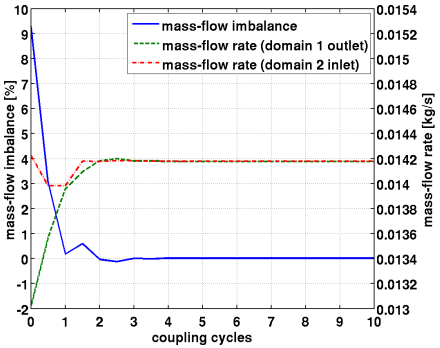


**(a)** Fluent/HybFlow

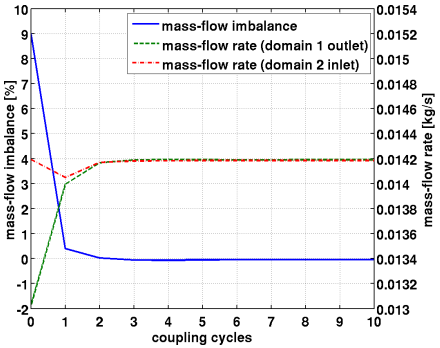


**(b)** Fluent/Fluent

Figure 3.2: Mass flow convergence history of the coupled simulations.

to the oscillations of the solution due to the changes of inlet conditions that cause numerical transients in the time marching procedure. The maximum final absolute value of mass imbalance, registered in the Fluent/Fluent computation is about 0.02%. Moreover, this error is comparable with the differences in the mass flow estimation obtained comparing the solutions obtained simulating the entire diffuser in a unique domain with the commercial code and the in-house one.

Figure 3.3 shows the convergence history of the axial component of the momentum equation for the Fluent/HybFlow computation. Residuals de-

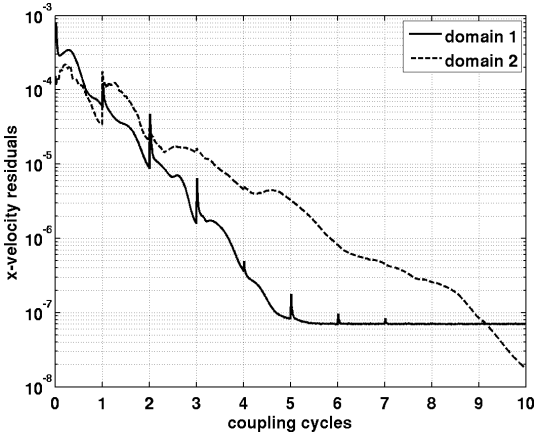


Figure 3.3: Convergence history of the axial velocity residual in the coupled Fluent+HybFlow case.

crease by more than three orders of magnitude in both the sub-domains. It is interesting to note the discontinuities of the residuals that occur at the start of each coupling cycle due to the modifications of the boundary conditions on the interfaces. As the calculation advances these discontinuities tend to vanish since solutions across the two domains became continuous. It is also possible to observe how the convergence rate of the in-house solver is lower than for the commercial code.

Figure 3.4 shows the contours of Mach number for all the simulations performed. Looking at Figures 3.4(a) and 3.4(b), relative to the coupled simulations, it is possible to observe a smooth passage from the first to the second sub-domain. For all the cases, flow accelerates up to a Mach number of 1.2 downstream of the throat section then passes to subsonic conditions through a shock. The shock position is predicted slightly differently in the four simulations. In particular, the simulation of the entire domain with ANSYS® Fluent leads to predict the highest flow acceleration, with the shock positioned downstream with respect to all the other cases. The opposite happens in the case of the entire domain resolved with HybFlow. As expected, an hybrid behavior has been found in the

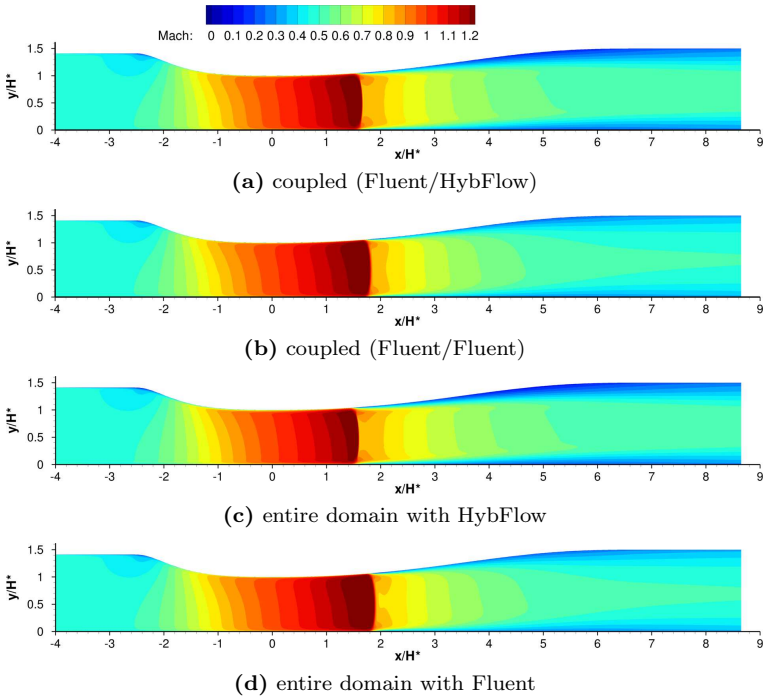


**(a)** coupled (Fluent/HybFlow)

**(b)** coupled (Fluent/Fluent)

**(c)** entire domain with HybFlow

**(d)** entire domain with Fluent

Figure 3.4: Mach number distributions: comparison between coupled domains and entire domains.

Fluent/HybFlow case, while the Fluent/Fluent computation provides a result very similar to the one relative to the simulation of the entire domain with the commercial code, although a slight difference in the shock position is present.

The coherency of the solutions in the overlapped regions is demonstrated in terms of Mach number profiles in Figure 3.5(a) for the Fluent/HybFlow case and in Figure 3.5(b) for the Fluent/Fluent case. The full-domain computations are taken as references since no experimental data are available in that zone. Profiles are taken at $x/H^* = -0.825$, in the middle between the two interfaces. Mach number distributions

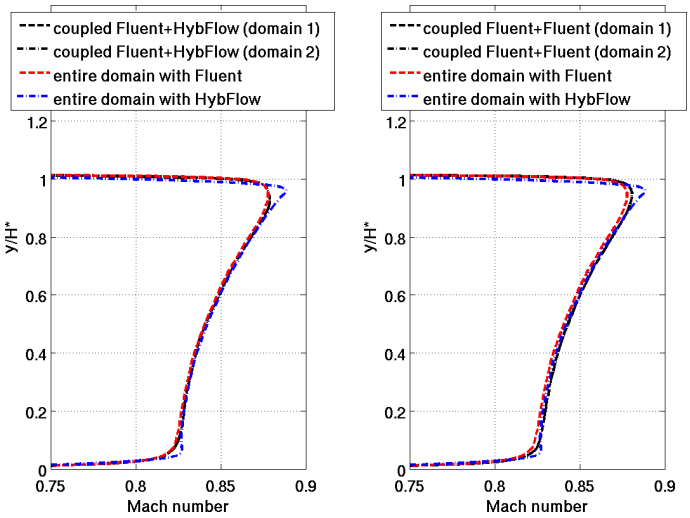


**(a)** coupled Fluent/HybFlow and entire domains

**(b)** coupled Fluent/Fluent and entire domains

Figure 3.5: Mach number profiles in the overlapped zone.

relative to the two sides of the overlapped regions (black lines in Figure 3.5) are almost equal, indicating an effective transfer of information between the domains. As evidenced before, the main differences in determining the results with respect to the full-domain computations are again ascribable to the code selected.

Figures 3.6(a) and 3.6(b) show the comparison between numerical simulations and experimental data in terms of pressure distributions along respectively upper and lower walls of the channel. A general qualitative good agreement between computations and experiments is reached. The main differences with respect to experimental data are present immediately downstream of the position of the shock measured experimentally ($x/H^* \simeq 1.5$). In the interval $1.5 < x/H^* < 2.5$, the uncertainty in the prediction of the shock position, postponed in all the simulations with respect to the experiments, leads to underestimates the local pressure. Such underestimations are more marked for the cases where the domain

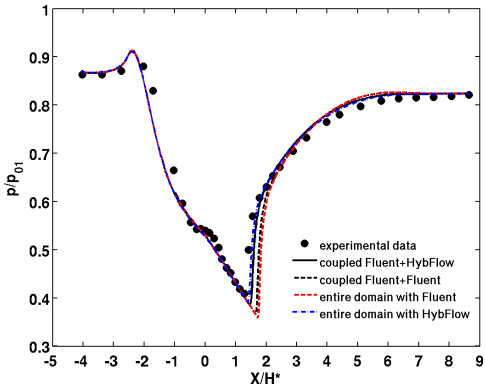


**(a)** upper wall

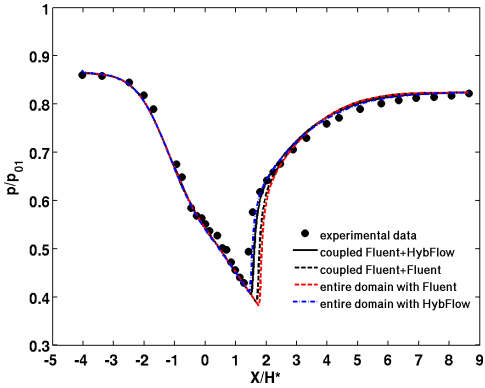


**(b)** lower wall

Figure 3.6: Pressure distribution along upper and lower walls: comparison with experimental data.

is simulated with Fluent, either entirely or separately. However, the pressure distribution does not differ sensibly between these latter simulations, leading to conclude that the main differences in reproducing the flow field are due to the code selected rather that to the use of the coupling method. In other words, in the analyzed case, the domain separation affects the solution only in a limited way.

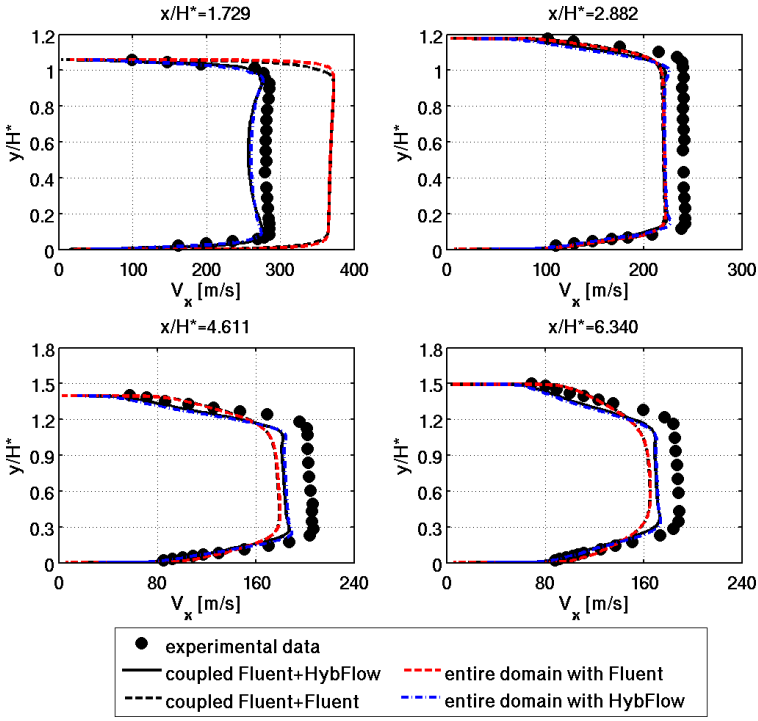


Figure 3.7: Axial velocity profiles at four positions downstream to the throat section.

The axial velocity profiles at four different positions downstream to the throat section are reported in Figure 3.7. The first profile ($x/H^* = 1.729$) is taken immediately upstream of the shock. As commented previously the computations executed with the full domain with Fluent and the Fluent/Fluent one predicts a stronger acceleration of the flow. This aspect is particularly evident by comparing the numerical results with the experimental data. Downstream of the shock all the simulations are more in line with the experimental data, with a general underestimation of the axial velocity (tendency evident also in literature [53]), coherently with the overestimation of the static pressure present in the terminal part

of the channel (Figures 3.6(a) and 3.6(b)). Again, the main differences between numerical results can be ascribed to the ability of each solver in reproducing the flow field, more than to the application of the coupling methods. In particular, ANSYS® Fluent has evidenced the tendency to predict more "rounded" velocity profiles far downstream to the shock position ($x/H^* = 4.611$ and $x/H^* = 6.340$ in Figure 3.7).

## 3.2 Unsteady flow in a linear cascade

The high-subsonic flow through the linear cascade experimentally investigated by Sieverding et al. [56] is studied in this section with the aim to validate the unsteady coupling methodology based on the URANS/URANS technique. Sieverding et al. [56] provided both time-averaged and time-resolved experimental data, including the pressure distribution along the trailing edge of the profile, which is very difficult to reproduce numerically due to the strong unsteadiness and the complexity of the flow field in the base region.

### 3.2.1 Description of the test case

The instrumented blade is reported in Figure 3.8, taken from the work by Sieverding et al. [56]. The geometric definition of pressure and suction surfaces is reported by Cicatelli and Sieverding [57]. As observable from Figure 3.8 the blade is prismatic and two fences are present at the ends in order to reduce the onset of secondary flows. It follows that it is possible to treat the flow as two-dimensional. Pressure taps are positioned along the blade surface at midspan. The blade is equipped with a rotatable trailing edge cylinder instrumented with a pneumatic pressure tap and a fast response pressure sensor that allow the acquisition of the pressure signal along all the semi-circumference of the trailing edge itself. The geometrical characteristics and operating conditions of the cascade are reported in detail in Table 3.2

Figure 3.9 shows a schematic of the two-dimensional computational domain. The inlet section is positioned 0.5 chords upstream of the leading

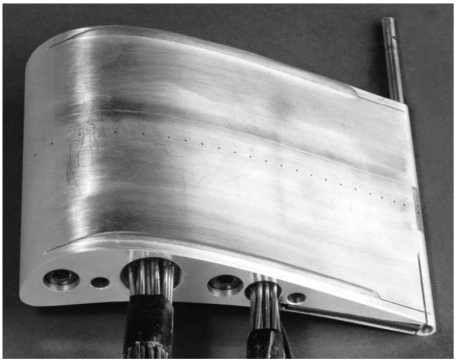

Figure 3.8: Instrumented blade (Sieverding et al. [56]).

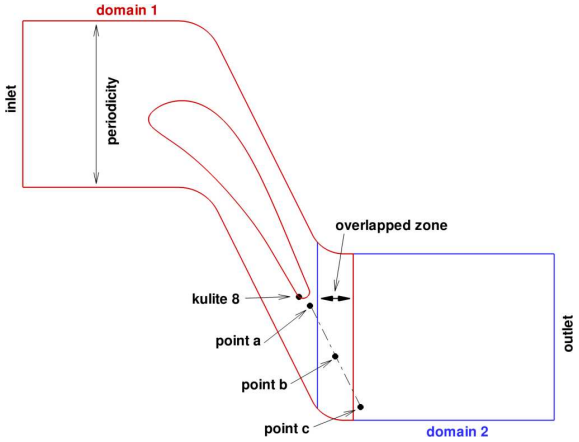


Figure 3.9: Computational domain.

edge while the outlet section is located 1 chord downstream of the trailing edge of the profile. For the coupled simulations the domain has been divided into two sub-domains. The first one is extended from the inlet section up to about 0.27 axial chords downstream to the trailing edge while the second one is overlapped to the first one on a portion equal to about 0.22 axial chords and is extended up to the outlet section. The

| | | |
|---|---|---|
| chord length | 140 | [mm] |
| axial chord to chord ratio | 0.656 | |
| pitch to chord ratio | 0.696 | |
| trailing edge thickness to chord ratio | 0.0531 | |
| stagger angle | $-49.83$ | [deg] |
| inlet total pressure | 1.4 | [bar] |
| inlet total temperature | 280 | [K] |
| outlet isentropic Mach number | 0.79 | [bar] |
| inlet turbulence level | 1 | [%] |
| Reynolds number (based on chord and outlet velocity) | $2.8 \cdot 10^6$ | |

Table 3.2: Geometrical characteristics and operating conditions from Sieverding et al. [56].

four "numerical probes", referred as kulite 8, point a, point b and point c in Figure 3.9, are used to monitor the static pressure during the unsteady solution and to evaluate the effectiveness of the communication between the coupled sub-domains. The "kulite 8" probe is the same reported in [56] and experimental data are available for it.

The computational grid used for the coupled simulations is reported in Figure 3.10. It is an hybrid unstructured grid generated with the software Centaur$^{\text{TM}}$ [54]. Thirty layers of quadrilateral elements are used at the wall to accurately reproduce the boundary layer, while the remaining part of the domain is filled with triangular elements. A preliminary grid sensitivity analysis has been performed in order to choice the appropriate grid resolution. The entire domain counts about $134k$ elements, while the count is slightly higher in the case of coupled sub-domains due to the presence of the overlapped region. A low Reynolds grid has been generated near wall, where $y^+$ of the first element is below the unity along all the blade surface. As visible in Figure 3.10, particular attention has been dedicated to obtain a gradual refinement of the region downstream of the trailing edge, which is also the location of the interfaces.

Simulations have been performed using the pressure-based solver implemented in ANSYS® Fluent both for the entire domain and the coupled sub-domains. For the coupled simulations the loosely coupled approach

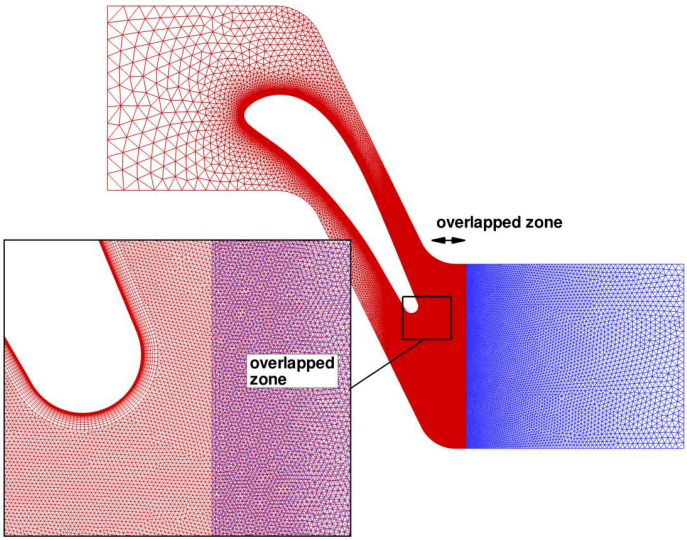


Figure 3.10: Computational grid used of the coupled calculations.

has been used. Unsteady simulations have been performed, starting from the steady solution, with a time step of $1\mu s$, also in the two sub-domains of the coupled case. Such time step ensures an adequate reproduction of vortex shedding phenomenon that occurs downstream of the trailing edge. The turbulence model used is the fully turbulent SST $k-\omega$ by Menter [50]. Time averaged quantities have been calculated over 60 vortex shedding periods after reaching statistical convergence. In the case of unsteady coupled simulation the exchange of information between the two sub-domains happens for each physical iteration without averaging (see Figure 2.4(a)), being the time step the same in both the sub-domains.

### 3.2.2 Results

Figure 3.11 shows the Mach number distributions obtained from both steady and unsteady simulations. The effect of the domain subdivision for the steady computations can be evidenced comparing Figure 3.11(a)

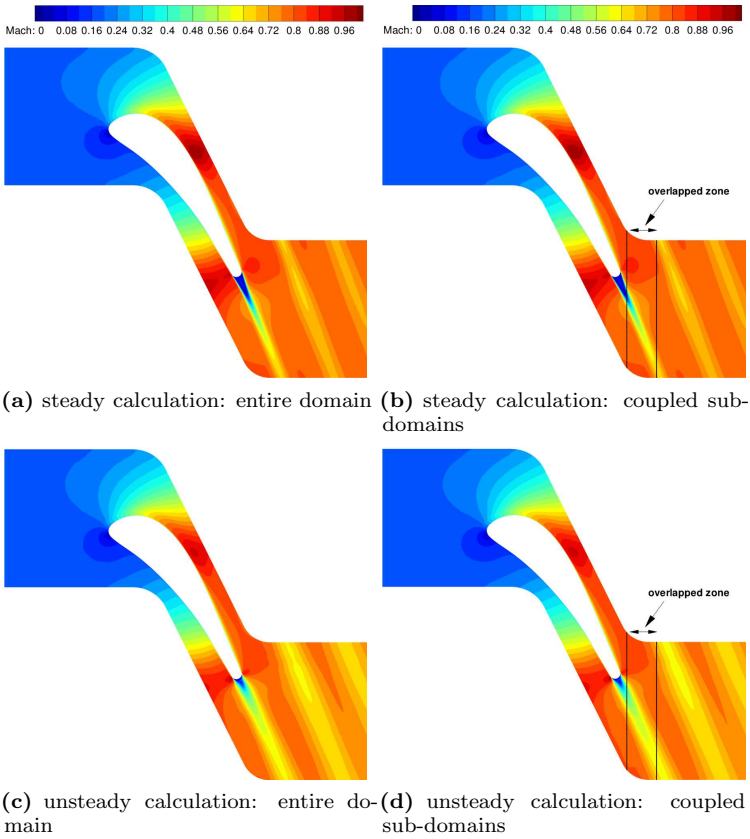


**(a)** steady calculation: entire domain

**(b)** steady calculation: coupled sub-domains

**(c)** unsteady calculation: entire domain

**(d)** unsteady calculation: coupled sub-domains

Figure 3.11: Contours of Mach number obtained from steady and unsteady simulations of the entire domain and the coupled sub-domains.

with 3.11(b) and for the unsteady computations, comparing 3.11(c) with 3.11(d). Mach number distributions obtained from the steady simulations are almost identical, confirming that the application of the coupling method to divided sub-domains does not cause substantial alteration of the solution for a steady case. A slightly different behavior can be noted for the unsteady cases. Despite the two solutions (Figures 3.11(c) and

3.11(d)) are very similar, some differences can be noted in the amplitude of the high-Mach number zone downstream of the throat section. Another aspect that appears from Figure 3.11 is that, independently from the fact that the domain is divided or not, the predicted Mach number is higher in the steady cases, although the choking conditions are not reached. To evaluate the effectiveness in the transfer of turbulent quanti-

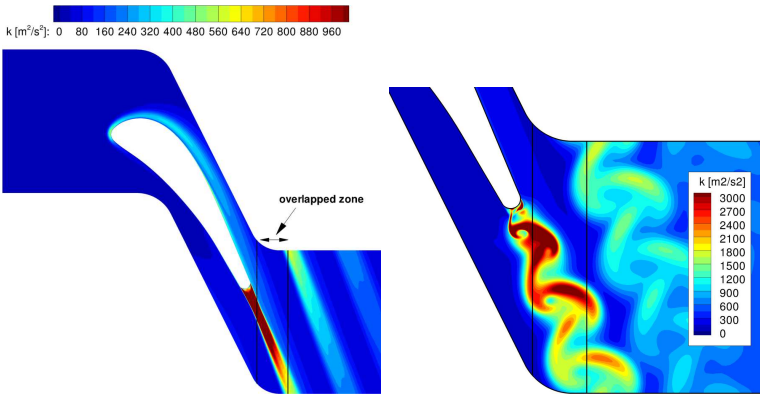


**(a)** steady simulation

**(b)** unsteady simulation (detail of instantaneous $k$ downstream of the trailing edge)

Figure 3.12: Turbulent kinetic energy obtained with steady and unsteady coupled simulations.

ties across the two sub-domains, distributions of turbulent kinetic energy within the domain has been reported in Figure 3.12. Figure 3.12(a) shows the turbulent kinetic energy obtained with the steady coupled simulation; as it is possible to observe, no appreciable discontinuities can be observed. Figure 3.12(b) reports the instantaneous turbulent kinetic energy distribution downstream the trailing edge resulting from the coupled unsteady simulation. An evident vortex shedding is reproduced by the simulation, with the characteristic coherent structures originated from the trailing edge. Also in this case, discontinuities in the turbulent kinetic energy fields are very limited.

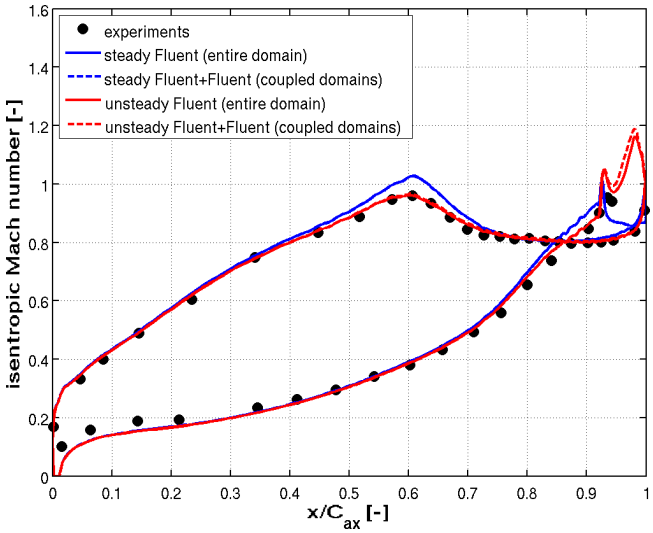


Figure 3.13: Isentropic Mach number distribution: comparison between experimental data and numerical simulations.

The isentropic Mach number distributions obtained numerically are compared with those obtained experimentally by [56] in Figure 3.13. Results relative to the steady simulations on the entire domain and on the coupled sub-domains are coincident, as already commented previously looking at the Mach number distributions, but some discrepancies with respect to the experimental data can be observed. For $0.4 < x/c_{ax} < 0.75$ the steady simulations overestimate isentropic Mach number, while they underestimate it in the trailing edge region. This latter tendency is evident also in the work by Léonard et al. [58], on the same test case, and in the one by Gehrer et al. [59], performed on a linear cascade with a geometry different from the one analyzed here. A significant improvement of the results is obtained with the unsteady simulations, underlining the importance of the unsteadiness in determining the blade loading, especially along the suction side. A significant difference between steady and unsteady simulations is present in the trailing edge region, due to the effects

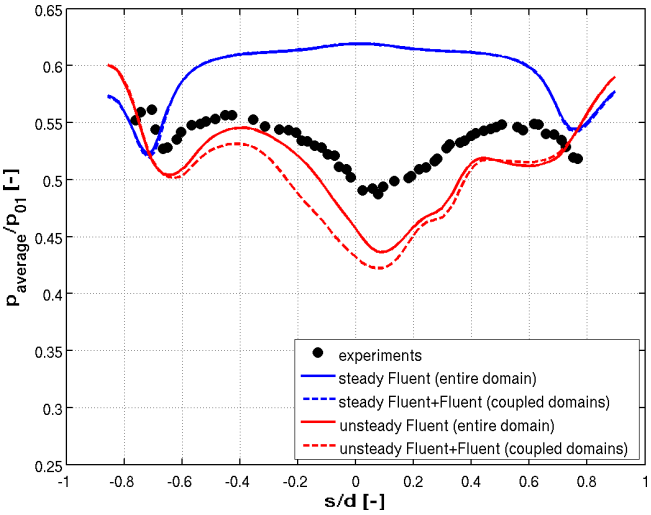


Figure 3.14: Non-dimensional static pressure distribution along the trailing edge circle: comparison between experimental data and numerical simulations (pressure side for negative $s/d$).

of the vortex shedding phenomenon that are completely missed with a steady approach. In such region, some differences between the unsteady simulations of the entire domain and the coupled sub-domains can be observed. Looking at the pressure distribution around the trailing edge circle, reported in Figure 3.14 as a function of the curvilinear coordinate, non-dimensionalized with respect to the trailing edge diameter, trends evidenced above are confirmed. In fact, steady simulations overestimate the base pressure and, in addition, do not reproduce its distribution neither from a qualitative point of view. On the contrary, the qualitative behavior is reproduced quite well with the unsteady simulations, even if an underestimation is present with respect to the experimental data. As observable in Figure 3.14, the unsteady results obtained with the entire domain and the coupled sub-domains differ in the interval $-0.6 < s/d < 0.5$ with the major discrepancies along the pressure side portion (the maximum percentage difference of 6.8%, considering the entire domain as reference,

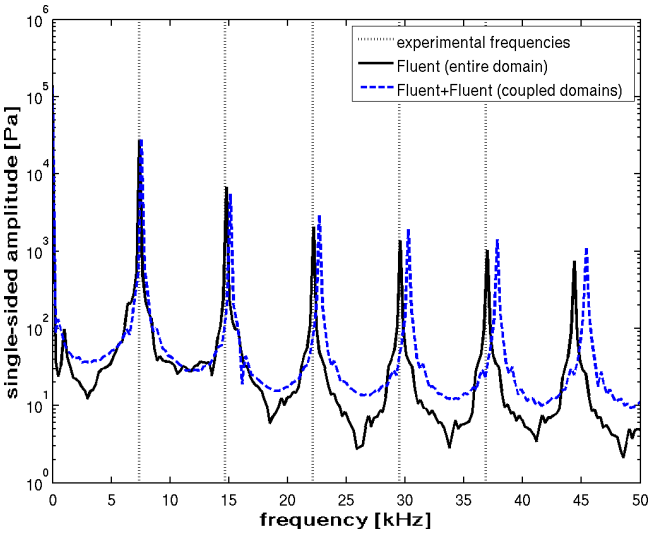


Figure 3.15: Frequency contents of the signal measured on the point referred as "kulite 8" in Figure 3.9: comparison between experimental data and numerical simulations.

is located at $s/d = -0.16$). To better understand the reason of such discrepancies it is appropriate to compare the numerical results with the experimental data available in the point referred as "kulite 8" in Figure 3.9. Such point is in fact located immediately upstream to the trailing edge circle along the pressure side. Figure 3.15 reports a comparison between the experimentally measured frequencies and the discrete Fourier transformation (obtained by means of a FFT) of the numerical pressure signal. The computation on the entire domain reproduces very well the five harmonics present in the experimental data while the coupled simulation tends to overestimate such frequencies, with a shift that increases progressively moving to higher frequencies. Moreover, except for the two lower harmonics, the amplitude of the higher ones is slightly larger in the coupled case. Figure 3.16 shows the pressure fluctuations downstream of the trailing edge, in the points a, b and c of Figure 3.9. The frequency

shift evidenced on the kulite 8 point is confirmed also for these points. The maximum percentage differences in terms of local pressure peaks are $+8\%$, $-1.1\%$ and $-0.9\%$ respectively for point a, b and c, considering the entire domain as reference. It is interesting to underline such percentage errors becomes smaller moving away from the trailing edge, where the unsteadiness are generated. From a numerical point of view, the differences found for the coupled simulations with respect to the entire domain can be attributed to the treatment of boundary conditions of the two interfaces (the outlet section of the first sub-domain and the inlet section of the second sub-domain). These boundaries are not completely transparent to the pressure waves that travels across them since no NRBC (Non-Reflecting Boundary Conditions [60]) have been used. For this reason, waves originated from the trailing edge and traveling in the flow direction are partially reflected by the outlet section of the first domain. Similarly, waves propagating from the second sub-domain to the first one, like for example a pressure wave reflected from the outlet of the second sub-domain, are partially reflected by the inlet section of the second sub-domain. Generally speaking, the problem of spurious reflections across domain boundaries has been resolved in literature using NRBC or NSCBC (Navier-Stokes Characteristics Boundary Conditions [61, 62]). However, such methods are not directly applicable to the boundary conditions exchanged between coupled sub-domains. In facts, these are not satisfactory for the reproduction of the time-dependent influence of a downstream URANS domain on the upstream one because tend to filter the unsteadiness arriving from this latter, creating a discontinuity in the pressure field. Very recently, Vagnoli and Verstraete [63] proposed a solution to this problem, based on the theory of characteristic waves. Instead of using the classical approach for the imposition of boundary conditions, they enforced directly the exchange of characteristic waves, reaching to adequately reproduce the influence of the downstream domain on the first one. The future implementation of such approach could represent an interesting potential improvement to the work presented in this thesis.

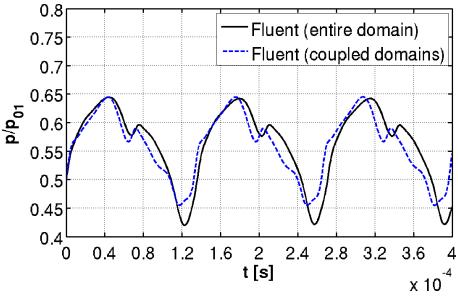


**(a)** point a

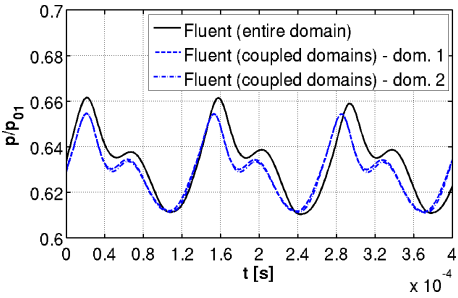


**(b)** point b

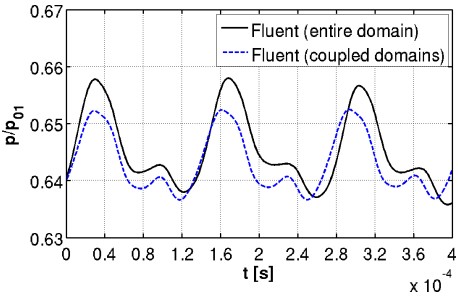


**(c)** point c

Figure 3.16: Time-resolved non-dimensional pressure signal in the points a,b and c indicated in Figure 3.9: comparison between simulation with entire domain and coupled sub-domains.

## 3.3 Turbulent pipe flow

This test case has been used to validate the unsteady SAS/URANS coupling methodology presented in section 2.4.2. It has been derived from an analogous test case studied by Collado Morata [43] during the development of a LES/RANS coupling method.

### 3.3.1 Description of the test case

The computational domain has a very simple geometry, represented by a cylindrical volume with a diameter of $3mm$ and a length equal to six diameters. It has been divided into two sub-domains, as reported in Figure 3.17(a), respectively resolved with SAS method and the URANS method in ANSYS® Fluent. The extension of the first sub-domain goes

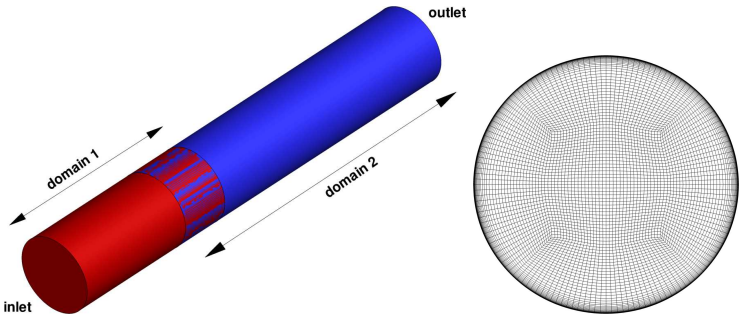


**(a)** domain **(b)** grid section

Figure 3.17: Computational domain and grid of the tubular domain.

from the origin of the coordinate system to $7mm$ in x direction while the second one is in the interval $5mm \leq x \leq 13mm$. The axial extension of the overlapped region is equal to $2mm$. The working fluid is air having a total temperature of $300K$ and a bulk velocity of $U_b = 100m/s$. Under these conditions, the Reynolds number, based on tube diameter and bulk velocity, is about $2 \cdot 10^4$; therefore a turbulent flow is expected. According to Collado Morata [43], an average turbulent velocity profile has been

imposed on the inlet section of the first sub-domain by means of the empirical power law:

$$\overline{u}(r) = \frac{1}{2}U_b(n+2)(n+1)\left(1-\frac{r}{R}\right)^n \tag{3.1}$$

where R is the external radius of the tube and $n = 1/7$. An inlet turbulence intensity of 10% has been imposed through the velocity fluctuations introduced by means of the vortex method (Mathey et al. [64]). A uniform static pressure is imposed on the outlet section of the second sub-domain.

Structured multi-block grids have been generated for both the domains using ANSYS® ICEM CFD. A transversal section of the grid is shown in Figure 3.17(b). It is an O-grid composed by 112 elements in y and z directions that provides an element dimension of $0.04mm$ in the core of the flow, while the grid size in axial direction is $0.1mm$. Grid dimension is reduced gradually in radial direction close to the wall in order to ensure $y^+ < 1$. Both the sub-domains have the same grid resolution. The overall domain counts $1.3536 \cdot 10^6$ elements: $4.7376 \cdot 10^5$ in the first sub-domain (SAS) and $8.7984 \cdot 10^5$ in the second one (URANS).

Different time steps have been used for the two domains. In the SAS domain $\Delta t_1 = 1.5 \cdot 10^{-7} s$ has been chosen, while for the URANS domain $\Delta t_2 = 10\Delta t_1 = 1.5 \cdot 10^{-6} s$. In this way, for the SAS domain, the CFL number obtained is:

$$CFL = \frac{\overline{u}(r=0) \cdot \Delta t_1}{\Delta x} \simeq 0.18 \tag{3.2}$$

ensuring an appropriate time resolution (according to [65], $CFL < 1$ should be guaranteed in the "LES" zones.).

Calculation, based on the loosely coupled strategy, has been started from coupled RANS solutions of the two sub-domains. Due to the different time steps ($\Delta t_2 = 10\Delta t_1$), the exchange of boundary conditions was set every ten time steps for the first sub-domain (passage of **F** to the second sub-domain) and every time step for the second one (passage of **B** to the first sub-domain). In this way, a "relaxed" variation of the

back pressure on the outlet section of the SAS domain is obtained. Ten numerical iterations have been executed for each physical iteration of the SAS solver while twenty numerical iterations were necessary to obtain an adequate convergence of the physical iterations of the URANS solver due to the larger time step. The amplitude of the moving window for the computation of the average quantities of the data set **F** has been set to $0.6 \cdot 10^{-4} s$, corresponding to 1/3 of the convective time of the entire tube. More in detail, the time interval of the moving window corresponds to 400 time steps of the SAS domain and, consequently, to 40 time steps of the URANS domain.

After a first initial phase necessary to reach statistical convergence, 14 convective times ($0.00252s$) has been simulated to collect time statistics.

It was necessary to use non-reflecting boundary conditions (NRBC) on the outlet sections of both the sub-domains, since if simple reflective conditions were used, spurious pressure waves reflections induce unphysical strong fluctuations of the solution.

### 3.3.2 Results

Figure 3.18 shows an instantaneous map of the axial velocity field along a longitudinal section of the domains (the URANS solution is shown in the overlapped region). As it is possible to observe, the SAS solution is characterized by velocity gradients in axial and radial directions, caused by the synthetic turbulence generation imposed on the inlet section. On the contrary, due to the effect of the moving window that acts like a low-pass filter in the transmission of data from SAS to URANS, the second domain is mainly characterized by radial velocity gradients.

The effect of the averaging process passing from SAS to URANS is clearly observable in Figure 3.19, where the axial velocity signal obtained on a point positioned along the axis of the tube, in correspondence of the inlet section of the second sub-domain, is shown. Such point is shared between the SAS and the URANS sub-domains, allowing the comparison of the solution on the two sides. Figure 3.19(a) reports the signal on a time window large about 1.1 convective times. As it is possible to

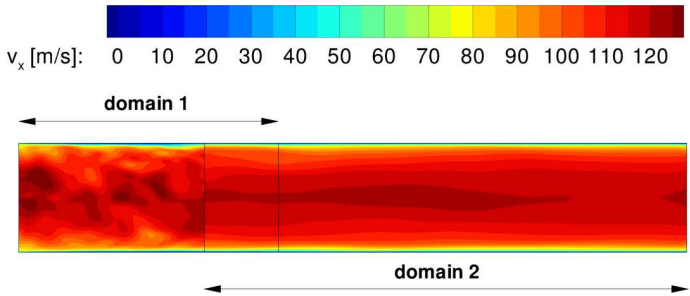


Figure 3.18: Instantaneous axial velocity field; URANS solution is shown on the overlapped region.

observe, on the SAS side, the velocity signal is characterized by strong high-frequency fluctuations while, after the averaging process, the same point on the URANS side is characterized by a filtered signal. Figure 3.19(b) reports the same signal of Figure 3.19(a), but showing a narrow time window. Points represent the discrete samples that compose the signals. As it is possible to note, the time resolution of the SAS signal is higher than the URANS one, coherently with the relation $\Delta t_2 = 10\Delta t_1$. On a plane corresponding to the inlet section of the second sub-domain, a study of the transmission of turbulent quantities has been done. Details are reported in Figure 3.20 in terms of time averaged quantities. Figure 3.20(a) reports the ratio between the modeled and the total turbulent kinetic energy. As explained previously, this quantity allows establishing if an adequate resolution of turbulence is obtained in scale-resolving simulations. An appropriate solution in terms of turbulence resolution is obtained when $M \leq 0.2$ [51]. The quantity $M$ has been calculated in both the sub-domains. As shown in Figure 3.20(a), the SAS solution evidences an LES behavior along most of the radius ($M \leq 0.2$), while $M > 0.2$ only in the outer parts of the domain, near wall, where the peak of turbulent kinetic energy is present. On the opposite, for the URANS solution, $M$ is close to unity along most of the radial coordinate, indicating that turbulence is mainly modeled, as expected from a Reynolds-averaged simulation. $M$ is not equal to unity in the URANS

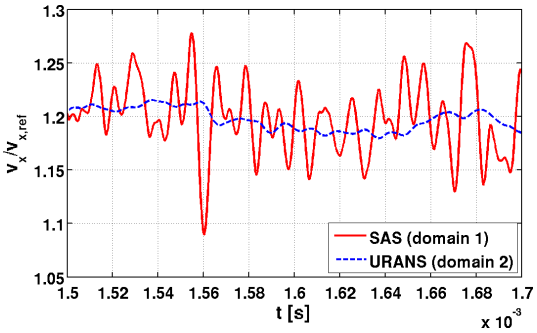


**(a)** time window on about 1.1 convective times

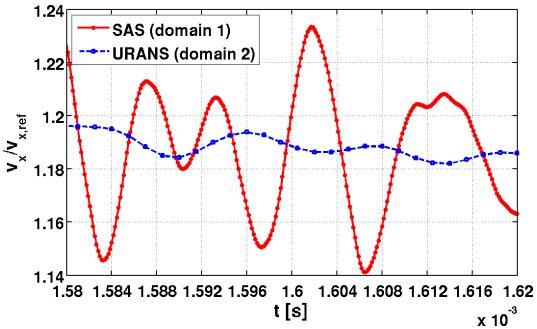


**(b)** time window on about 0.22 convective times

Figure 3.19: Axial velocity signal on a point positioned along the axis of the tube in correspondence of the inlet section of the second sub-domain.

solution since a portion of the turbulent kinetic energy is still present in terms of velocity fluctuations (see Figure 3.19). Made these premises, the average total turbulent kinetic energy profiles (containing resolved and modeled terms), shown in Figure 3.20(b), are coherent, except for a slight underestimation of $k_{tot}$ in the URANS solution.

As explained previously, turbulence specific dissipation rate is not directly passed from the SAS computation to the URANS one. The approximation of assuming a frozen field of $\omega$, deriving from the RANS/RANS

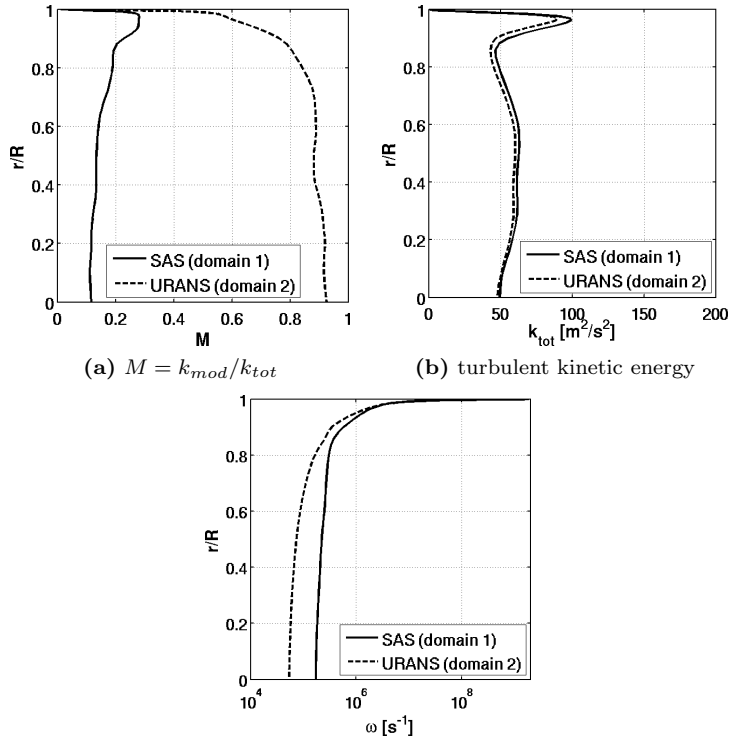


**(a)** $M = k_{mod}/k_{tot}$ **(b)** turbulent kinetic energy

**(c)** specific dissipation rate

Figure 3.20: Time averaged radial profiles of $M$ [51], turbulent kinetic energy and specific dissipation rate on a section positioned in correspondence of the inlet of the second sub-domain.

coupled simulation, at the inlet of the second sub-domain is done. For this reason, as shown in Figure 3.20(c), radial profiles of $\omega$ differ sensibly in the core of the flow, while tends to the same value at the maximum radius as a consequence of the imposition of the same boundary condition along the wall in terms of $\omega$.

In order to verify that the domain subdivision does not affect sensibly the solution, velocity profiles obtained with the SAS/URANS com-

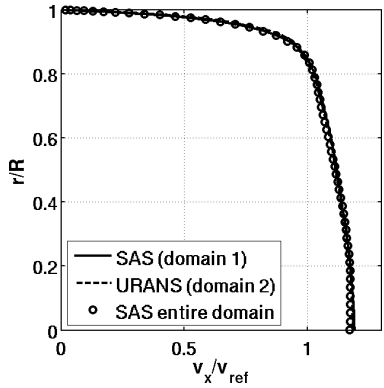


Figure 3.21: Time averaged radial profile of axial velocity on a section positioned in correspondence of the inlet of the second sub-domain.

putation along a section positioned in correspondence of the inlet of the second sub-domain, are compared with the velocity profile obtained with the simulation of the entire domain with the SAS approach. Profiles are reported in Figure 3.21. No evident discrepancies can be observed between the velocity profiles relative to SAS and RANS solutions of the coupled case. Moreover, the results of the coupled simulation agrees very well with the one of the entire domain simulated with the SAS approach, evidencing that the application of the coupling method does not affect the prediction of the flow field.

# Chapter 4

# Study of a realistic case of interaction between combustor and high-pressure turbine vanes

**Contents**



After having validated the methodology for the coupling of different CFD solvers, its application to a realistic test case of interaction between annular combustion chamber and high-pressure turbine vanes is proposed

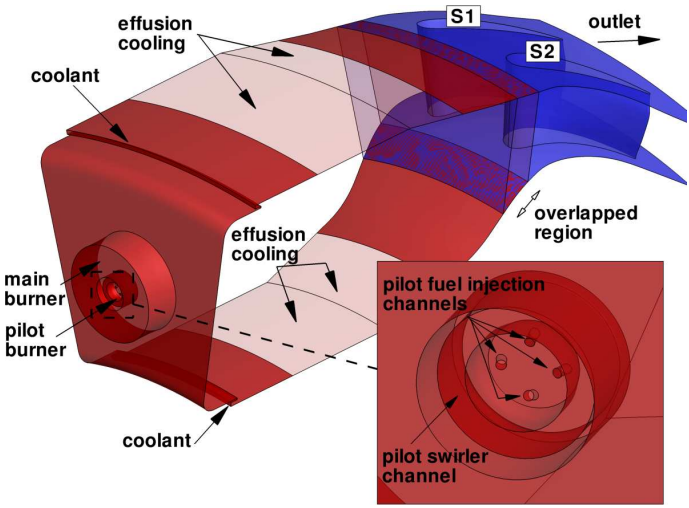


Figure 4.1: Computational domain.

in this Chapter. The annular combustor considered is a "virtual model" designed ad hoc for this activity, while the high pressure vanes considered are those of the well-known MT1 turbine stage used in the framework of the EU projects TATEF I and TATEF II [7, 21, 66]. Details about geometry and boundary conditions are reported in the following sections, after which the numerical results are presented.

## 4.1 Description of the test case

A schematic of the computational domain is reported in Figure 4.1. It is a periodic sector of 22.5° that includes a burner of the combustion chamber and two vanes, with an overlapped region which axial extension is 0.38 NGV axial chords. Detailed descriptions of the two sub-domains are given in the follow.

### 4.1.1 Annular combustor

As previously mentioned, the combustion chamber is a virtual model designed during the PhD activity and no experimental data are available. The decision to design and use such model has been dictated by the impossibility to access actual industrial geometries. It was therefore decided to reproduce a model representative of a modern lean-burn annular combustor making use of existing scientific literature. The combustion chamber presented here is an evolution of the one described in [67]. The main principle at the base of the design of the virtual model was to adequately reproduce aero-thermal characteristics on the interface between combustor and turbine. At the same time some constraints on geometry and operating conditions were imposed by the selected turbine. Concerning geometrical constraints, the shape of the endwalls of the vanes were to be respected. As it is possible to observe from Figure 4.1, the liner walls perfectly match the hub and casing surfaces of the turbine. The only fluid contained within the liner has been modeled, without considering any external casing in order to reduce computational costs.

The whole combustion chamber is equipped with 16 main burners, which corresponds to an equal number of pilot burners, arranged concentrically to the main ones with the function to provide an adequate flame stabilization. In this way the ratio between burners and vanes is $1 : 2$, it follows that the geometry is characterized by a periodicity of $22.5°$. A premixed stream of air and methane feed the main burner, from which enters the 90% of the total thermal input. The remaining 10% of the global thermal input is elaborated by a diffusion type pilot burner that supports each main burner. Methane is injected in the pilot burners through four cylindrical channels inclined in radial direction with respect to the burner axis. Air/fuel mixture in the main burner and air in the pilot one enter the combustion volume with tangential velocity components (co-rotating) with an angle of $40°$ with respect to the axis that provides swirl numbers of about 0.61 and 0.7 respectively for main and pilot burners. No swirler vanes are introduced in the computational model in order to reduce computational costs. For this reason, the swirl velocities have

| | $\dot{m}_{air}/\dot{m}_{air,tot}$ [%] | $\dot{m}_{fuel}/\dot{m}_{fuel,tot}$ [%] |
|---|---|---|
| main burner | 75 | 90 |
| pilot burner | 5 | 10 |
| outer slot cooling | 2.6 | |
| inner slot cooling | 1.8 | |
| outer effusion cooling | 9.5 | |
| inner effusion cooling | 6.1 | |

Table 4.1: Air and fuel repartitions in the combustion chamber.

been imposed by means of boundary conditions.

The combustor liner is cooled by means of two slots, adjacent to the dome, and through four effusion cooling platforms: two on the inner liner and two on the outer one. The cooling configuration is quite similar to the one studied by Andreini et al. [68]. Effusion cooling holes are not inserted in the model because of the excessive requirement in terms of grid resolution. The effusion platforms are treated by means of the adiabatic homogeneous model proposed by Mendez and Nicoud [69] to reproduce the effects of the effusion cooling on the main flow. Multiperforated platforms have been replaced by inlet sections, where the coolant mass flow rate is uniformly distributed with an inclination angle of $10^{\circ}$ with respect to the surface in order to reproduce the flow direction impressed by inclined effusion holes.

The mass flow repartition of air and fuel is reported in Table 4.1. A percentage of 20% of the total air is dedicated to the liner cooling, while the remaining air flow passes through the burners. The 4.4% of the air is used for slot cooling, while the 15.6% feeds the effusion cooling platforms. The equivalence ratio of the main burner is $\Phi = 0.63$, while the pilot burner works at stoichiometric conditions ($\Phi = 1$). The overall equivalence ratio $\Phi = 0.52$ is characteristic of lean-burn combustion systems. The operating pressure is $26bar$ and air enters the combustion volume at a stagnation temperature of $770K$, while fuel is provided at $300K$. The Reynolds number of the main burner, considering the channel height as reference, is about $4.17 \cdot 10^5$, while its Mach number is about 0.24.

### 4.1.2 MT1 high-pressure vane

The nozzle guide vane of the MT1 transonic research high-pressure stage [7, 21, 66] is inserted in the computational domain downstream to the combustion chamber. An image of the stage is reported in Figure 4.2. Such stage has been originally designed to operate with relatively low inlet

Figure 4.2: Instrumented MT1 stage [70].

total pressure ($4.6bar$) and total temperature ($444K$) thus, the coupling with the combustor described above leads to alter its dimensional working conditions. However, the matching between the operating conditions of combustor and vane is thought in order to maintain unaltered non-dimensional working parameters of the vane, as well as its geometry. In such a way the vane operates in similitude with respect to the original design point. In fact, when operative conditions of the combustor have been chosen, reduced mass-flow has been maintained unchanged, in first approximation, with respect to the design point $\dot{m}_{red} \simeq \dot{m}_{red,des}$ (see Dixon [71] for the definition) as well as Reynolds number $Re \simeq Re_{des}$, as

shown in the following equations:

$$\dot{m}_{red} = \frac{\dot{m}\sqrt{RT_{01}}}{D^2 p_{01}} \simeq \frac{\dot{m}_{des}\sqrt{R_{des}T_{01,des}}}{D_{des}^2 p_{01,des}} = \dot{m}_{red,des} \tag{4.1}$$

$$Re = \frac{\rho U D}{\mu} \simeq \frac{\rho_{des} U_{des} D_{des}}{\mu_{des}} = Re_{des} \tag{4.2}$$

where $p_{01}$ and $T_{01}$ are intended at the inlet section of the vane row and the subscript "*des*" is referred to the design point. At the design point, the Reynolds number of the NGV, based on its axial chord, is about $1.61 \cdot 10^6$, while the absolute Mach number at the NGV exit is 0.879. Further details on the MT1 stage can be found in [72, 73]. The geometry of the vane has not been modified ($D = D_{des}$), while all the other parameters change when the NGV works in conjunction with the combustion chamber. It is worth to underline that it must be also considered that the gas properties $R$ and $\mu$ change since air is elaborated at design point while the combustor exit flow is constituted by a mixture composed mainly by $N_2$, $CO_2$, $H_2O$ and $O_2$ with different thermo-chemical properties with respect to air.

## 4.2 Numerical approach

Simulations of the combustor/NGV interaction have been performed using a steady RANS approach with the loosely coupled methodology. For both the sub-domains, the same code ANSYS® Fluent has been used, but with different numerical approaches. Within the combustion chamber domain, the reactive turbulent flow is modeled using the SST turbulence closure and the partially premixed combustion model implemented in the solver. For the NGV sub-domain, the same turbulence closure is used while it is supposed that combustion is "frozen" at the exit of the combustor sub-domain. This assumption allows to avoid the need of resolving additional transport equations relative to combustion modeling. Such approximation will be discussed more in detail later in the text.

The computational domain used for the coupled simulations is reported in Figure 4.1. The exit section of the first sub-domain (combus-

tion chamber) is located on a plane positioned 0.25 NGV axial chords upstream of the leading edges plane while the inlet section of the second sub-domain (NGV) is located 0.6 NGV axial chords upstream of the leading edges plane. The computational domain terminates with the outlet section of the NGV domain, which is located in correspondence of the stator/rotor interface of the stage ($\simeq$ 0.21 axial chords downstream of the trailing edge).

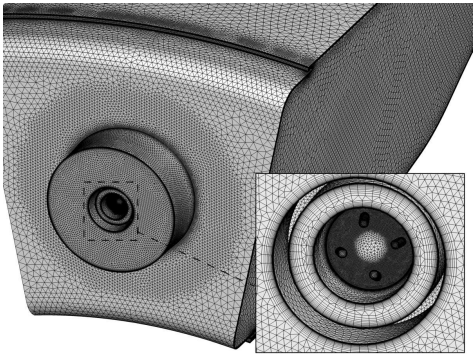

**(a)** combustion chamber

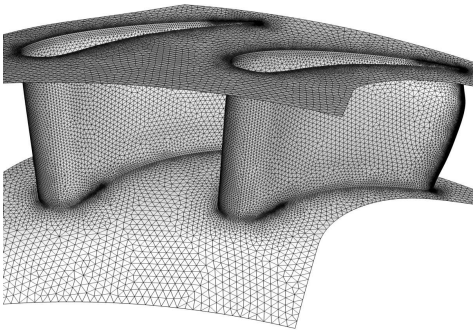

**(b)** nozzle guide vanes

Figure 4.3: Computational grids of combustion chamber and nozzle guide vanes.

Computational grids used for combustion chamber and NGV, both hybrid unstructured and generated with the commercial software Centaur$^{TM}$ are respectively reported in Figures 4.3(a) and 4.3(b). The mesh of the combustor is composed by about $5 \cdot 10^6$ elements while the NGV grid counts about $3.3 \cdot 10^6$ elements for the two vanes. Grid setting for this latter are derived from a previous work by Salvadori et al. [74], where a grid dependency study was performed.

The ability of ANSYS® Fluent in reproducing the isentropic Mach number distribution along the MT1 vane in its original working conditions ($p_{01} = 4.6bar$, $T_{01} = 444K$) has been evaluated comparing numerical results with the available experimental data at three spanwise positions. Results are reported in Figure 4.4 and are obtained with the SST $k-\omega$ turbulence model by Menter [50]. The isentropic Mach number distribution is in general good agreement with experimental data along the pressure side while, along the suction side, some discrepancies are

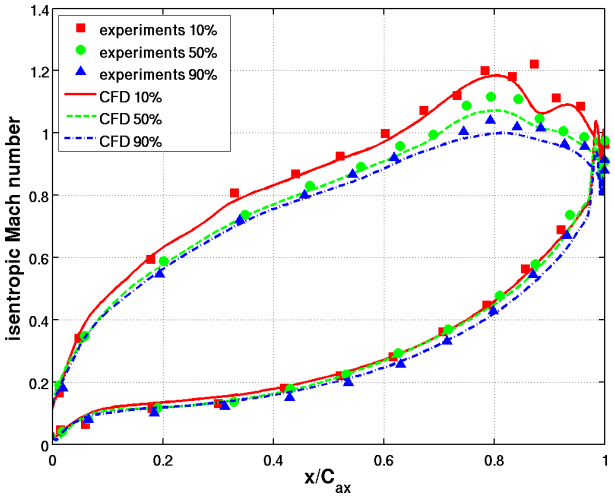


Figure 4.4: Isentropic Mach number distribution at three spanwise positions along the MT1 vane under uniform inlet conditions. Comparison between experimental data and numerical results.

present for $x/C_{ax} > 0.75$. In that zone, numerical results slightly underestimate flow acceleration at 50% and 90% of the spanwise position while at 90% of the vane height the peak of Mach number is not well reproduced by the CFD code. However, it is worth mentioning that, the actual geometry is characterized by fillets that connect the vane surface to hub and casing. Such geometric features are not reproduced in the computational model and this represents surely a source of uncertainty in comparing numerical results with experimental data.

### 4.2.1 Combustion modeling

The so-called "partially premixed" model [46] implemented in ANSYS® Fluent has been used to resolve the combustion process. It is based on the premixed and the non-premixed combustion models and allows to simulate combustion systems where the premixed and non-premixed type of combustion coexist. This is, in fact, the case of the analyzed combustor, where a air/fuel mixture enters the main burner and contemporaneously fuel is injected directly in the pilot burner.

The approach to non-premixed combustion modeling is based on the "mixture fraction" concept: a scalar variable which is conserved during the combustion process. It includes the concentration of all the species taking part to the reaction [75]. Through the use of the mixture fraction $f$, the thermo-chemical state of the flow is locally described by means of the following ratio:

$$f = \frac{Y_i - Y_{i,ox}}{Y_{i,fuel} - Y_{i,ox}} \tag{4.3}$$

where $Y_i$ is the mass fraction of the $i$-th element, $Y_{i,ox}$ the mass fraction of the element $i$ contained in the oxidizer, while $Y_{i,fuel}$ is the mass fraction of the element $i$ contained in the fuel. It follows that $f$ varies between 0 and 1, respectively for oxidizer and fuel. The possibility of "collapsing" all the chemical species in the mixture fraction depends from the assumption that all the species are characterized by the same diffusion coefficient. In this way, the mixture fraction definition is unique and it is possible

to substitute the transport equations for each specie to the transport equations for two scalar quantities. The first one is relative to the time-averaged mixture fraction itself ($\overline{f}$):

$$\frac{\partial}{\partial t}(\rho\overline{f}) + \nabla\cdot(\rho\overrightarrow{v}\overline{f}) = \nabla\cdot\left(\frac{\mu_t}{\sigma_t}\nabla\overline{f}\right) + S_m + S \tag{4.4}$$

and the second one relative to its time-averaged variance ($f' = f - \overline{f}$):

$$\begin{aligned}\frac{\partial}{\partial t}(\rho\overline{f'^2}) + \nabla\cdot(\rho\overrightarrow{v}\overline{f'^2}) = \\ = \nabla\cdot\left(\frac{\mu_t}{\sigma_t}\nabla\overline{f'^2}\right) C_g\mu_t(\nabla\overline{f})^2 - C_d\rho\frac{\epsilon}{k}\overline{f'^2} + S\end{aligned} \tag{4.5}$$

where $\sigma_t$, $C_g$ and $C_d$ are constants, $S_m$ takes into account mass transfer between liquid and gaseous phase in case of liquid fuels, while $S$ indicates source terms eventually defined (in our case both $S_m$ and $S$ are null). In order to describe the interaction between chemistry and turbulence the approach based on "assumed-shape probability density function" $p(f)$ has been used. It can be imagined as representative of the time fraction in which fluid is in the state determined in the neighborhood of a given value of $f$. Figure 4.5 summarizes this concept: on the right the fluctuating behavior of the mixture fraction is shown while the corresponding probability density function is shown on the left. The concept can be

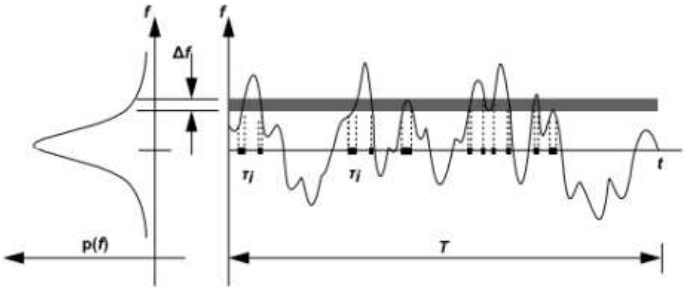


Figure 4.5: Schematic of the probability density function from [46].

expressed mathematically as follows:

$$p(f)\triangle f = \lim_{T\to\infty} \frac{1}{T} \sum_i \tau_i \tag{4.6}$$

where $\tau_i$ is the fraction of time where $f$ assumes the value determined from the neighborhood $\triangle f$. The shape of the probability density function depends from the nature of the turbulent fluctuations, which are not known a priori. For this reason it is assumed before the calculation and in our case a $\beta$-function probability density function has been assumed. Simulations have been performed using an extension of the non-premixed model for non-adiabatic systems. In this way it is no more sufficient the only mixture fraction to describe the local thermo-chemical state but the enthalpy variable must be introduced in order to describe energy exchanges. Chemistry is treated by means of the "diffusion laminar flamelet" concept. It is based on the concept of imagine the turbulent flame as an ensemble of diffusion laminar flamelets embedded within the turbulent flow field. Through the use of a detailed chemical kinetic mechanism it is possible to resolve, upstream of the CFD simulation, a multitude of flaminar flames where fuel and oxidizer are injected in opposition. Subsequently the generated flamelets must be "embedded" in the turbulent flame by means of the approach based on the probability density function described previously. In this way chemistry, which is preprocessed and tabulated, is managed through a group of look-up tables that are consulted during the resolution of the flow, without the need of a time-consuming resolution of chemistry for each iteration. It is then possible to take into account for complex chemical mechanisms ensuring an accurate reproduction of the chemical processes. The chemical kinetic mechanism used to describe methane combustion is a reduced mechanism developed by Correa [76] that considers 16 chemical species and 41 reactions. However the approach based on laminar flamelets is limited to the assumption that chemistry is infinitely fast with respect to characteristic aerodynamic phenomena, therefore it is not applicable for the prediction of relatively slow chemical phenomena like for example $NO_x$ formation.

The flamelet regime can be individuated through the Damköhler number $Da$, defined as the ratio between the characteristic time relative to integral scale turbulence and the characteristic time of chemistry based on laminar flame thickness and laminar flame speed. The hypothesis of "fast chemistry" will be satisfied when $Da \gg 1$. Further details on the non-premixed combustion model and on flamelet generation are reported in [46, 75].

What described up to here is relative to the non-premixed modality of fuel injection and to its relative development of the combustion process. On the other side it is necessary to treat the premixed combustion process taking place downstream to the main burner of Figure 4.1. It has been treated by means of the so-called "c-equation" model. It is based on a scalar reactive quantity called "progress variable" that defines the advancement of the reactive process being defined zero in the unburnt mixture and unity in the burnt products. In terms of temperature it is defined by:

$$c = \frac{T - T_{burnt}}{T_{unburnt} - T_{unburnt}} \tag{4.7}$$

The flame front propagation is solved by means of a transport equation for the mean progress variable $\overline{c}$:

$$\frac{\partial}{\partial t}(\rho\overline{c}) + \nabla \cdot (\rho \overrightarrow{v}\overline{c}) = \nabla \cdot \left(\frac{\mu_t}{Sc_t}\nabla\overline{c}\right) + \rho S_c \tag{4.8}$$

where $Sc_t$ is the turbulent Schmidt number and $S_c$ is the reaction progress source terms. This latter term, the mean reaction rate, is modeled in the following way:

$$\rho S_c = \rho_u U_t \left|\nabla\overline{c}\right| \tag{4.9}$$

having defined $\rho_u$ and $U_t$ respectively how the unburnt density and the turbulent flame speed. The right evaluation of the turbulent flame speed is the key of the premixed combustion model. This local parameter has been evaluated by means of the Zimont closure [77], which uses the local

turbulence intensity and length scale to derive the turbulent flame speed from the laminar one.

To summarize, the following equations are resolved in the combustor domain: continuity, momentum (three components), energy, mixture fraction, mixture fraction variance, progress variable, turbulent kinetic energy and specific dissipation of this latter.

### 4.2.2 Hypothesis of uniform chemical species distribution within the turbine domain

As mentioned before, going downstream to the combustor domain, the combustion process is assumed to be frozen. In this way it is not necessary to use combustion models within the turbine domain, reducing computational costs. It is straightforward that this assumption is much more realistic then the chemical reactions are close to the completion. Although some chemical reactions, like for example the ones relative to $NO_x$ formation, are relatively slow, it is reasonable to assume that most of the chemical reactions that determine the heat release are completed before that flow enters the turbine. Moreover, even if it is decided to resolve combustion process within the turbine domain it should be considered that an appropriate combustion model should be chosen. In fact, as described previously, the combustion model used is based on the assumption that the chemical processes are infinitely faster than turbulent phenomena. Such assumption may no longer be valid for the high-speed flow that is established in the turbine, affecting the model accuracy.

Not only the combustion process is frozen downstream to the combustor domain, but another approximation is done concerning the distribution of the combustion products. The concentration of these latter is not uniformly distributed on the combustor/turbine interface and local gradients are present, especially near the endwalls, where only the cooling air is present. For this reason, in order to accurately describe the transport of chemical species, it should be necessary to use a single transport equation for each specie. Considering only the most important species ($CO_2$, $H_2O$, $O_2$ and $N_2$), four additional equations should

be resolved in the turbine domain, even if combustion is not considered. This is obviously time-consuming and the following simplification is done. Once a preliminary computation of the reactive flow in the combustor is obtained without considering the turbine, the mass-weighted average thermo-chemical properties are calculated on the plane corresponding to the inlet section of the turbine domain. Such average values are used to define the properties of the ideal gas that is used in the turbine domain to reproduce the combustion products. In this way, using such "equivalent" ideal gas, it is intrinsically assumed that combustion products are uniformly distributed within the turbine domain. An attempt to quantify the error introduced by this approximation is reported in Appendix A.

### 4.2.3 Coupling process

To initialize the coupled simulations, a preliminary simulation of the only combustion chamber has been performed with a uniform static pressure map imposed on its outlet section, without considering the influence of the downstream vanes. Once obtained the converged solution, the distributions of total pressure, components of the velocity unit vector, total temperature, turbulent kinetic energy and turbulence specific dissipation rate have been extracted on a plane corresponding to the inlet section of the NGV domain. Such distributions have been used as inlet boundary conditions for the computation of the only NGV domain. In this latter, a static pressure map corresponding to the time-averaged result obtained from an unsteady RANS computation of the entire MT1 stage, operating at the design point, performed by Salvadori et al. [74], has been used as outlet boundary condition. Obviously, since the working conditions simulated with the upstream combustor are different with respect to the MT1 design point (reported above), such pressure distribution has been rescaled in order to obtain the mean exit value required by the actual operating conditions.

After resolving the two separated domains in these two preliminary steps, the iterative coupling process has been started. Convergence has been obtained after 15 coupling cycles composed by 500 numerical it-

erations for each solver. Two runs have been performed with different thermal conditions imposed along the walls: adiabatic and isothermal. The first has been used to derive the adiabatic wall temperature distribution while the second one permitted to calculate wall heat flux.

## 4.3 Characterization of the aero-thermal field at the exit section of the combustion chamber

As mentioned before, no experimental data are available for the considered combustion chamber. Therefore, the first step was to evaluate the coherence of the aero-thermal field at the exit with data available in the scientific literature relatively to modern low-emission gas turbine annular combustion chambers or hot streaks generators dedicated to their reproduction.

A map of non-dimensional total temperature (non-dimensionalized with respect the mass-weighted average), with superimposed velocity vectors, extracted on a plane corresponding to the inlet section of the NGV domain, is shown in Figure 4.6. It has been obtained from a steady RANS simulation of the combustor domain only, with uniform static pressure imposed on the outlet section. The plane is located 0.6 NGV axial chords upstream of the leading edge plane and the image is a view looking upstream from the turbine. As it is possible to observe, the hot fluid is confined in the central region of the height of the channel, while, coolant injected within the combustion chamber generates cold streaks along the endwalls. It is also evident that swirl, imposed by the burners, is conserved up to the analyzed plane. Differently from what expected, the swirl center is not positioned centrally with respect to the burner position (central with respect to Figure 4.6), but it is moved tangentially. Such lateral migration has been observed also in [67] and can be attributed to the shape of the end-walls; the internal end-wall in fact is more curved than the external one. This implies that the meanline of the channel, moving from combustor to turbine, is characterized by an increase of radius. Vorticity originated by the swirler is initially oriented

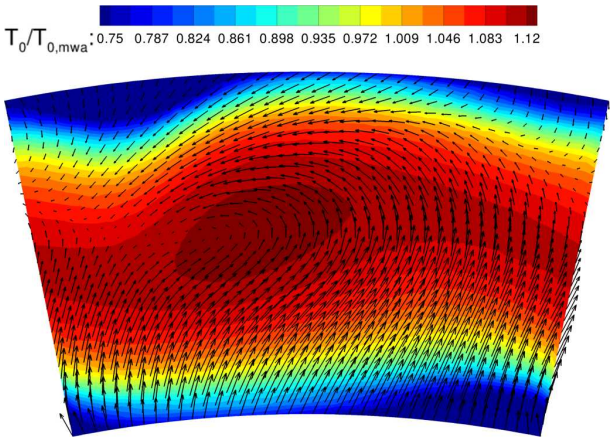


Figure 4.6: Aero-thermal field on the combustor/turbine interface.

as the axis of the machine but, since the mean radius increases towards the vanes, the vortex tube is forced to deflect radially. As a consequence of this deflection the vortex core tends to moves laterally. From a mathematical point of view, the vorticity equation should be considered; for a steady incompressible flow of a Newtonian fluid in absence of body forces it can be expressed as follows:

$$\left(\vec{V}\cdot\vec{\nabla}\right)\vec{\omega} = \frac{\mu}{\rho}\nabla^2\vec{\omega} + \left(\vec{\omega}\cdot\vec{\nabla}\right)\vec{V} \tag{4.10}$$

The therm on the left-hand side of equation 4.10 represents the inviscid transport of vorticity. The first term on the right-hand side represents diffusion of an existent vorticity due to viscosity while the second term is responsible for reorientation or stretching of vortex filaments [78]. This latter term, present also for inviscid flows, is the reason why the vortex core migrates tangentially. In case the end-walls were parallel planes, swirl is not subjected to changes of direction and remains aligned with the swirler from which it was generated. This behavior is evident in the work by Giller and Schiffer [27], where a linear cascade with straight end-walls is analyzed. On the contrary, a tangential migration could

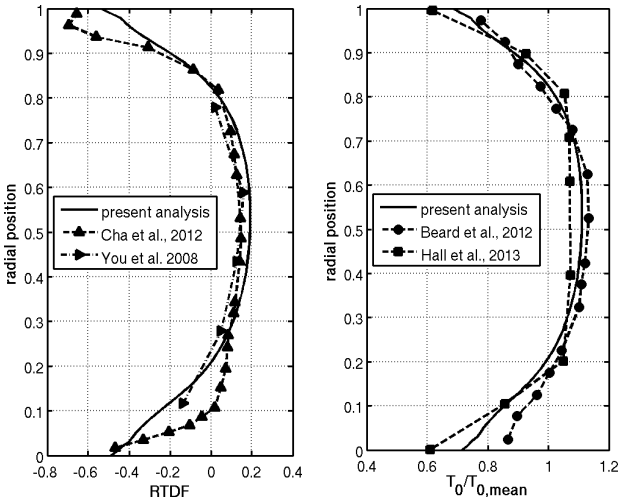


**(a)** RTDF **(b)** non-dimensional total temperature

Figure 4.7: Comparison of RTDF and tangentially averaged non-dimensional total temperature with respect to available data from scientific literature.

be noticed in the work by Hall et al. [32], where the analyzed combustor simulator test rig is characterized by a shape of the end-walls very similar to the test case considered in this thesis.

On the considered combustor/turbine interface, the combustor model reproduces fairly well the radial distributions of non-dimensional temperature of other test cases available in literature, as shown in Figure 4.7. Non-uniformities are reported in terms of local Radial Temperature Distortion Factor ($RTDF$) and non-dimensional total temperature. Profiles, obtained from the simulation of the only combustor domain, are compared with the ones available from the works by Cha et al. [6], You et al. [79], Beard et al. [80] and Hall et al. [32]. The local $RTDF(r)$ is defined by:

$$RTDF(r) = \frac{T_{0;t.a.} - T_{0;mean}}{\Delta T_{0;cc}} \tag{4.11}$$

where $T_{0;t.a.}$ is the tangentially-averaged total temperature and $T_{0;mean}$ is the mean total temperature; $\Delta T_{0;cc}$ is the total temperature rise between $T_{0;mean}$ and temperature of air entering the combustion chamber itself. Concerning the references from literature, the works by Cha et al. [6] and You et al. [79], reported in Figure 4.7(a), both concerns real combustion chambers for aero engines. The first one analyzes a RQL combustion chamber experimented in similitude conditions, without reacting flow. The second one is relative to the combustion chamber of the Pratt & Whitney 6000 engine. The works by Beard et al. [80] and Hall et al. [32] of Figure 4.7(b) are instead both referred to hot streak generators, experimented at the Oxford Turbine Research Facility (OTRF), working in conditions of non-reacting flow. All the literature references differ between them, especially in the regions close to the endwalls. However, the temperature profile of the present analysis (solid line in Figure 4.7) is a compromise both in terms of maximum temperature peak in the central region of the span and near the endwalls. It was therefor judged that the virtual combustor model was adequate to reproduce a realistic thermal field at the entry section of the high-pressure turbine. The aerodynamic field obtained from the steady RANS computation of the combustor only, on the plane positioned 0.6 NGV axial chords upstream of the leading edge plane, has been also compared in Figure 4.8 in terms of yaw angle with data available in the work by Qureshi et al. [24]. Such reference data are relative to target distributions, at 20% and 80% of the height of the channel, that had to be matched by the authors through an apposite swirl generator. As visible from Figure 4.8, the yaw angle distributions of the present analysis are less aggressive with respect to the ones of Qureshi et al. [24], especially in terms of maximum and minimum peaks.

Turbulence intensity and turbulence length scale, obtained on the combustor/turbine interface, are shown in Figure 4.9. These values, even if obtained with a RANS simulation, are indicative of the tubulence quantities on the inlet section of the turbine. A streak with high turbulence intensity ($\simeq$ 30%) appears in the central part of the channel, with an inclined shape caused by swirl. Such high value of $Tu$ is in line with

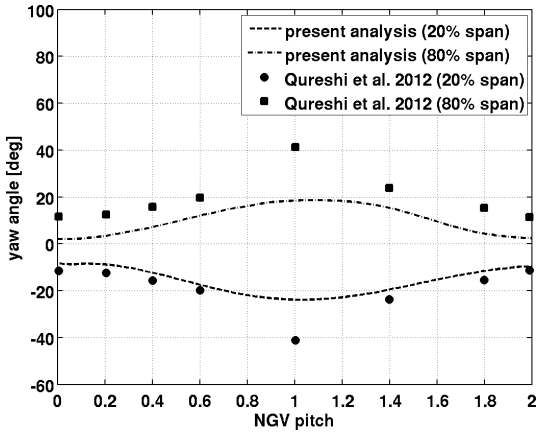


Figure 4.8: Comparison of yaw angle distributions at 20% and 80% of the channel height; reference data are extracted from the work by Qureshi et al. [24].

what emerged from Chapter 1.

The length scale, calculated as the local ratio $\sqrt{k}/\omega$ and normalized with respect to the channel height, is shown in Figure 4.9(b). The maximum peak found is about 5% of the height of the channel. This value is lower with respect to the findings of Chapter 1 but it must be considered that no turbulence scales are resolved with a RANS simulation.

## 4.4 Results

Figure 4.10 reports the isentropic Mach number distributions at three vane heights, for the two vanes; results of the coupled simulations are compared with the ones relative to the simulation of the only NGV domain considering uniform inlet flow. As expected, S1 and S2 vanes work under different aerodynamic conditions with respect to the uniform inlet case. In particular, an increment of the aerodynamic load can be observed at 10%, especially for the S2 vane. At midspan no noticeable differences are present neither between S1 an S2 nor with respect to the uniform inlet

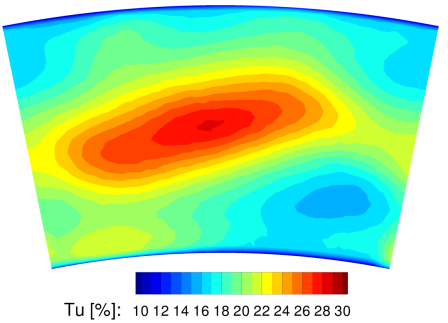


**(a)** turbulence intensity

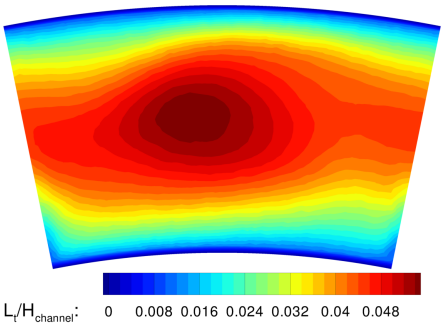


**(b)** normalized turbulence length scale

Figure 4.9: Distributions of turbulence intensity and turbulent length scale on the combustor/turbine interface plane.

case. Near casing, at 90% of the height, both the vanes have a reduced aerodynamic load with respect to the uniform case and the difference is more marked on the S2 vane. All these variations are due to changes of the flow incidence with respect to the uniform case, induced by the incoming swirl. At 10% the incidence is slightly increased, while at 90% is reduced, coherently with the swirl motion imposed in the combustor, which generates a positive axial vorticity component with respect to the burner machine axis. The cause of the more pronounced aerodynamic variations evidenced on the S2 vane can be ascribed to the previously

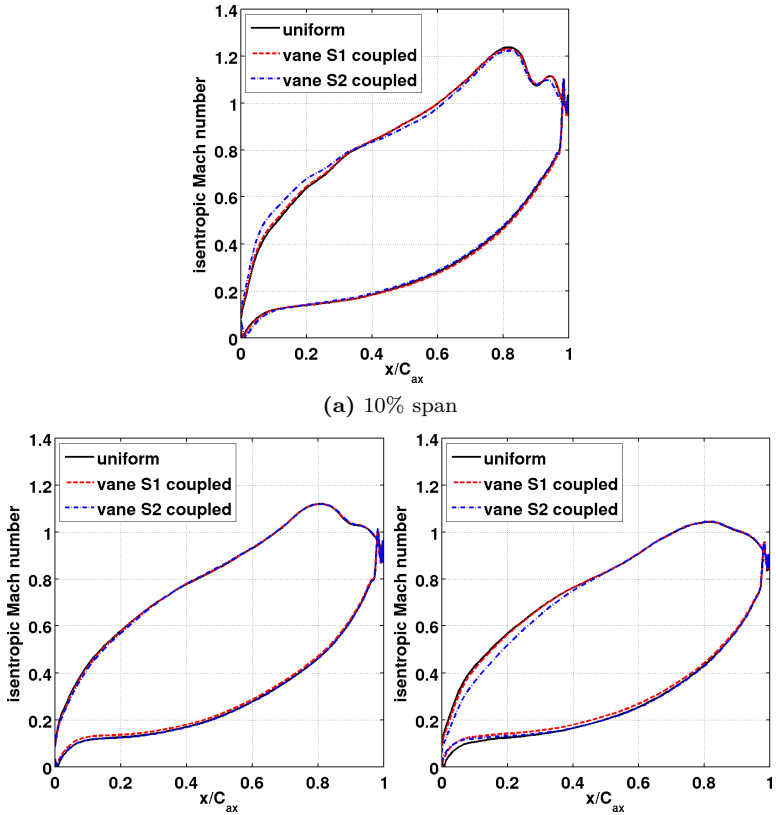


**(a)** 10% span

**(b)** 50% span

**(c)** 90% span

Figure 4.10: Comparison between the isentropic Mach number distributions on the NGV obtained with coupled simulation and uniform inflow.

mentioned lateral swirl migration taking place passing from combustion chamber to turbine. In fact, despite of the burner is centered with respect to the vane passage, swirl tends to move laterally with respect to the original direction and arrives at the inlet section of the turbine close to the S2 vane. Due to the aero-thermal distortions entering the turbine,

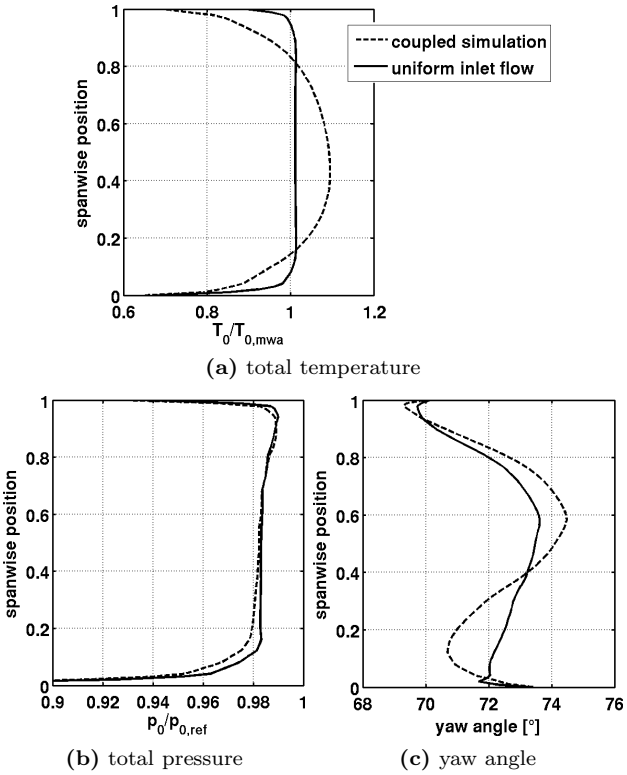


**(a)** total temperature

**(b)** total pressure

**(c)** yaw angle

Figure 4.11: Tangentially-averaged quantities measure on the outlet section of the NGV domain (corresponding to the stator/rotor interface).

the characteristic of the flow downstream of the NGV row are modified with respect to a case considering uniform inlet flow. Such variations are particularly critical for the downstream rotor and a measure of how they impact on the operation of the rotor can be deduced observing the tangentially-averaged quantities measured on the NGV outlet section reported in Figure 4.11. As stated before, that section has been defined in correspondence of the stator/rotor interface of the stage. All the quan-

tities reported in Figure 4.11 are mass-weighted averages. From Figure 4.11(a), showing the spanwise distribution of the total temperature, the effect of the hot spot is clearly visible. In fact, compared with the uniform case, the coupled one is characterized by an increased total temperature peak located slightly below midspan while lower total temperature is present near the endwalls. Such temperature reductions are due to the cold streaks established by the action of the cooling system present in the combustion chamber.

As demonstrated previously in Figure 4.10, residual swirl and total pressure non-uniformities, exiting from the combustor, considerably alter aerodynamics of the vanes and consequently its losses. This is visible in Figure 4.11(b), where the spanwise distribution of total pressure is shown. This latter is normalized with respect to the average total pressure measure in the combustor, on a plane corresponding to the inlet section of the NGV domain. The increased losses due to flow distortions present in the coupled cases are particularly evident in the lower part of the span. Such increased losses can be ascribed to the interaction between residual swirl and secondary flows developing inside the vane passages. Figure 4.11(c), that reports the radial distribution of the exit yaw angle, supports this hypothesis. In fact, a considerable under-turning is present in the lower part of the span, where swirl and passage vortex are discordant. The opposite happens in the upper middle part of the span, where an overturning can be observed for the coupled case.

Variations of the tangentially-averaged quantities shown in Figure 4.11 are absolutely non-negligible considering both the NGV and the operation of the components downstream of it. Therefore, these results underline the importance of taking into account the real working conditions of components.

Although the aerodynamic variations induced by distortions coming from the combustion chamber are relevant, the behavior of the NGV is also modified from a thermal point of view. Adiabatic wall temperature and heat transfer coefficient are analyzed in the follow. Distributions of non-dimensional adiabatic wall temperature along the vanes are reported

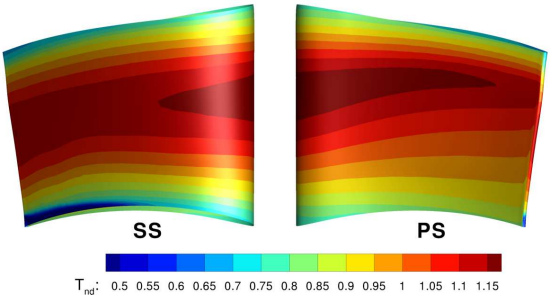


**(a)** S1

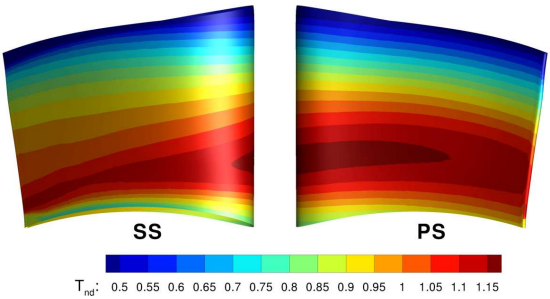


**(b)** S2

Figure 4.12: Distributions of non-dimensional adiabatic wall temperature on S1 and S2 vanes.

in Figure 4.12. The hot streak migration causes a non-uniform distribution along the surfaces of the vanes and, similarly to what observed before concerning aerodynamic load, the two vanes are subjected to very different conditions. Differently from the aerodynamic load, in this case the most critical conditions are relative to the S1 vane, where the high-temperature region is more extended with respect to the S2 vane, both in streamwise and in spanwise directions. Moreover, the characteristic shape of the hot streak, distorted by swirl, leads to a different positioning of such high-temperature zones. In fact the hot streak impacts on the S1 vane in the upper part of span, vice versa, for the S2 vane, it goes to affect the lower part of the span, leaving a marked cold streak near

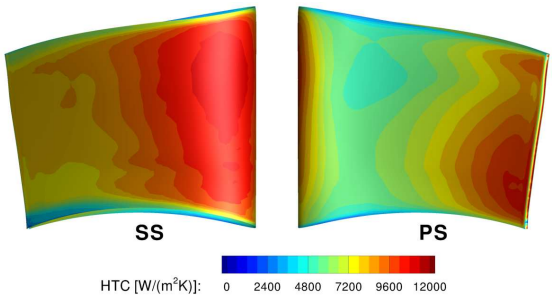


**(a)** S1

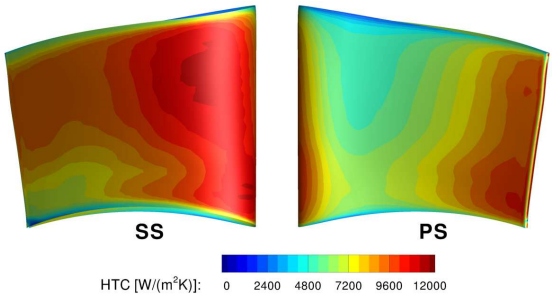


**(b)** S2

Figure 4.13: Distributions of heat transfer coefficient on S1 and S2 vanes.

casing.

Distributions of heat transfer coefficient are ported in Figure 4.13; it is calculated according to the following definition:

$$HTC = \frac{\dot{q}}{T_{aw} - T_w} \tag{4.12}$$

where $\dot{q}$ is the local wall heat flux, obtained through a simulation with an imposed uniform wall temperature ($T_w$) and $T_{aw}$ is the adiabatic wall temperature distribution shown in Figure 4.12. Although some differences are present, distributions of heat transfer coefficient are characterized by less marked vane-to-vane differences with respect to what previously

observed in terms of adiabatic wall temperature. The maximum peak is located on the suction side of the S2 vane, in the upper part of the span, where, the heat transfer coefficient remains higher with respect to the S1 vane also downstream. On the contrary, looking at the pressure side, a more extended spot with $HTC$ is present on the S1 vane. The non-uniform distribution of heat transfer coefficient along the vane surfaces is due to, obviously the flow acceleration inside the passages and, in addition, to the non-uniformly distributed turbulence intensity of the incoming flow (Figure 4.9(a)). Close to the endwalls, the effect of secondary flows in determining the spanwise gradients of $HTC$ are visible, especially along the suction side of the vanes.

Comparing the results of the coupled simulations (adiabatic and isothermal cases) with the analogous obtained using a uniform inlet flow with the same average parameters of coupled one, it has been possible to calculate local differences of adiabatic wall temperature ($\Delta T_{aw}$) and heat transfer coefficient ($\Delta HTC$) along the surfaces. $\Delta T_{aw}$ and $\Delta HTC$ are defined as:

$$\Delta T_{aw} = \frac{T_{aw;coupled} - T_{aw;uniform}}{T_{aw;uniform}} \tag{4.13}$$

$$\Delta HTC = \frac{HTC_{coupled} - HTC_{uniform}}{HTC_{uniform}} \tag{4.14}$$

Such differences are reported in percentage terms respectively in Figures 4.14 and 4.15. These maps report locally the percentage error that would be committed relying on a simulation that does not take into account any inlet distortion. As for the adiabatic wall temperature distribution, also the qualitative behavior of $\Delta T_{aw}$ is characterized mainly by spanwise gradients, being the inlet total temperature of the reference simulation uniform. $\Delta T_{aw}$ ranges from $-30\%$ up to $+10\%$. The negative peaks are located close to the endwalls, where the reference simulation does not take into account the cold streaks generated by the cooling system of the combustor. The maximum peak instead is located in the upper middle part of the S1 vane and is more extended axially along the suction

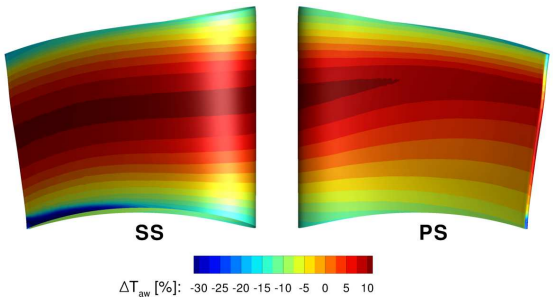


**(a)** S1

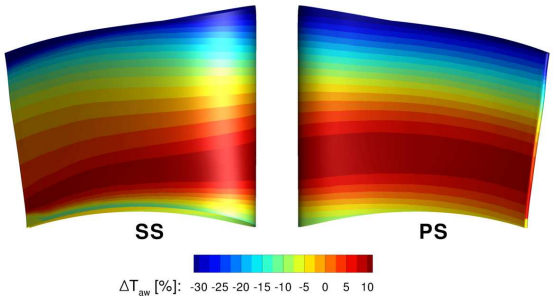


**(b)** S2

Figure 4.14: Distributions on S1 and S2 vanes of the difference between adiabatic wall temperature of the coupled simulation with respect to the case with uniform inflow.

side. Even if the present simulations do not consider the turbine cooling system, it is possible to draw some considerations concerning this latter. Relying the cooling system design on simulations that do not consider any inlet temperature distortion, two problems can emerge. The first one is related to the overestimation of the main flow temperature close to the endwalls, that could drive the designer to overestimate the amount of cooling air needed to protect such zones. The second problem is opposite and is related to the underestimation of the main flow temperature in the zone interested by the hot streak. In those regions the designer, based on the estimation done considering uniform inflow, could

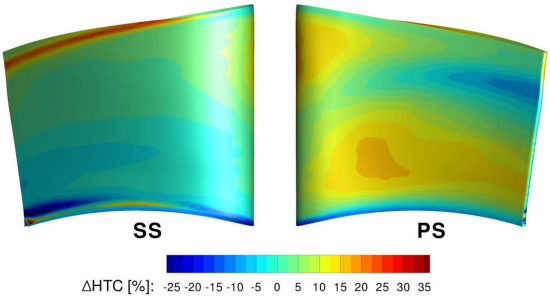


**(a)** S1

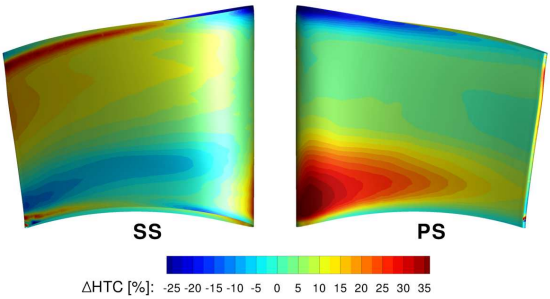


**(b)** S2

Figure 4.15: Distributions on S1 and S2 vanes of the difference between heat transfer coefficient of the coupled simulation with respect to the case with uniform inflow.

be inclined to save cooling air, with potential deleterious effects on the component reliability. Obviously, the actual metal temperature of the vanes depends, apart from the efficacy of the cooling system, not only by the adiabatic wall temperature but also from the heat transfer coefficient. The same evaluations proposed above in terms of $\Delta T_{aw}$ can be done in terms of $\Delta HTC$ (Figure 4.15). Percentage variation of the heat transfer coefficient, with respect to the reference case, is wider with respect to $\Delta T_{aw}$, ranging from $-25\%$ to $+35\%$. The maximum peak is located on the S2 vane (where the most pronounced incidence variations have been observed; see Figure 4.10) along the pressure side, in the lower part of

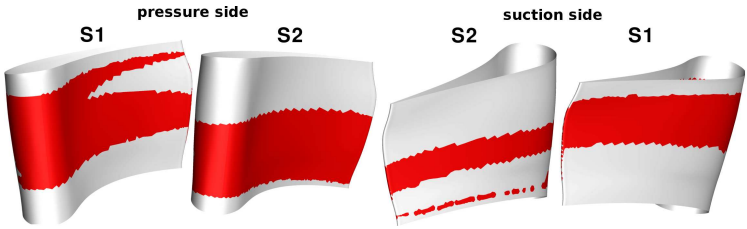


Figure 4.16: Zones (depicted in red) where both adiabatic wall temperature and heat transfer coefficient are underestimated using uniform inlet boundary conditions.

the span. Both Figures 4.15(a) and 4.15(b) evidence large percentage variations in the estimation of the heat transfer coefficient close to the endwalls. This is a clear sign that secondary flows, characterizing these zones, are modified by the incoming aerodynamic distortions.

Combining the information given by data shown in Figures 4.14 and 4.15, it is possible to evaluate zones where, the consideration of a uniform inlet flow would lead to an underestimation of both adiabatic wall temperature and heat transfer coefficient. Such zones are individuated by the following simple criterion:

$$min(\Delta T_{aw}, \Delta HTC) > 0 \tag{4.15}$$

The colored parts of the vanes shown in Figure 4.16 indicates where the criterion is satisfied. In this way, critical zones associated to not consider inlet aero-thermal flow distortions are highlighted. The "critical" zones cover large portions of pressure and suction side of both the vanes. The fact that both $\Delta T_{aw}$ and $\Delta HTC$ are greater than zero does not imply necessarily that metal temperature will be higher than in other zones but, however, it provides a measure of how uniform inlet conditions can be ineffective in simulating the actual behavior of components. However, any consideration on metal temperature and component life can not be separated by an evaluation of the temperature field inside the metal parts itself, for example by means of conjugate heat transfer simulations.

# Part II

# Effects of combustor non-uniformities on cooled high-pressure vanes

# Chapter 5

# Study of the effects of combustor non-uniformities on a film-cooled high-pressure vane

**Contents**



In the previous Chapter, the importance of considering the actual working conditions at which components are subjected to, has been highlighted analyzing an annular combustor and a high-pressure vane, this

latter without considering cooling system. Results have demonstrated strong aerodynamic variations with respect to a reference case with uniform inlet boundary conditions, suggesting important modifications of the operation of cooling systems, where present. In the present Chapter, a film-cooled high pressure vane subjected to inlet temperature distortions and residual swirl is considered. Performance of the cooling system and metal temperature distributions are evaluated by means of conjugate heat transfer (CHT) simulations.

## 5.1 Description of the test case

The test case used for numerical activity is a heavily film cooled vane which detailed description is available in the research papers of Jonsson and Ott [81] and Charbonnier et al. [82]. It is a transonic research vane, experimentally investigated with uniform inflow conditions in a linear cascade at the Ecole Polythecnique Fédérale de Lausanne during the EU-funded TATEF2 project. The exit Reynolds number based on chord length is $1.46 \cdot 10^6$ while the nominal value of isentropic Mach number at the outlet section is 0.88. The cooling system, shown in Figure 5.1,

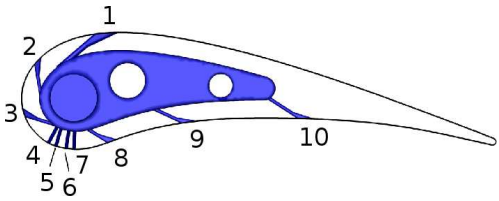


Figure 5.1: Schematic of the cooling system.

consists of three rows of fan-shaped holes on both pressure and suction side while 4 rows of cylindrical holes inclined by 45° downward protect the leading edge of the vane (showerhead). The streamwise injection angle of the fan-shaped holes is different row by row and ranges from 31° of row 10 to 53.3° of row 3 with respect to the local surface tangential direction. The diffuser shape opens 12° symmetrically in both lateral directions

| | main | coolant |
|---|---|---|
| working fluid | air | $CO_2$ |
| inlet total pressure $[bar]$ | 1.535 | 1.780 |
| inlet total temperature $[K]$ | 333 | 303 |
| inlet turbulence intensity [%] | 10 | |
| inlet turbulence length scale $[m]$ | 0.013 | |
| exit static pressure $[bar]$ | 0.927 | |

Table 5.1: Working conditions of the experimental case.

together with a laid-back angle of 15°. Two computational domains have been considered for the numerical campaign. The first one, referred as experimental geometry, has been used for grid sensitivity analysis and validation while the second one, referred as realistic geometry (or engine-like geometry), has been used for the evaluation of the thermal effects with realistic inlet conditions. The computational domain used for grid sensitivity analysis and turbulence model assessment is shown in Figure 5.2(a) and reproduces the experimental configuration of Jonsson and Ott [81] reported in Figure 5.2(b). It includes the whole fluid region with plenum and cooling channels but no solid parts. Inlet and outlet sections are placed respectively about $0.65C_{ax}$ upstream of the leading edge and about $0.6C_{ax}$ downstream of the trailing edge. The coolant inlet is on the top of the plenum.

For the experimental configuration, $CO_2$ is used as coolant in order to match coolant-to-main-flow density ratio ($DR = 1.6$) of an engine-like condition. The nominal blowing ratio ($BR$) of the showerhead cooling system is about 2.8, while varies from 1 to 1.5 moving from row 1 to row 3 and from 3.4 to 1.5 moving from row 8 to row 10. The other working conditions are reported in Table 5.1. Since no information were present concerning turbulence quantities for the cooling flow, a turbulence level of 5% and a length scale of $0.0004m$ have been imposed in the simulations.

In order to study the effects of realistic inlet conditions, the computational domain has been modified to be representative of a real machine configuration. The novel geometry, shown in Figure 5.2(c), has identical cooling system but is composed of two vanes and has a reduced aspect

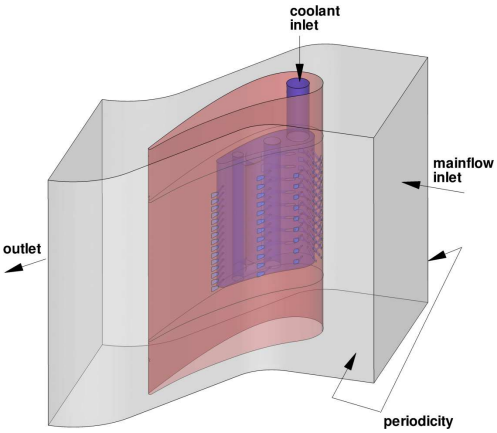


**(a)** domain of the experimental configuration

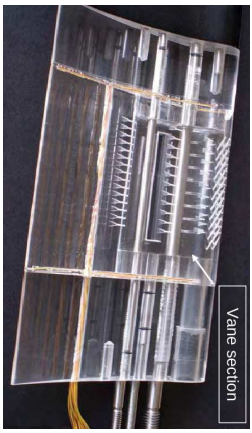


**(b)** experimental test article

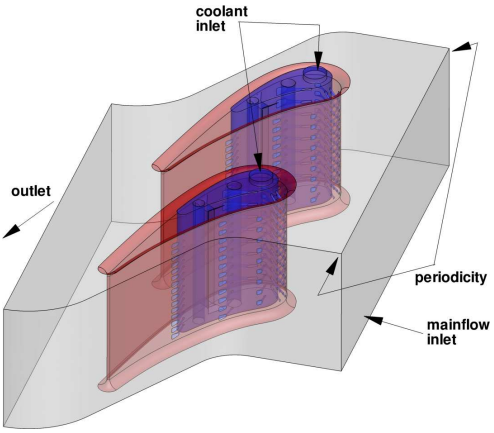


**(c)** domain of the engine-like configuration

Figure 5.2: Geometrical configurations tested.

ratio in order to match the realistic inlet profile periodicity and characteristic dimensions ratio. The model includes the whole fluid region (both plenums and cooling channels) and also solid regions in order to allow CHT simulations for the estimation of its thermal field.

### 5.1.1 Simulation matrix

All the simulations performed are summarized in Table 5.2. Simulations are subdived in three main groups. The first one is dedicated to the model assessment and includes grid sensitivity analysis and comparisons of numerical results with the experimental data in terms of adiabatic effectiveness $\eta_{aw}$, wall heat flux $\dot{q}$ and isentropic Mach number along the vane. This latter is evaluated on the same vane geometry but without cooling system.

The second group of simulations is dedicated to the study of the effects of swirl on the adiabatic film cooling effectiveness. A simulation with uniform inlet flow is used as reference for the comparison with two simulations where an aggressive swirl is imposed on the inlet section, considering two different alignments with respect to the vanes. The two configurations tested are relative to the swirl core aligned once with the vane passage and once with the leading edge.

The third group of simulations concerns the study of the combined effect of an inlet swirl with a superimposed hot spot. Also here, a simulation with uniform inlet flow is taken as a reference and is compared with two simulations where hot spot and swirl are clocked in the same positions used in the second group of simulations.

Adiabatic effectiveness has been evaluated via adiabatic condition imposed along the walls while an isothermal condition of $323K$ has been imposed according to Charbonnier et al. [82] for analyzing the heat flux. For the last group of simulations, since conjugate heat transfer is used, the thermal boundary condition present along the solid surfaces is determined by the coupled resolution of the thermal field of solid and fluid.

The non-uniform inlet boundary conditions used in the second and third groups of simulations are described in the following section.

### 5.1.2 Non-uniform inlet boundary conditions

The hot spot and swirl profiles used derives from the experimental campaign of the EU-funded TATEF2 project and are respectively de-

| | **domain** | **n° of vanes** | **thermal b.c.** | **hot spot** | **swirl** |
|---|---|---|---|---|---|
| grid sensitivity (uniform inlet flow) | experimental | 1 | $323K$ | no | no |
| evaluation of $\eta_{aw}$ (uniform inlet flow) | experimental | 1 | adiabatic | no | no |
| evaluation of $\dot{q}$ (uniform inlet flow) | experimental | 1 | $323K$ | no | no |
| evaluation of $M_{is}$ (uniform inlet flow) | experimental | 1 | $323K$ | no | no |
| uniform | engine-like | 2 | adiabatic | no | no |
| swirl aligned to leading edge | engine-like | 2 | adiabatic | no | yes |
| swirl aligned to passage | engine-like | 2 | adiabatic | no | yes |
| uniform | engine-like | 2 | CHT | no | no |
| hot spot and swirl aligned to leading edge | engine-like | 2 | CHT | yes | yes |
| hot spot and swirl aligned to passage | engine-like | 2 | CHT | yes | yes |

Table 5.2: Test matrix.

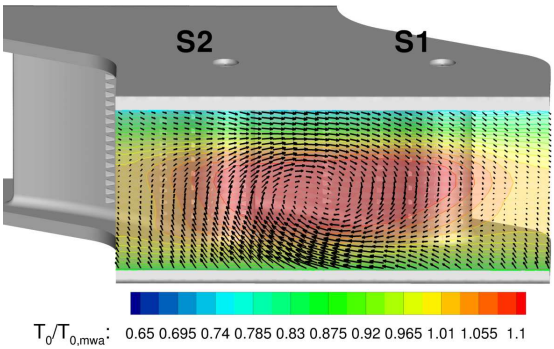


**(a)** passage aligned configuration

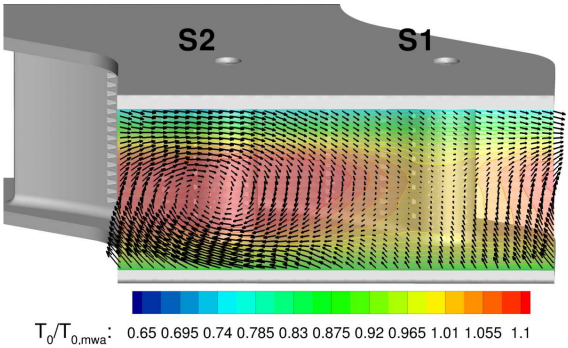


**(b)** leading edge aligned configuration

Figure 5.3: Relative alignments between inlet distortions and vanes.

scribed in the work by Salvadori et al. [74] and by Qureshi et al. [24]. The hot spot profile, already presented in Figure 1.5, is colloquially referred from the TATEF2 project as "EOTDF" (Enhanced Overall Temperature Distortion Factor). A measure of the spanwise and pitchwise temperature non-uniformities is given respectively as follows:

$$\frac{max(T_{0;t.a.}) - min(T_{0;t.a.})}{\overline{T_0}} = 0.335 \tag{5.1}$$

$$\frac{max(T_{0;s.a.}) - min(T_{0;s.a.})}{\overline{T_0}} = 0.14 \tag{5.2}$$

where $T_{0;t.a.}$ and $T_{0;s.a.}$ are respectively the tangentially-averaged and spanwise-averaged total temperature, while $\overline{T_0}$ is the total temperature averaged over the whole inlet surface and is equal to the one used for uniform simulations. A preferential spanwise variation is present, coherently with modern aero-engines.

The swirl profile, deriving from the work by Qureshi et al. [24], is shown in Figure 1.13.

Both hot spot and swirl have been rearranged in spanwise and pitchwise directions in order to be adapted to the geometry of the test case, obtaining a 1 : 2 ratio between non-uniformities and number of vanes. As mentioned previously, two different relative alignments between non-uniformities and vanes have been tested. The passage aligned configuration is shown in Figure 5.3(a) while the leading edge aligned one is reported in Figure 5.3(b).

When non-uniform inlet flows are analyzed, in order to maintain coherency between the minimum temperature of the non-uniform inlet profile and the coolant temperature, this latter has been reduced for the engine-like case. A coolant-to-main-flow temperature ratio of 0.598 has been used with main flow total temperature unaltered. Moreover air has been used as coolant, instead of using $CO_2$, without modifying its inlet pressure in order to obtain a nominal density ratio equal to the experimental case.

### 5.1.3 Numerical approach

Steady Reynolds-averaged Navier-Stokes simulations have been performed, on hybrid unstructured grids, using the commercial code ANSYS® Fluent. To ensure reliable results, a preliminary grid sensitivity analysis has been done, together with the assessment of the turbulence model. A second-order accurate upwind discretization has been applied in space, while gradients are reconstructed with the Green-Gauss node based approach. The pressure-based solver has been used in conjunction with the SIMPLE scheme for pressure-velocity coupling.

## 5.2 Model assessment

### 5.2.1 Grid sensitivity analysis

The geometry of a film-cooled vane is characterized by large variations of characteristic lengths from cooling channels diameter to vane chord. This implies that very different length scales of the flow are present, making grid generation a crucial issue. A grid dependence analysis has been carried out on the experimental configuration using hybrid unstructured grids generated with the commercial software Centaur$^{TM}$. A domain composed by a single vane (fluid only) has been used for this purpose. Prismatic layers are used near the walls to accurately reproduce boundary layer while tetrahedral elements fill the remaining volume. Refinements have been enforced in the cooling channels, near the vane surfaces and in the mixing zone between cooling flow and main stream. Four different grids have been generated consisting of about $3.66 \cdot 10^6$, $6.35 \cdot 10^6$, $14.2 \cdot 10^6$, and $25.9 \cdot 10^6$ elements. For all the grids the number of prismatic layers and their height are the same, in order to maintain the accuracy in the discretization of the boundary layer. For all the cases the average $y^+$ is about 0.3 and its maximum is about 0.92. Simulations of the grid sensitivity analysis has been performed using a re-calibrated version of the $k_T - k_L - \omega$ model (originally proposed by Walters and Cokljat [83]), which details will be provided in section 5.2.2.

Spanwise-averaged isentropic Mach number distributions are shown in Figure 5.4 for the various grid resolutions. Negligible variations have been observed therefore results are not sensitive to grid in terms of static pressure field. A more detailed evaluation demonstrates that strong effects of the grid resolution can be observed in terms of aggregated parameters. Figure 5.5 reports the dependence, with respect to the total number of elements, of mainstream and coolant mass flow rates as well as the average heat flux along the vane surface. Values are normalized with respect to the result corresponding to the finer grid. The mainstream mass flow is scarcely influenced by grid resolution but, on the contrary, a strong dependence can be observed for the coarse grids in terms of

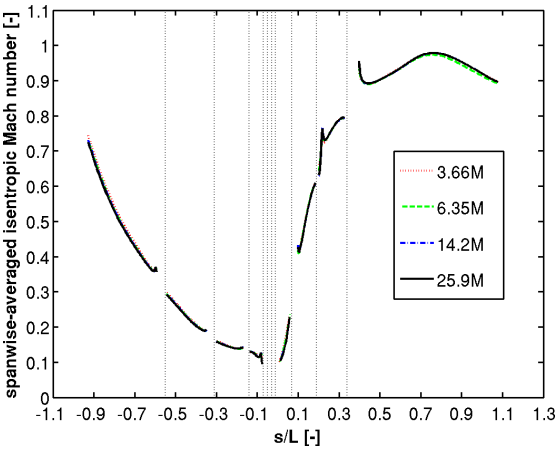


Figure 5.4: Effect of grid resolution in determining isentropic Mach number distribution on the cooled vane (experimental configuration).

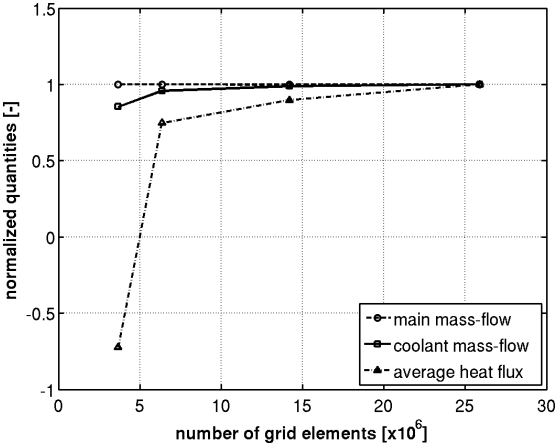


Figure 5.5: Effect of grid resolution in affecting mass flow rates and average heat fluxes over the blade surface.

coolant mass flow. The behavior becomes almost asymptotic passing from $14.2 \cdot 10^6$ to $25.9 \cdot 10^6$ elements. Heat flux is the most sensitive

to grid resolution. Although the difference in average heat flux prediction is reduced sensibly increasing the number of elements, non-negligible variations has been observed passing from $14.2 \cdot 10^6$ to $25.9 \cdot 10^6$ elements.

Grid effects have been quantified for the mass flows and total pressure losses using Grid Convergence Index (GCI) suggested by Roache et al. [84]. The value of the GCI for coolant mass flow on the finest meshes is 1.18% while for the total pressure loss coefficient is 0.45%. This latter is defined as follows:

$$\xi = \frac{p_{01;main} - p_{02}}{p_{02} - p_2} \tag{5.3}$$

It can be concluded that increasing the computational cost from the $14.2 \cdot 10^6$ elements to the $25.9 \cdot 10^6$ does not imply substantial variations in terms of the analyzed quantities. Despite the non-negligible change in terms of average heat flux remains, the $14.2 \cdot 10^6$ elements grid has been selected for the numerical campaign, resulting a trade-off between accuracy and computational costs. Once the distribution of the characteristic grid dimensions has been assessed it has also been applied to the engine-like domain. The grid obtained for such configuration, counts about $37 \cdot 10^6$ elements, including solid parts (vanes and endwalls). The obtained grids are shown in Figure 5.6.

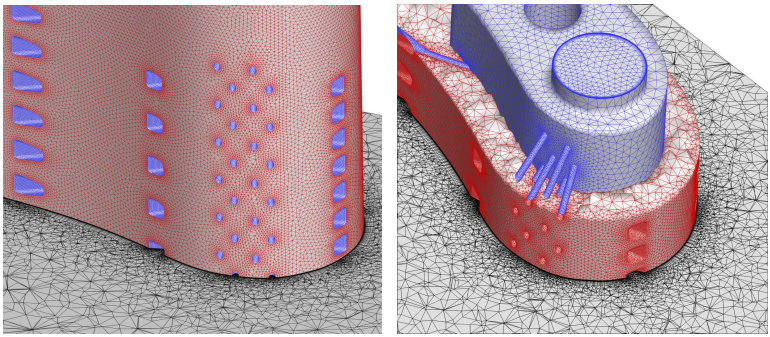

**(a)** experimental configuration **(b)** engine-like configuration

Figure 5.6: Computational grids of the tested configurations.

### 5.2.2 Turbulence model assessment

Once the appropriate resolution of the computational grid has been determined, an assessment of the turbulence model has been performed. Three different turbulence closures have been considered: the fully turbulent SST $k-\omega$ model by Menter [50], the transitional $k_T-k_L-\omega$ model in the original configuration proposed by Walters and Cokljat [83] and a re-calibrated version of this latter [85, 86].

The $k_T-k_L-\omega$ model is based on the $k-\omega$ structure and is able to predict both natural and bypass transition mechanisms. A third transport equation for laminar kinetic energy $k_L$ is added to predict the behavior of the low-frequency velocity fluctuations in the pre-transitional zone of the boundary layer. The $k_T-k_L-\omega$ model is not fully based on empirical correlations like other models but it is conceived on a phenomenological approach that makes it probably more suitable for engineering evaluations. However, the complexity of the physics that is the basis of transition process implies the use of a large number of model constants. For the re-calibrated version of the model four parameters have been modified with respects to the original set of 27 proposed by Walters and Cokljat [83]: $C_{R,NAT}$, $C_{NAT,crit}$, $C_\lambda$ and $C_R$. For the definitions of these parameters please refer directly to [83]. The choice of these parameters has been dictated by their role in the model. In fact, they control directly both natural and bypass transition and also the turbulence production term driven by strain rate. The re-calibration of the $k_T-k_L-\omega$ model has been based on thirteen RANS simulation, which results are not reported here for sake of brevity, that have been performed by varying empirically the selected parameters in order to match the experimental distribution of heat flux on a cooled vane different from the one analyzed here. The re-calibrated version of the model is characterized by $C_{R,NAT}=0$, $C_\lambda=2.2$ and $C_R=0.8$ while the $C_{NAT,crit}$ parameter losses its significance being $C_{R,NAT}=0$ (natural transition no more considered). Further details on the model calibration can be found in [85] and [86]. A detailed description of the calibration is provided in Appendix B.

The efficacy of the three tested turbulence models has been evaluated

based on the experimental data (extracted from the works by Jonsson and Ott [81] and Charbonnier et al. [82]) available in terms of spanwise-averaged adiabatic film cooling effectiveness and heat flux. The adiabatic film cooling effectiveness is defined as follows:

$$\eta_{aw} = \frac{T_{rec} - T_{aw}}{T_{0m,in} - T_{0c,in}} \tag{5.4}$$

where $T_{rec}$ is the mainstream recovery temperature, $T_{aw}$ is the adiabatic wall temperature while $T_{0m,in}$ and $T_{0c,in}$ are the total temperatures of respectively mainstream and coolant, measured on the corresponding inlet sections. The mainstream recovery temperature is calculated according to the classical definition:

$$T_{rec} = T + Pr^{1/3} \frac{u_{is}^2}{2c_p} \tag{5.5}$$

The distribution of the isentropic velocity $u_{is}$ along the vane has been calculated through the isentropic Mach number distribution obtained from a simulation of the uncooled geometry, according to the work by Charbonnier et al. [82]. It must be stated that the heat flux data are analyzed for a slightly different working condition with respect to what reported in Table 5.2: the main flow inlet pressure is equal to $1.493bar$ (with exit isentropic Mach number unchanged) and a coolant mass flow of $6.8g/s$ is imposed, coherently to [82]. A general good agreement is achieved between qualitative trends of prediction and experiments, as evident from Figures 5.7(a) and 5.7(b). Comparing the turbulence models tested, different behaviors are shown downstream of the cooling rows (represented via vertical dotted lines). From a quantitative point of view, turbulence models do not agree particularly downstream of the last cooling row moving from the leading edge to the trailing edge of the suction side (row 1). In fact for $s/L > 0.4$ the SST $k-\omega$ over-predicts adiabatic effectiveness while the original $k_T - k_L - \omega$ significantly under-predicts it. Same behavior is also highlighted for the heat flux. In such region, that covers a significant amount of the suction side of the blade, the re-calibrated $k_T - k_L - \omega$ shows the best performance. Looking also at the other

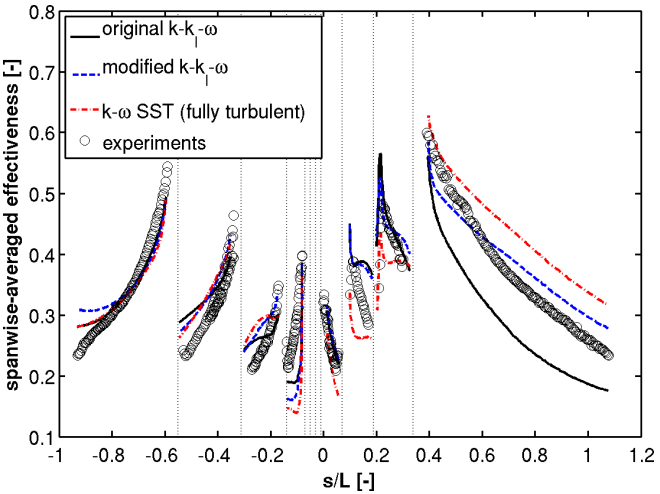


**(a)** spanwise-averaged adiabatic effectiveness

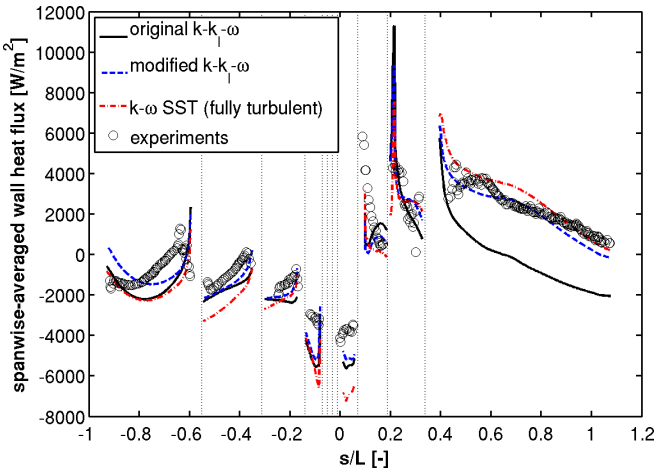


**(b)** spanwise-averaged heat flux

Figure 5.7: Effect of turbulence model in determining spanwise-avereraged distributions of adiabatic effectiveness and heat flux; pressure side for negative $s/L$.

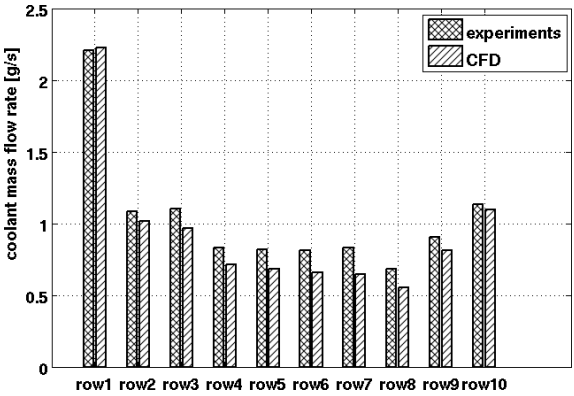


Figure 5.8: Row-by-row comparison of coolant mass flow rates obtained experimentally and numerically.

zones, this latter seems to be a good compromise for the prediction of both effectiveness and heat flux. Therefore it has been selected for the subsequent simulations. For the selected turbulence model, the coolant-to-mainstream mass flow ratio is evaluated as well the row by row coolant distribution. The experimental value of the first one is about 4.36% and is correctly predicted by the numerical simulations where a value of 4.22% is obtained. Concerning the coolant distribution, shown in Figure 5.8, a general good agreement is achieved. The over-prediction of the row 1 (the last of the suction side of the vane) and the under-predictions of the other rows with peaks in the leading edge region (rows 4 to 7) can be attributed to the different methodology used in evaluating the mass flow. While numerical simulation allows to evaluate the mass flow when all the cooling rows are feeded, a different approach has been followed to derive the experimental data. In the experimental case, coolant distribution were derived discharging coolant row by row into ambient pressure instead of using the back pressure imposed by the mainstream.

The isentropic Mach number distribution at 50% of the vane span, obtained with the re-calibrated $k_T - k_L - \omega$ turbulence model along the uncooled geometry is compared with experimental data in Figure 5.9. A

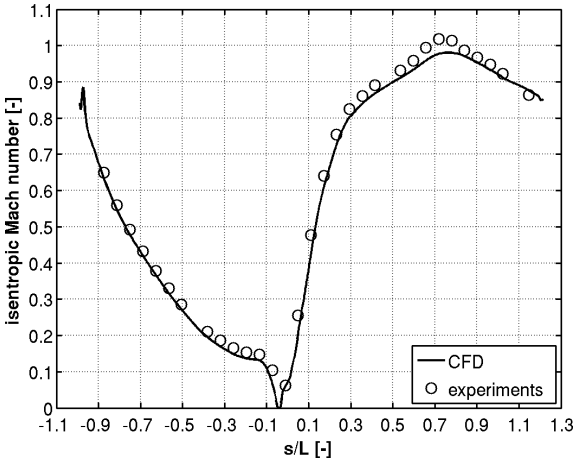


Figure 5.9: Isentropic Mach number distribution on the uncooled vane geometry: comparison between experimental data and numerical results.

general very good agreement is obtained, except for $0.6 < s/L < 0.8$ on the suction side, where the isentropic Mach number is slightly underestimated, however, the same behavior has been observed in literature [82].

## 5.3 Results

After validating the numerical setup in terms of grid resolution and turbulence model, results of the simulations with inlet distortions are presented in this section. Effects of swirl in determining film cooling effectiveness are initially evaluated considering only the fluid domain and subsequently the combined effect of hot spot and swirl are evaluated by means of conjugate heat transfer simulations.

### 5.3.1 Effect of swirl

Results for the doubled vane with uniform and swirled conditions are shown in Figure 5.10 in terms of adiabatic effectiveness. Uniform sim-

ulation shows a good overall covering effect of the film cooling system even if low effectiveness is present at the leading edge in the shroud region due to the downward angle of the showerhead holes. Consequently, a jet impinges the lower end-wall generating an advantage for its coverage. Swirling cases show three main effects on the adiabatic effectiveness. The first one is the effect of the main-flow incidence variation along the leading edge. This affects mainly showerhead behavior since the external pressure field is modified, leading to performance deterioration with respect to the uniform case. The second effect is that, despite the showerhead low efficacy, the modified working conditions imply a beneficial effect for the hub, which is partially covered by the jets coming from the showerhead itself, especially near the pressure side. The third effect is due to swirl migration and its interaction with cooling jets and secondary flows (enforcing lower passage vortex and suppressing higher). For the passage aligned case of Figures 5.10(c) and 5.10(d), swirl is convected inside the central passage thus affecting mainly the pressure side of the vane 1 and suction side of the vane 2, with detrimental effects respectively over the mid-span and under the midspan. For the leading edge aligned case of Figures 5.10(e) and 5.10(f) the vortex core is convected in the other passage thus affecting vane 2 pressure side and vane 1 suction side, showing analogous detrimental effects previously highlighted.

The distributions of total pressure losses, on a section located 0.16 axial chords downstream of the trailing edge, are reported in Figure 5.11 for the three cases. The quantity shown is the local loss coefficient, defined as follows:

$$\xi_{local} = \frac{\overline{p_{01}} - p_0}{\overline{p_0} - \overline{p}} \tag{5.6}$$

For the uniform case (5.11(a)), losses induced by secondary flows are evident near the endwalls, with a more marked loss coefficient near hub. The asymmetric behavior between hub and casing are due to the fact that the showerhead cooling system injects coolant with a downward velocity component. Different behaviors emerges for the two cases with inlet swirl (5.11(b) and 5.11(c)). The maximum peaks of loss coefficient are higher

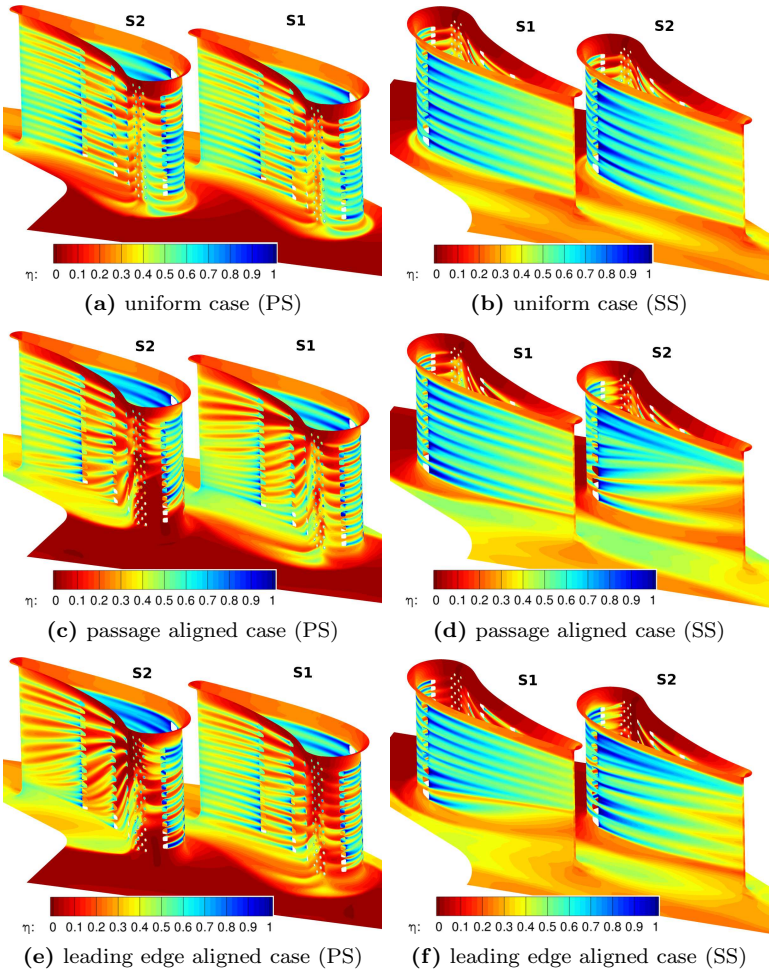


**(a)** uniform case (PS) **(b)** uniform case (SS)

**(c)** passage aligned case (PS) **(d)** passage aligned case (SS)

**(e)** leading edge aligned case (PS) **(f)** leading edge aligned case (SS)

Figure 5.10: Adiabatic film cooling effectiveness distributions along the vanes. Uniform case is compared with the two cases having inlet swirl in different clocking positions.

than in the uniform case. For both the cases, the maximum losses are generated in the upper part of the channel, downstream of the S2. With

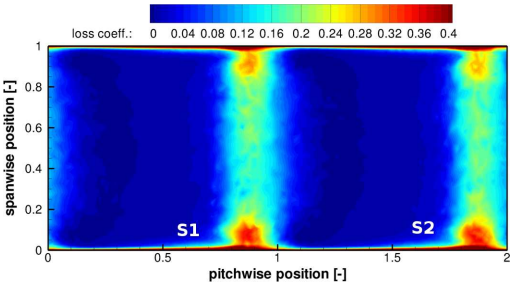


**(a)** uniform case

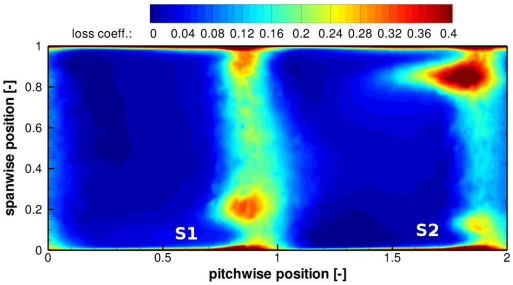


**(b)** passage aligned case

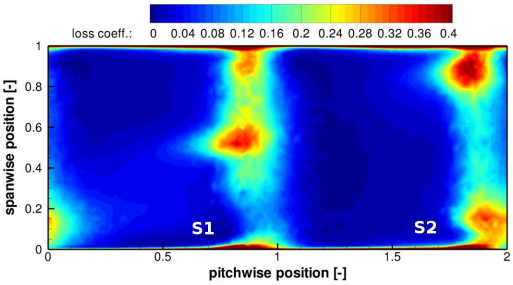


**(c)** leading edge aligned case

Figure 5.11: Loss coefficient distributions 0.16 axial chords downstream of the trailing edge. Observation point is downstream of the section.

respect to the uniform case, the shape of the wakes are distorted, especially for the passage aligned case, where a distortion coherent with the swirl direction can be observed. The strong interaction between swirl and

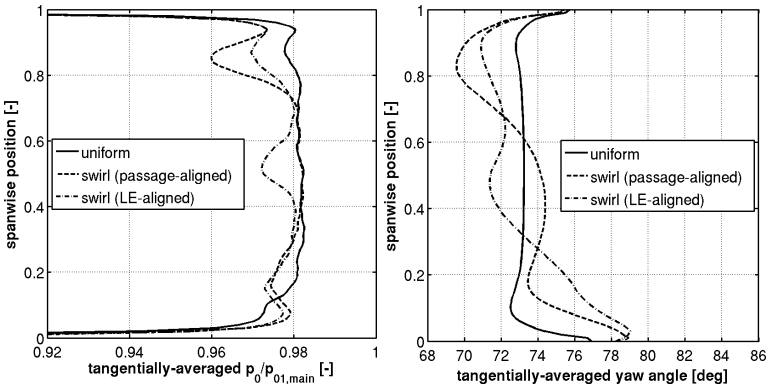


**(a)** total pressure **(b)** yaw angle

Figure 5.12: Pitchwise-averaged spanwise distributions of total pressure and yaw angle measured 0.16 axial chords downstream of the cascade.

secondary flows developing inside the passages leads to altered pitchwise-averaged distributions of both total pressure and yaw angle, respectively shown in Figures 5.12(a) and 5.12(b). In the spanwise distribution of the total pressure, the exact feature of the loss coefficient maps, shown in Figure 5.11, can be found. Losses are particularly relevant at 85% of the vane height in the passage aligned case, while the leading edge aligned case shows a minimum of total pressure close to midspan. The distorted non-uniform distribution of total pressure could significantly affect the development of secondary flows inside the downstream rotating row, which is also affected by a modified spanwise distribution of absolute yaw angle (5.12(b)). Considering this latter, the passage aligned case is characterized by significant underturning above 60% of the span with respect to the uniform case, while an overturning is present elsewhere. The underturning is less pronounced in the leading edge aligned case, even if more extended in the spanwise direction. Contrarily, the overturning is higher in the leading edge aligned case below 30% of the span. Looking at Figure 5.13, the effects of swirl in altering the aerodynamic load of the vanes can be clearly observed. Comparing the isentropic Mach number at 15%

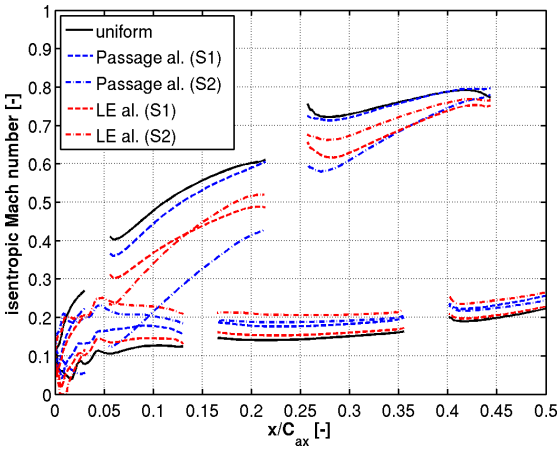


**(a)** 15% span

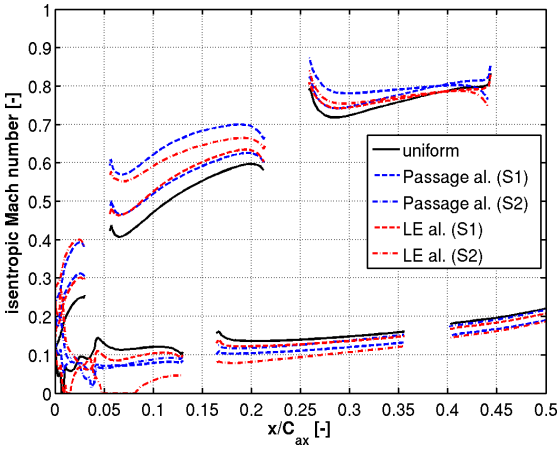


**(b)** 85% span

Figure 5.13: Isentropic Mach number distributions at 15% and 85% of the span; a detail on the first half of the axial chord is shown.

and 85% of the vane span for both the clocking positions, with respect to the uniform inlet condition, it is evident that swirl mainly affects S2 vane. A strong negative incidence is in fact observed at 15% of the span, while

a severe positive incidence is present at 85% of the span. This confirms the detrimental effects observed in Figure 5.10 in terms of adiabatic effectiveness, especially on the leading edge. This latter is in fact the part of the vane that is more affected by incidence variations caused by swirl. As a consequence, altered metal temperature distributions are expected.

### 5.3.2 Combined effect of swirl and inlet temperature non-uniformity

As one might expect, the combined presence of swirl and hot streak leads to a different transport of this latter with respect to a case without swirl. A representation of the hot streak migration is shown in Figure 5.14. As observable, the convection of the hot fluid inside the passages is dependent from the relative alignment between vanes and distortions. In the passage aligned case the hot spot is convected into the passage defined by the suction side of the S2 vane and the pressure side of the S1 vane. Swirl and secondary flows drive it towards the S2 suction side, where the aerodynamic effects generates some uncovered regions (see Figure 5.10(d)). In the leading edge aligned case, the hot fluid is directly convected to the leading edge of the S2 vane and the hot streak embraces the whole vane, maximizing the heat exchange on uncovered regions of the suction side. Moreover, the hot streamlines that in the leading edge aligned case reach the pressure side of the S2 vane are transported, towards the suction side of the S1 vane, in the lower corner near the trailing edge.

Figure 5.15 shows the thermal fields along the metal parts for the three cases. Before to highlight the characteristic behavior of the distorted cases, some general aspects, will be firstly evidenced. A first aspect is that the lower endwall is at a higher temperature than the upper one. This is due to the hot spot configuration that has the minimum temperature in the upper part of its spanwise distribution. A heat sink effect of the coolant entering the plenum also affects the upper endwall on both vanes. The temperature increase at mid-span due to the hot spot presence is lower than expected along all of the vanes, except for the S2 vane in the

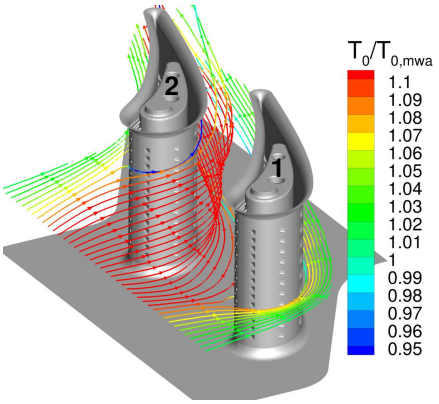


**(a)** passage aligned case

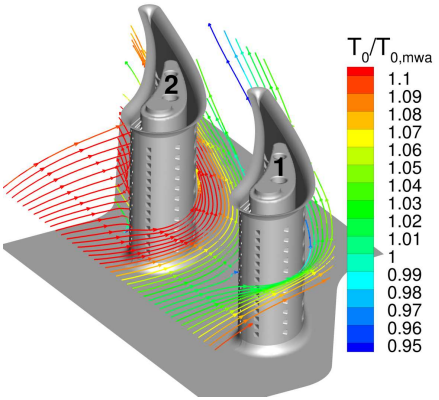


**(b)** leading edge aligned case

Figure 5.14: Different hot streak migration determined by swirl alignment with respect to the vanes.

leading edge aligned case that will be discussed later. This indicates that the cooling system remains effective enough to mitigate the effect of the incoming hot streak, especially in the front part of the vanes. However, it must be underlined that quite extended zones in the lower-rear part of the vanes undergoes a temperature increase. This effect is more aggressive on

the S2 vane for both clocking positions. The difference in terms of upper and lower regions on the vanes thermal field is another consequence of the hot spot radial temperature distribution (with its minimum temperature at the upper endwall). This affects the vane temperature both externally (a colder fluid convection in the upper vane region) and internally, due to conduction between vanes and endwalls with significant variations from upper to lower regions.

As previously stated both clocking positions experience an aggressive temperature increase on S2 vane lower-rear region. A detailed investigation demonstrates that the overheating is mainly due to two effects: the hot spot migration inside of the passage and the film cooling effectiveness reduction in the rear part of the suction side of the S2 vane. Due to swirl and secondary flows interaction, hot spot migration inside of the passages affects mainly the S2 vane in both the clocking positions. The S2 vane results also affected by strong aerodynamics effects caused by swirl that significantly alter the coverage effect provided by the cooling system.

Comparing Figures 5.15(c) and 5.15(d) with Figures 5.15(e) and 5.15(f), clocking effects can be highlighted. The previously described phenomena bringing the S2 vane to experience a higher temperature in the rear-lower region is more aggressive on the leading edge aligned configuration; with an increase of +4% in local temperature peak. Another clocking effect can be observed in the lower leading edge region of S2 vane for the leading edge aligned case, where a higher temperature is observed with respect to the other clocking position and the other vane in the same position. Since both configurations are similarly affected by swirl effects on the coverage performance of the cooling system, the increase in temperature has to be attributed to the hot spot migration; hot fluid is driven to the leading edge of the S2 vane. Finally, temperature of the lower endwall results higher in the region from the S1 suction side to the S2 pressure side for the leading edge aligned configuration. This is again a secondary effect of a previously described phenomenon. The hot spot transported towards the S1 rear-lower region is previously driven to the lower end-wall.

As evidenced, the hot spot migration is strongly affected by the rel-

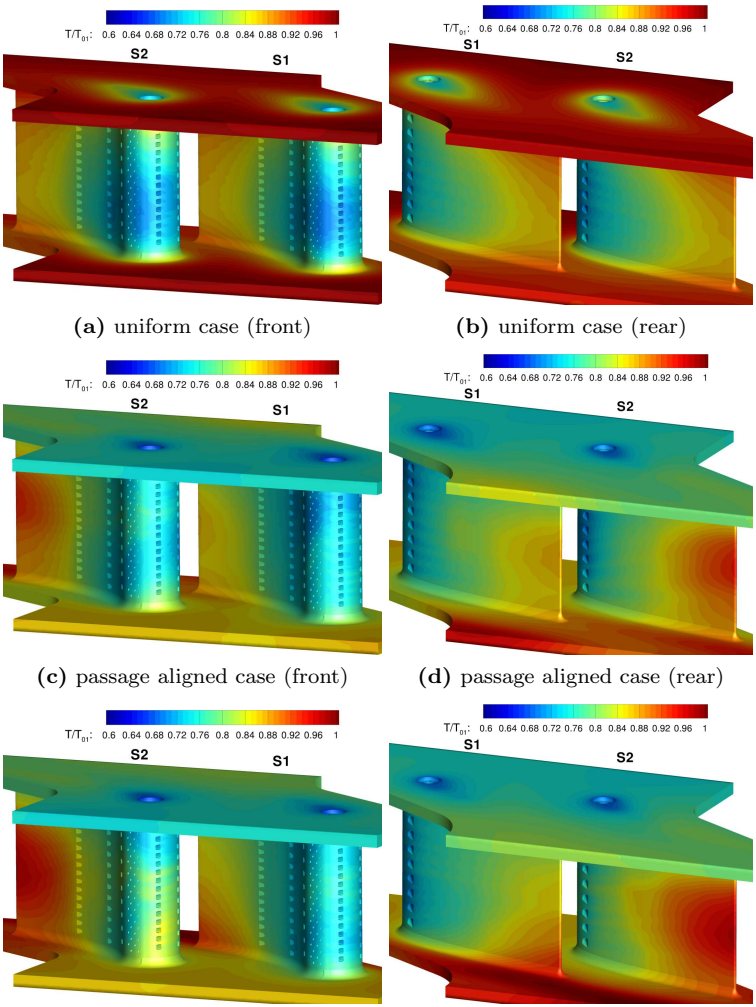


**(a)** uniform case (front) **(b)** uniform case (rear)

**(c)** passage aligned case (front) **(d)** passage aligned case (rear)

**(e)** leading edge aligned case (front) **(f)** leading edge aligned case (rear)

Figure 5.15: Non-dimensional temperature distributions along the vanes. Uniform case is compared with the two cases having inlet hot spot and swirl in different clocking positions.

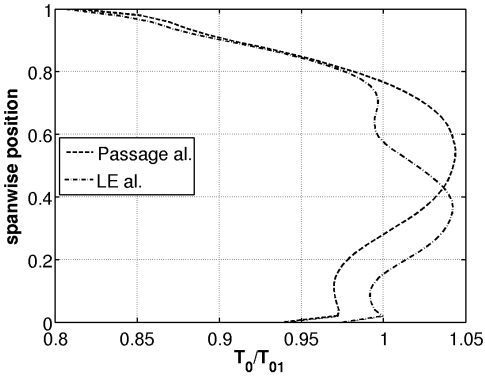


Figure 5.16: Pitchwise-averaged total temperature on the outlet section.

ative alignment between vanes and distortions. This not only alters the thermal behavior of the vane row but also will go to affect the downstream component. In fact, as shown in Figure 5.16, a different spanwise distribution of the pitchwise averaged total temperature emerges from the distorted cases. In particular, swirl of the leading edge aligned case tend to move the hot fluid downward with respect to the passage aligned case, determining an increased thermal load in the lower part of the downstream blades. Such zone are also the most stressed from a mechanical point of view, due to centrifugal force. This aspect is particularly important and should be considered during the design phase.

**Average thermal characteristics**

Figure 5.17 reports aggregated parameters in terms of non-dimensional averaged temperature and thermal power (positive from fluid to metal) for pressure and suction side as well as the overall data. Although the maximum temperature peaks are higher in the non-uniform cases, Figure 5.17 shows that the uniform inlet flow generates higher averaged temperatures, except for the S2 vane in the leading edge aligned configuration. This is due to the fact that the uniform inlet temperature profile is char-

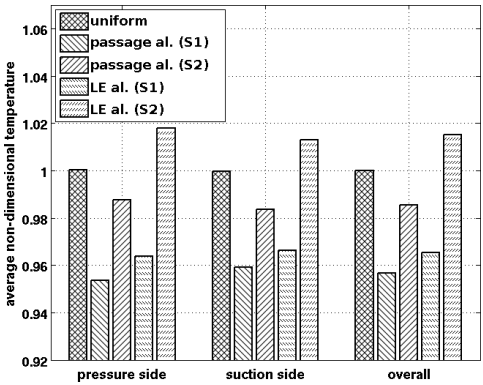


**(a)** temperature

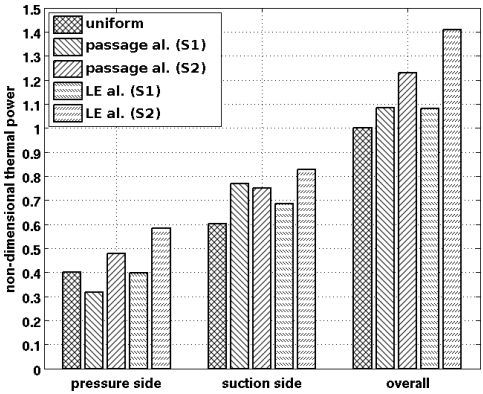


**(b)** thermal power

Figure 5.17: Average non-dimensional temperature and total thermal power: comparison between uniform case and hot spot with swirl.

acterized by higher temperatures near the endwalls with respect to the non-uniform cases. This overheats endwalls which, in turn, go to heat both the vanes via metal conduction.

The lower averaged temperatures experienced by both clocking positions (with the exception cited above) are due to the internal conductive effects. In fact, looking at the thermal power exchanged along the vanes,

it is possible to notice how in front of a decrease in averaged temperature, an increase in thermal power is shown. Since the thermal power represented is the external one, this implies that the contradiction raises from not considering all the actors in the phenomenon. Internal conductive fluxes needs to be considered demonstrating the important role of the internal heat exchange from and to the endwalls. As previously stated, the S2 vane in the leading edge aligned case is the only one experiencing an increase in averaged temperature. The reason has been discussed previously describing the temperature fields. In fact, the hot spot migration in the leading edge aligned case maximizes the external heat fluxes, especially where aerodynamics causes lack of coverage (e.g. S2 suction side). This increase is significant and sufficient to contrast internal conductive fluxes.

As a general observation, it is possible to state again that the S2 vane is always more thermally loaded than the S1. As previously discussed, this is mainly due to detrimental swirl effects and hot spot migration. Moreover, results allows to individuate the leading edge aligned case as the worst one, both in terms of temperature and thermal power.

**Performance of the showerhead cooling system**

The leading edge region of a HPV is critical from a thermal point of view due to the strong curvature of the surface that makes almost impossible to generate an attached film of coolant. For this reason showerhead holes, where large amounts of thermal power is extracted from the vanes via heat sink effect, results a constrained choice. Realistic inlet flows are characterized by strong swirl velocity components that sensibly alter the pressure distribution in the front part of the vanes, as previously demonstrated. For this reason the behavior of such cooling systems is particularly problematic. A detailed analysis of the showerhead operative conditions is presented in Figure 5.18. Figure 5.18(a) reports the thermal power removed along the internal surface of each showerhead channel, grouping the holes by row (see Figure 5.1).

Before to comment the effects of the non-uniform inlet profile, some

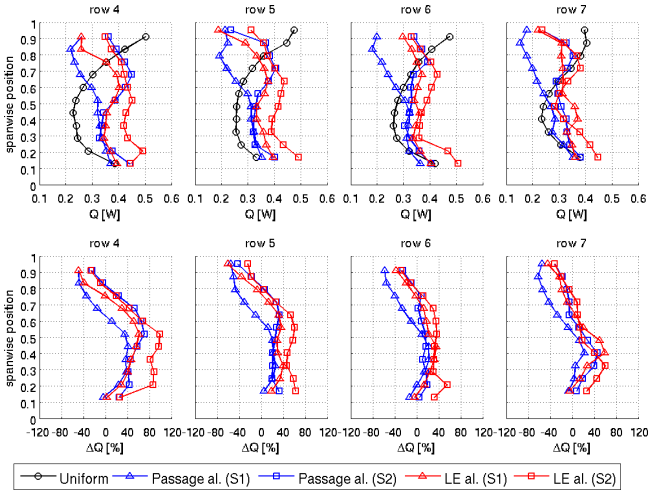


**(a)** thermal power

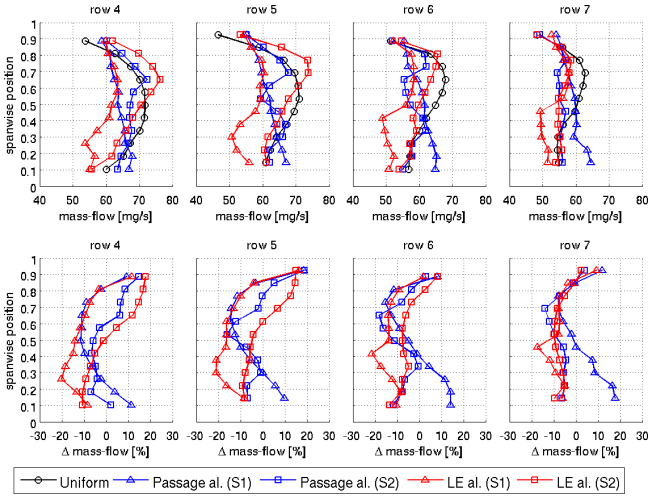


**(b)** coolant mass flow rate

Figure 5.18: Showerhead cooling system: spanwise distributions of thermal power removed by heat sink and coolant mass flow rate.

considerations have to be done about the uniform case. All the rows show a bow-shaped distribution of the thermal power due to the heat flux coming from the endwalls, where an adiabatic condition has been imposed on the top and bottom of the metal surfaces. The bow-shaped behavior of the rows 5 and 7 is slightly different in the upper part because these two rows are shifted upward by a half of the holes pitch, resulting then closer to the shroud with respect of row 4 and 6.

Remarkable differences are highlighted with realistic inlet conditions. An S-shaped behavior can be approximately evidenced for all the vanes in both the configurations. Except for the common behavior on the shroud region, where heat flux is reduced due to the colder part of the hot spot, significant variations are present. The S1 vanes results less thermally loaded and thus with a generally lower heat exchange via heat sink effect than the S2 vanes (for the reasons discussed previously). The spanwise oscillations slightly disappear moving from row 4 to row 7, except for the S1 vane of the passage aligned configuration that results almost insensitive. Qualitatively, it is possible to state that the showerhead system in leading edge aligned case extract more thermal power than in the passage aligned one. The percentage differences in terms of thermal power, whith respect to the uniform case, are reported in the lower part of Figure 5.18(a). From such figure it is possible to observe a behavior similar to a bow-shaped distribution that is due to the hot spot radial distribution. As expected, the positive peak is reached in the S2 vane of the leading edge aligned case at 50% of the span, where a +100% of thermal power is reached with respect to the uniform case.

Figure 5.18(b) reports a similar analysis for the mass flow passing through the showerhead channels, again grouped by row. As for the thermal power, the mass flow of the channels is characterized by a bow shaped distribution in the uniform inlet case although in the opposite sense. This behavior is due to the proximity of the upper and lower holes to the endwalls. Local effects of streamlines curvature and total pressure losses reduce the mass flow through that holes with respect to that far away from the endwalls. Concerning realistic inlet effects, it is possible

to observe a reduction of the mass flow spanwise variations moving from row 4 to row 7. A bow shaped distribution can be observed for the S2 vane in the leading edge aligned configuration. Considering percentage differences with respect to the uniform case (lower part of Figure 5.18(b)), in the upper region (above 50% of the span) the S1 vane discharges a lower mass flow with respect to the S2 vane, in particular the S2 vane of the leading edge aligned case reaches the maximum coolant mass flow ($76 g/s$ and a $+19\%$ difference). Again, this difference tends to disappear from row 4 to row 7. In the lower region, the S2 vanes shows reduced variations with respect to those of the S1 vane. An opposite behavior is highlighted with a reduction of mass flow with respect to the uniform case for the S1 vane of the leading edge aligned case (with a peak of $-22\%$) and an increase in the coolant mass flow on the S1 vane of the passage aligned case ($+20\%$).

# Conclusions

The field of combustor/turbine interaction is very complex and scarcely covered by scientific literature, limited to a few works. From a literature review it is emerged that the various aspects that characterize the interaction between the two components are treated with "fragmentation" and a very limited number of scientific paper gives a comprehensive vision of the problem. In fact, a large number of scientific works were dedicated in the past especially to the study of hot streaks propagation within turbine stages. Despite some works have gave a fundamental comprehension of the physical phenomena governing hot streaks propagation, most of the scientific papers considered only theoretical inlet temperature distortions, far from the actual one. Consideration of the additional non-uniformities in terms of residual swirl, turbulence intensity, turbulence length scale and total pressure have been analyzed only quite recently.

Due to complexity and costs of experimentation in this research field, computational fluid dynamics is necessary to understand the aerodynamic and thermal mechanisms. The comprehension of them is of great importance in the design process, helping to mitigate some deleterious aspects emerging from the combustor/turbine coupling.

In the field of CFD simulations, a problematic emerges about the specificities of the codes used for the resolution of the specific component. In fact, difficultly a CFD solver can provide accurate and stable solution of the nearly-incompressible reacting flow inside of the combustion chamber and contemporary allow analyzing the high Mach number flow through the downstream turbine stages. To overcome this prob-

lem, methods based on the use of coupled solvers emerged from scientific literature, although only a few works are present. In this context, a methodology finalized to coupled simulation of combustion chamber and high-pressure turbine has been developed in the first part of the thesis using different commercial and in-house solvers. The methodology has been applied to steady and unsteady RANS test cases, demonstrating an adequate reproduction of the experimental data available. Moreover, the subdivision of the computational domain in two coupled sub-domains has demonstrated to be not intrusive in the case of steady simulations. However, considering unsteady flows, a slight perturbation of the solution is introduced with respect to a case where the entire domain is simulate into a unique solver. The reason has been addressed to spurious reflections of pressure waves between the interfaces of the sub-domains and the resolution of this problem represents a possible evolution of the present work.

The steady coupling methodology developed has been applied to a realistic case of interaction between annular combustion chamber and uncooled high pressure vanes. Results, obtained with the RANS approach, have demonstrated the onset of aerodynamic and thermal aspect in the vane row that are not reproducible without considering the realistic working conditions that emerges from the combustor/high-pressure turbine coupling. The aggressive aerodynamic conditions at which vanes are subjected to, due to swirl originated from the burners, affects not only the operation of the vane row itself, but also the downstream components. In fact, tangentially averaged quantities on the stator/rotor interface, obtained considering the coupling between vanes and combustion chamber, are modified with respect to a case with uniform inlet conditions in the turbine.

A novel unsteady coupled approach based on zonal SAS/URANS simulations has been developed and validated on a simple test case. It is able to locally resolve turbulence structures in a predefined computational sub-domain (e.g. combustion chamber), resulting in a LES-like behavior, conserving the limited computational costs of the unsteady RANS ap-

proach in the remaining sub-domain (e.g. high-pressure turbine), where turbulence resolution would involve excessive computational resources. The application of the zonal SAS/URANS coupled approach to an actual case of interaction between combustion chamber and high-pressure turbine represents a future development of the present work, considering large scale turbulence that characterize the reactive flow in the combustor.

Having in mind the aggressive flow conditions at which the high-pressure vanes are subjected to, the effects of inlet distortions on cooled components have been analyzed in the second part of the work. In this field, open scientific literature is very limited. The studied linear cascade is equipped with a representative cooling system, characterized by showerhead holes along the leading edge and fan-shaped film cooling holes along pressure and suction side. Results, carried out with steady RANS conjugate heat transfer simulations, demonstrated the deleterious effects that inlet distortions have on the cooling system. In particular, the aggressive incidence changes induced by incoming swirl alters significantly the distribution of adiabatic effectiveness, affecting the protection of the surfaces against the hot fluid of the mainflow. Moreover, coherently with the results obtained in the first part of the thesis concerning the effects of combustor non-uniformities on uncooled vanes, strong changes in the pitchwise-averaged quantities downstream of the row have been observed.

The combined presence of hot streak and swirl lead to different aerothermal behaviors of the components in relation to the relative alignment between distortions and vanes. The analysis, that considered passage aligned and leading edge aligned configurations, permitted to individuate this latter as the most critical from the thermal point of view. Moreover, results have shown that inadequacy of simulation with uniform inlet conditions in reproducing the actual behavior of the cooling system. Particularly critical is resulted to be the showerhead cooling system, that is strongly affected by incidence variations caused by swirl.

As a general conclusion of the work, it is possible to state that strong attention should be dedicated in considering components integration for a

reliable prediction of the actual working conditions at which components are subjected to and, consequently, to guarantee a design able to optimize component life.

# Appendix A

# Effect of non-uniform chemical species distribution on the turbine inlet section

**Contents**



As mentioned in Chapter 4, going downstream to the combustor domain, the combustion process is assumed to be frozen. In this way computational costs, due to the use of combustion models within the turbine domain, are eliminated. Moreover, not only the combustion process is frozen downstream to the combustor domain, but another approximation is done concerning the distribution of the combustion products. These latter are not uniformly distributed on the combustor/turbine interface in the actual case. For this reason, in order to accurately describe the transport of chemical species, it should be necessary to use a single trans-

| | $n^\circ$ of elements on NGV | $n^\circ$ of elements on blade |
|---|---|---|
| coarse | 633234 | 784364 |
| medium | 1005920 | 1672940 |
| fine | 1805580 | 3324160 |
| very fine | 2727140 | 4925470 |

Table A.1: Grid dimensions for NGV and blade.

port equation for each chemical specie. This is obviously time-consuming and the simplification of assuming uniformly distributed species is done. Once a preliminary computation of the reactive flow in the combustor is obtained without considering the turbine, the mass-weighted average thermo-chemical properties are calculated on the plane corresponding to the inlet section of the turbine domain. Such average values define the properties of the "equivalent" ideal gas that is used in the turbine domain to reproduce the combustion products. In this Appendix, an estimation of the effects that the assumption of uniformly distributed species has on the aero-thermal results of the turbine domain is performed.

The test case used is the MT1 high-pressure turbine stage [7, 21, 66], of which both stator and rotor are considered. The whole stage is composed by 32 nozzle guide vanes and 60 unshrouded blades.

## A.1 Validation

Before to study the effect of the assumption of uniformly distributed chemical species, a preliminary validation of the computational model has been carried out using air with uniform inlet flow. Numerical results have been compared with the experimental data reported in [87]. The adequacy of the grids used has been evaluated by means of a grid sensitivity analysis. Four different multi-block structured grids, with increasing resolution, have been considered (the number of elements are reported in Table A.1). The same resolution of the boundary layer has been maintained for all the grids ($y^+_{max} \simeq 1$). Steady state simulations have been performed using the mixing plane model to reproduce sta-

tor/rotor interaction. In this way it is possible to consider one vane and one blade with different pitches without introducing geometry alterations to restore a even periodicity. Figure A.1 shows the computational grids used for NGV and blade (fine version).

A summary of the working conditions of the MT1 stage at the design point is reported in Table A.2. Such parameters have also been imposed as boundary conditions for the simulations carried out for the model validation.

The inlet section of the domain is located 0.67 NGV axial chords upstream of the vane leading edge while the stator/rotor interface is positioned 0.23 NGV axial chords downstream of the vane trailing edge. The outlet section of the domain is positioned about 1.51 rotor axial chords downstream of the blade trailing edge.

Simulations have been performed using ANSYS® CFX v14.5 [88]. The transitional SST $\gamma - \theta$ $k - \omega$ model by Langtry and Menter [89] has been used as a turbulence closure with a second-order-accurate spatial discretization.

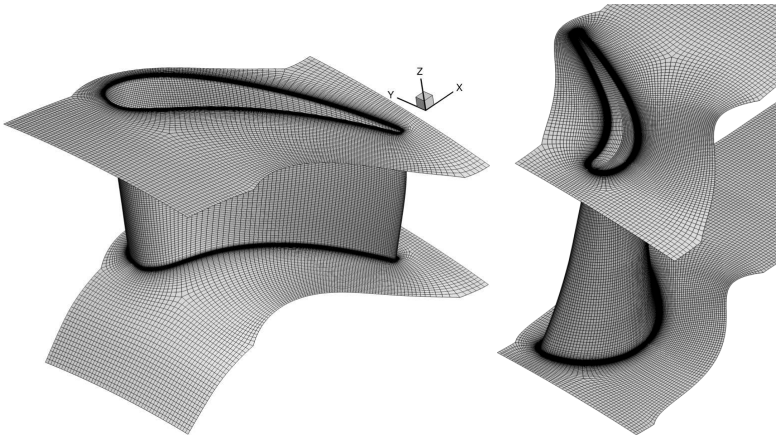


**(a)** NGV **(b)** rotor

Figure A.1: Structured grids (fine version) of the MT1 stage.

| | | |
|---|---|---|
| inlet total pressure | 4.6 | *bar* |
| inlet total temperature | 444 | *K* |
| inlet turbulence level | 5 | % |
| metal temperature | 289 | *K* |
| rotational speed | 9500 | *rpm* |
| rotor exit pressure (at hub) | 1.449 | *bar* |

Table A.2: MT1 working conditions.

Results in terms of isentropic Mach number along the vane are shown in Figure A.2 at three spanwise positions. The overall agreement is quite good, even if some discrepancies can be observed between experimental

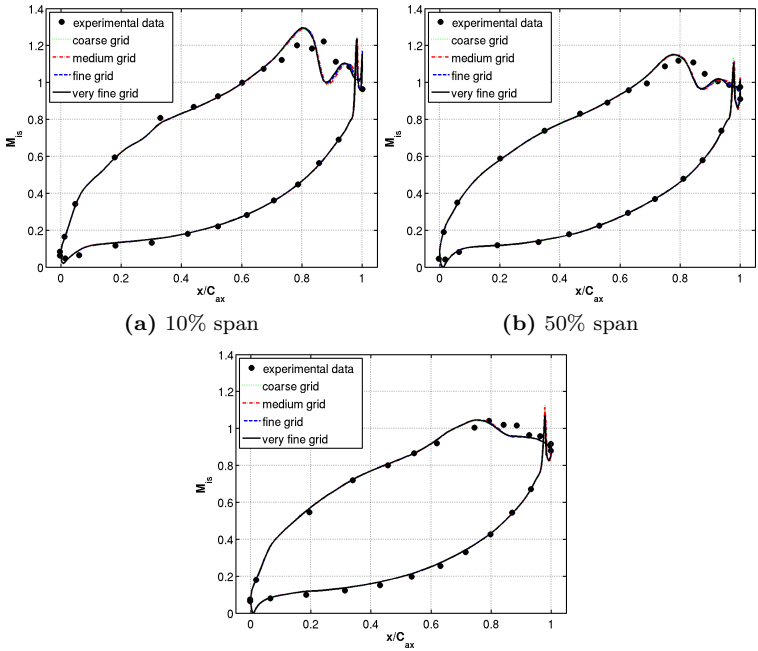


**(a)** 10% span **(b)** 50% span

**(c)** 90% span

Figure A.2: Isentropic Mach number distributions at three vane heights; comparison with experimental data.

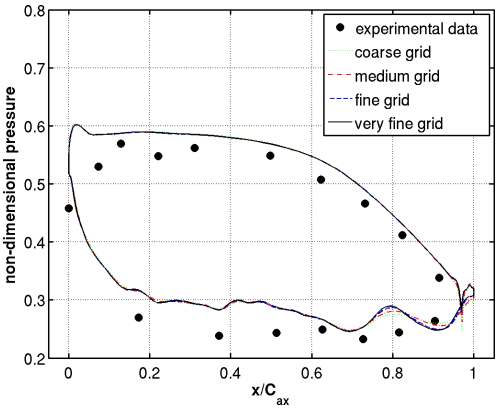


Figure A.3: Pressure distribution at midspant of the rotor; comparison with experimental data.

data and numerical results in the region $0.7 < x/C_{ax} < 0.9$. The errors can be ascribed to an erroneous prediction of the NGV back pressure determined by the mixing plane assumption that does not take into account unsteady effects. Secondarily, an uncertainty is introduced by the fact that fillets are present in the experimental model at the vane hub and shroud, as well as the blade hub, but they are not reproduced in the computational model. As evident in Figure A.2, the effect of grid resolution in altering the predicted isentropic Mach number distribution on the vane is limited to the rear region near hub.

A comparison of the non-dimensional pressure distribution between simulations and experiments along the midspan of the rotor blade is show in Figure A.3. Static pressure is normalized using the total pressure measured at the inlet section of the stage. The agreement of the numerical results with experiments is not as good as for the vane. Pressure is in fact overestimated by simulations along both pressure and suction side. However, similar difficulties in predicting the rotor blade load on the same test case have been also observed in literature, with different CFD codes and different eddy viscosity turbulence models, like for example

in the work by Salvadori et al. [87]. Neither the more accurate and computationally demanding LES approach proposed by Wang et al. [90] is able to correctly reproduce the experimental pressure distribution along the suctions side, nevertheless along the pressure side the agreement is improved with respect to steady and unsteady RANS.

The effect of grid resolution in determining the rotor pressure distribution is more marked with respect to what observed for the vane. The most appreciable variations are limited to the region $0.75 < x/C_{ax} < 1$, where the "fine" and "very fine" grids presents the same behavior.

After observing the effects of grid spacing in affecting the numerical solution, the "fine" version has been retained adequate for the subsequent simulations, being the "very fine" version more computationally demanding without providing benefits in the solution accuracy with respect to the selected one.

## A.2 Effects of chemical species transport

### A.2.1 Numerical approach

The effect of assuming uniformly distributed chemical species at the turbine inlet is investigated by means of the comparison between two different approaches. The first one using the actual chemical species distribution found in the annular combustion chamber analyzed in Chapter 4 (on a plane corresponding to the inlet section of the turbine) with a transport equation for each specie. The second one assuming the working fluid as a mixture of uniformly distributed chemical species, which mean composition equals the one found at the combustor exit section.

The temperature dependence of thermodynamic properties is described by means of the standard NASA format [91]. For the i-th specie, being $R$ the gas constant, it follows:

$$\frac{c_{p,i}}{R_i} = a_{1,i} + a_{2,i}T + a_{3,i}T^2 + a_{4,i}T^3 + a_{5,i}T^4 \tag{A.1}$$

$$\frac{h_i}{R_i} = a_{1,i}T + \frac{a_{2,i}}{2}T^2 + \frac{a_{3,i}}{3}T^3 + \frac{a_{4,i}}{4}T^4 + \frac{a_{5,i}}{5}T^5 + a_{6,i} \tag{A.2}$$

$$\frac{s_i}{R_i} = a_{1,i} lnT + a_{2,i} T + \frac{a_{3,i}}{2} T^2 + \frac{a_{4,i}}{3} T^3 + \frac{a_{5,i}}{4} T^4 + a_{7,i} \qquad \text{(A.3)}$$

where $a_{1 \div 7,i}$ are specific coefficients for the i-th specie. Two sets of coefficients have to be defined: one for a low-temperature interval and one for a high-temperature interval, which temperature ranges depend from the considered specie. To summarize, 14 coefficients characterize the thermodinamic properties of each specie. For the case considering species transport, such coefficients have been defined for each specie while, for the case with the "equivalent gas", coefficients have been calculated as averages weighted on the mass fraction of the specie measured on the inlet section on the domain of the computation with species transport. The temperature dependence of dynamic viscosity and thermal conductivity has been defined by means of the kinetic theory model [91].

The two approaches have been applied to simulations considering both isothermal and adiabatic conditions along the walls to respectively deduce wall heat flux and adiabatic wall temperature. A total amount of four steady simulations is then considered.

Only the four main chemical species are considered in the analysis: $CO_2$, $N_2$, $O_2$ and $H_2O$. Mass fractions of such species in the main flow are respectively 7.70%, 74.6%, 11.4% and 6.29%. In the case considering species transport, only three of the four species need to be transported (the selected ones are: $CO_2$, $O_2$ and $H_2O$); the concentration of the remaining one ($N_2$) is simply obtained from:

$$Y_{N_2} = 1 - (Y_{CO_2} + Y_{O_2} + Y_{H_2O}) \qquad \text{(A.4)}$$

Distributions of $CO_2$, $O_2$ and $H_2O$ at the turbine inlet section are reported in Figure A.4. As it is possible to observe, the effect of cooling flow is particularly evident from Figure A.4(b), where a high concentration of oxigen is present near the endwalls, while is reduced in the core of the flow due to the combustion process. The opposite happens for $CO_2$ and $H_2O$ (combustion products) whose concentration tends to decrease from the core of the flow to the endwalls.

The operating conditions simulated are the same reported in Table

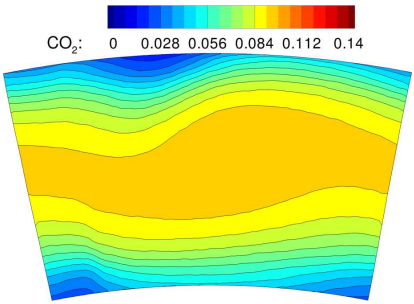


**(a)** $CO_2$

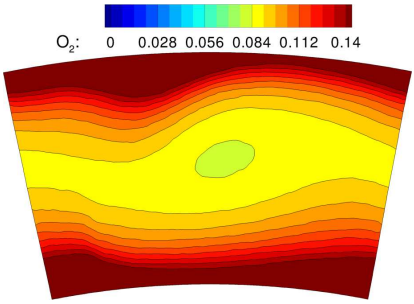


**(b)** $O_2$

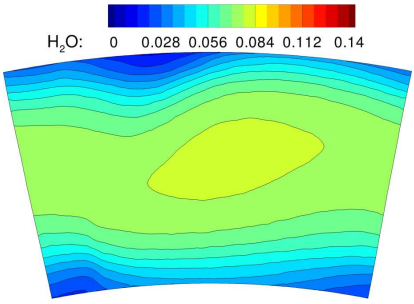


**(c)** $H_2O$

Figure A.4: Mass fractions of $CO_2$, $O_2$ and $H_2O$ at the inlet section of the turbine.

A.2, except that distorted inlet conditions are considered and a high turbulence level is introduced. Both the cases have been performed reproducing the realistic aero-thermal field on the turbine inlet section obtained from the combustor simulation including total temperature and total pressure non-uniformities as well as residual swirl. The average values of turbulence level and length scale, respectively equal to 21% and 1/50 of the channel height, have been uniformly imposed on the turbine inlet section. Since the combustor exit profiles have been obtained in real machine conditions, they have been rescaled to match the operating parameters of Table A.2 in terms of average inlet total temperature and total pressure. In this way the outlet pressure is maintained unchanged.

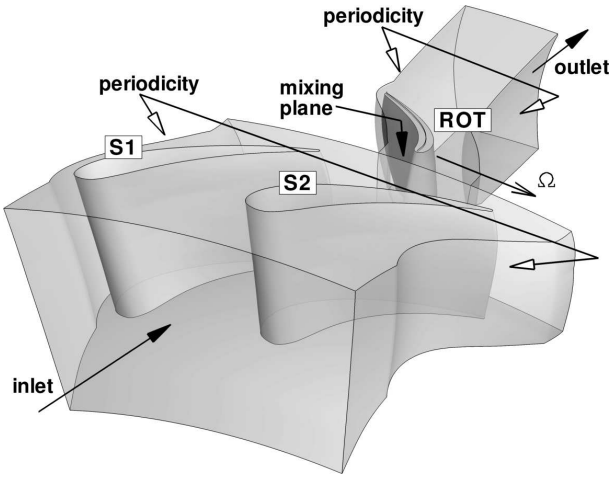


Figure A.5: Schematic of the computational domain.

Since the ratio between combustor burners and vanes is 1 : 2, two NGVs have been included in the computational domain with a single rotor blade downstream of them. As for the grid sensitivity analysis, the mixing plane approach has been used on the stator/rotor interface. A schematic of the computational domain is reported in Figure A.5.

### A.2.2 Results

#### Aerodynamics

Concerning vane aerodynamics, results have shown negligible variations introduced considering uniform species concentration. A slightly different behavior has been instead evidenced analyzing the blade row.

Figure A.6 shows the non-dimensional pressure distribution on the blade at three heights. Differences between the results are almost not appreciable along all the pressure side and in the rear part of the suction

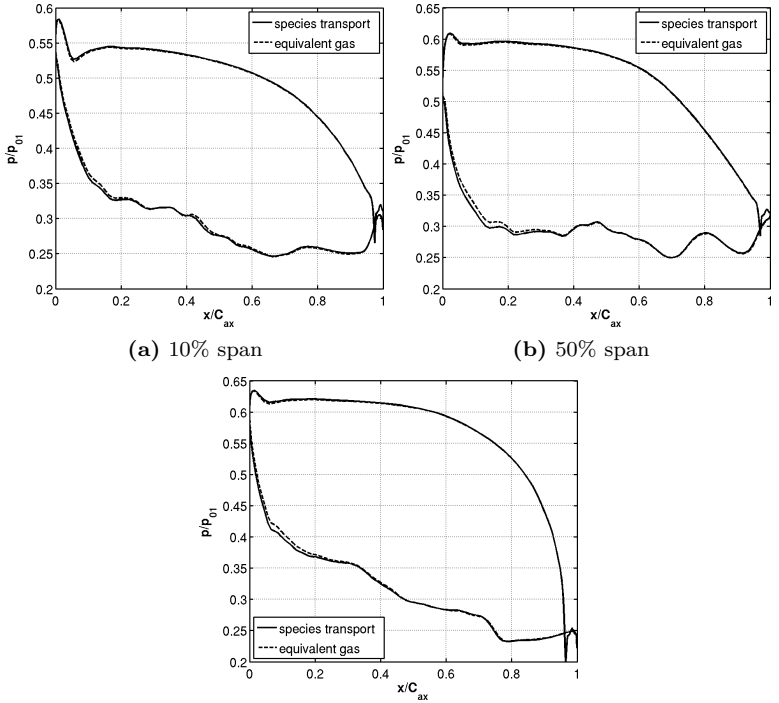


**(a)** 10% span **(b)** 50% span

**(c)** 90% span

Figure A.6: Effects of gas modeling on non-dimensional pressure distributions at three rotor heights.

side while the equivalent gas approach leads to underestimate pressure in the front part of the suction side, where the strongest flow acceleration is present. Figure A.7 shows a map of difference in the pressure estimation

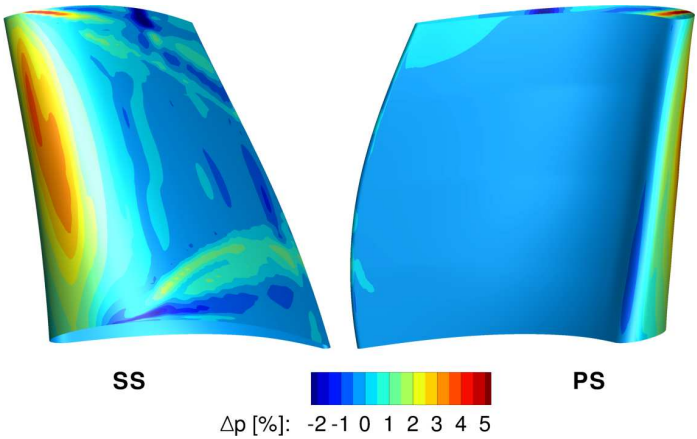


Figure A.7: Local pressure difference along the rotor surface between simulation with equivalent gas and species transport.

between the two approaches, having selected the approach with species transport as a reference. It confirms what evidenced in Figure A.6, allowing to localize the spot of pressure difference in the middle-upper part of the span along the suction side. Moreover, some differences, although quite limited, can be noted in the regions characterized by the development of secondary flows, especially near shroud (in correspondence of the tip leakage vortex). Figure A.8 reports radial distributions of tangentially averaged relative total pressure and yaw angle measured on a plane positioned half rotor axial chord downstream of the blade trailing edge. The prediction of both the quantities is very similar for the two approaches.

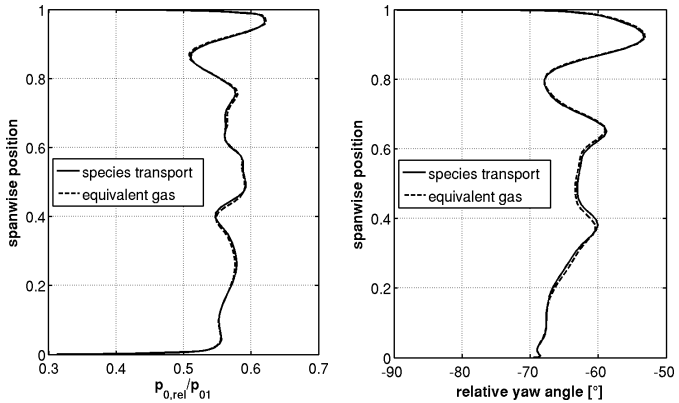


**(a)** relative total pressure **(b)** relative yaw angle

Figure A.8: Effects of gas modeling on tangentially averaged distributions of relative total pressure and yaw angle downstream of the rotor.

### Heat transfer

From a thermal point of view, the adiabatic wall temperature distribution along the vanes is resulted to be not altered by the simplifying assumption of uniform chemical species. Different considerations arises from the analysis of the heat flux along the vanes, extracted from the simulations with imposed wall temperature.

Distributions of heat flux are reported in Figure A.9 for the two vanes analyzed at three spanwise positions. The differences between the two vanes are due to the fact that the inlet flow is characterized by temperature distortions and swirl (see Figure 4.6). Pressure side is reported for negative $x/C_{ax}$. The abrupt increase of heat flux visible along the rear part of the suction side is due to the prediction of transition by the turbulence model. Differences between the two approaches for gas modeling emerges from the comparison between solid and dashed lines. At 50% of the span differences are negligible while at 10% and 90% limited differences appears in the front part of the suction side, where the approach

with the equivalent gas leads to a slight overestimation of the heat flux.

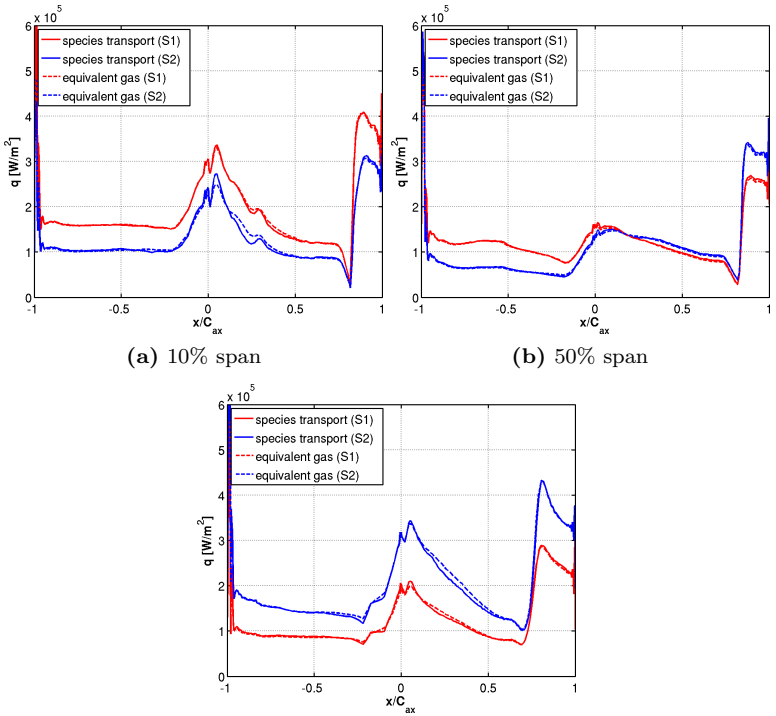


**(a)** 10% span

**(b)** 50% span

**(c)** 90% span

Figure A.9: Effects of gas modeling on heat flux distributions at three vane heights of the two vanes.

The heat flux distribution at three spanwise positions on the rotor surface is reported in Figure A.10. Distributions at 10% and 50% are qualitatively similar between them while, at 90%, a strong peak of heat flux is present on the suction side at $x/C_{ax} = 0.6$ due to the effect of the tip leakage vortex.

The local differences in heat flux prediction between the two approaches are more pronounced than for the vanes. A map showing the local percentage difference between the two approaches in the heat flux

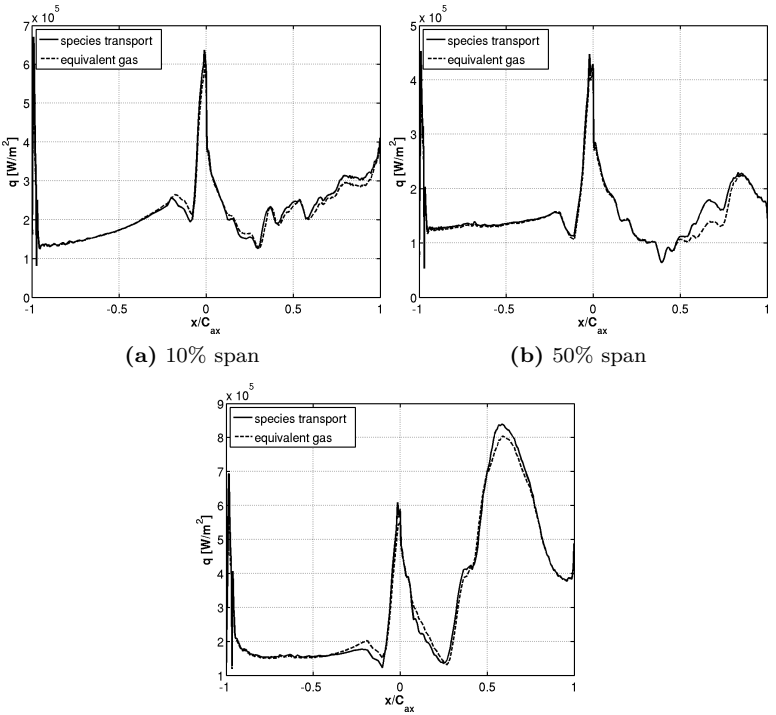


**(a)** 10% span **(b)** 50% span

**(c)** 90% span

Figure A.10: Effects of gas modeling on heat flux distributions at three rotor heights.

prediction is reported in Figure A.11(a). The maximum positive peak is higher than the absolute value of the minimum peak, indicating that the approach with the equivalent gas tends to provide mainly overestimations of heat flux with respect to considering species transport. Figure A.11(b) reports the local difference between the two approaches in the estimation of adiabatic wall temperature on the rotor surface. Differences are less pronounced with respect to the ones evidenced for heat flux. The characteristics patterns of secondary flows traces appear, indicating a slightly different prediction in the development of secondary flows.

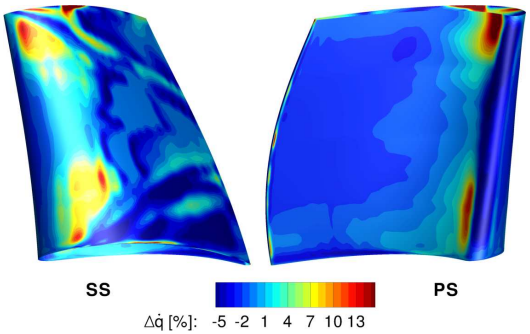


**(a)** $\Delta\dot{q}$

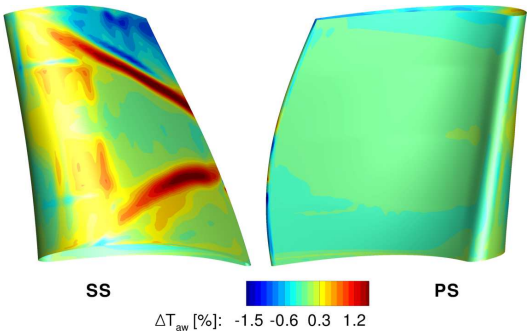


**(b)** $\Delta T_{aw}$

Figure A.11: Local difference of heat flux and adiabatic wall temperature between simulation with equivalent gas and species transport.

## A.3 Remarks

To summarize, results obtained from this study indicates that the effects introduced by approximating the composition of the gas entering the turbine as uniform are limited and affects mainly the blade row. Differences found in terms of pressure and adiabatic wall temperature distributions are small. Heat flux distribution along the blade is the most affected by the approximation due to local modifications in the predic-

tion of mixture properties and flow field characteristics. The magnitude of the differences found between the two studied approaches is comparable with what obtained by Wang and Yuan [92] for a similar study with unsteady RANS simulations. The differences found allow to retain that, the consideration of uniformly distributed chemical species in the turbine domain is not a heavy approximation, having in mind the common inaccuracies of the numerical models (at least for the (U)RANS approach) in reproducing experimental data.

# Appendix B

# Calibration of the $k_T - k_L - \omega$ turbulence model on a film cooled nozzle guide vane

**Contents**



As explained in Chapter 5, a re-calibrated version of the $k_T - k_L - \omega$ transitional turbulence model, originally proposed by Walters and Cokljat [83], has been used to simulate a film cooled nozzle guide vane. The calibration of the turbulence model has been done on the test case presented in this Appendix.

## B.1 Description of the test case

The test case used for the numerical activity is the vane of the MT1 high-pressure stage (in its annular version). This is an un-shrouded, high-pressure research turbine designed by Rolls-Royce and tested in the Isentropic Light Piston Facility (ILPF) by QinetiQ [93] [94]. The stage, composed by 32 vanes and 60 blades, has been tested in a cooled configuration with uniform inlet conditions during the Turbine Aero-Thermal External Flows (TATEF) project funded by the European Commission. Only the NGV is considered in the present analysis. The Reynolds number, based on the true chord of the Nozzle Guide Vane (NGV) and evaluated at the NGV outlet, which is positioned at the stage stator-rotor interface, is about $2.75 \cdot 10^6$ while the isentropic exit Mach number is about 0.942. The axial chord of the NGV is $38.8mm$.

For the NGV cooling system, air supply is assured by two plenum channels positioned inside of the vane. The diameter of the front and of the rear plenum is $10mm$ and $7mm$ respectively. Stagnation pressure is different between each plenum, leading to different coolant mass flows. Coolant reaches the vane surface through six rows of cylindrical holes: for each plenum, two rows are placed on the pressure side while a single row protects the suction side. The diameter of cooling channels is $0.6mm$ and all the rows have a spanwise pitch of $1.8mm$. The pressure side double row has an axial separation of $1.56mm$. All the cooling rows are characterized by an inclination angle of $50^\circ$ with respect to the local tangent on the vane surface. The nominal cooling non-dimensional parameters are reported by Chana and Mole [93]. Heat transfer measurements and pressure distributions along the surface of the vane are available from the experimental campaign. The vane operating conditions are summarized in Table B.1. Temperatures an pressures are normalized with respect to respectively the average inlet total temperature and average inlet total pressure.

| | inlet | plenum 1 | plenum 2 | wall | outlet |
|---|---|---|---|---|---|
| total pressure [−] | 1 | 1.365 | 1.061 | | |
| total temperature [−] | 1 | 0.645 | 0.645 | | |
| turb. level [%] | 6 | 5 | 5 | | |
| turb. length scale [$mm$] | 0.008 | 0.0004 | 0.0004 | | |
| metal temperature [−] | | | | 0.65 | |
| static pressure [−] | | | | | 0.565 |

Table B.1: Working conditions of the NGV.

### B.1.1 Numerical approach

Numerical simulations on hybrid unstructured grids have been performed using a steady approach with the commercial code ANSYS® Fluent. The transitional $k_T - k_L - \omega$ model by Walters and Cokljat [83] has been selected for the turbulence closure. A second-order-accurate upwind discretization has been applied in space, while gradients are reconstructed with the Green-Gauss node based approach. The SIMPLE scheme has been used for the pressure-velocity coupling. The computational domain, reported in Figure B.1(a), includes the whole fluid region, i.e. the external flow, the coolant interior channels and the supply plenums, colored in blue. Inlet and outlet sections are placed respectively about $0.65C_{ax}$ upstream of the leading edge and about $0.15C_{ax}$ downstream of the trailing edge. The inlet sections of the cooling flow are located on the side of the external endwall while the lower end is closed.

Total pressure, total temperature, turbulence level, turbulent length scale and flow direction have been imposed on the inlet sections, as well as zero laminar kinetic energy. The outlet section of the domain is located in correspondence of the stator/rotor interface and a static pressure map, obtained from the time-averaged solution of a previously performed unsteady simulation of the MT1 stage (see Salvadori et al. [74]), has been imposed to reproduce the radial and tangential pressure gradients.

### B.1.2 Grid dependence analysis

The geometry of a film cooled vane is characterized by large variations of characteristic lengths, from cooling channels diameter to vane chord.

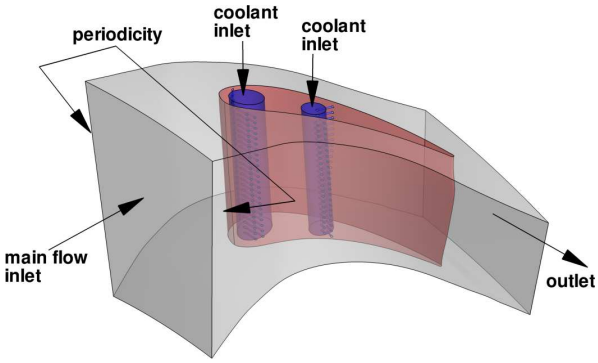


**(a)** computational domain

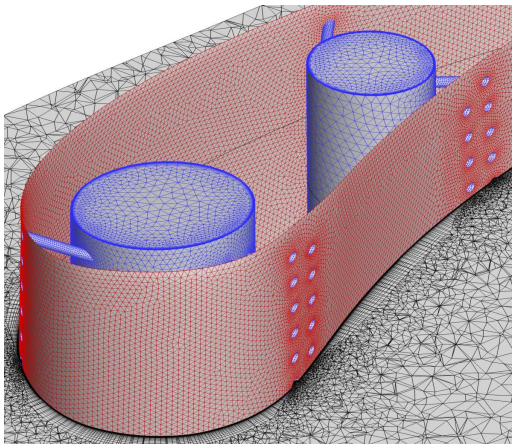

**(b)** grid

Figure B.1: Computational domain and grid of the cooled MT1 NGV.

This implies that very different length scales of the flow are present, and then grid generation must be considered a crucial issue in the simulation of such kind of components. A grid dependence analysis is the only way to limit the computational cost of the numerical campaign contemporaneously limiting the influence of grid resolution on the accuracy of the obtained results. For that reason a grid dependence analysis has been car-

| | $n^\circ$ of tetrahedra (x$10^6$) | $n^\circ$ of prisms (x$10^6$) | $\overline{y^+}$ | $y^+_{max}$ |
|---|---|---|---|---|
| $4M$ | 1.96 | 1.96 | 0.45 | 2.22 |
| $8M$ | 4.30 | 3.80 | 0.47 | 1.20 |
| $15M$ | 6.70 | 8.50 | 0.47 | 1.38 |
| $28M$ | 10.1 | 17.9 | 0.45 | 1.49 |

Table B.2: Characteristics of the computational grids used for grid sensitivity analysis.

ried out using hybrid unstructured grids generated with the commercial software Centaur$^{TM}$. Prismatic layers are used in the near wall region to better reproduce boundary layer development while tetrahedral elements are used to fill the remaining volume. The unstructured nature of the mesh allows obtaining local refinements where necessary, i.e. in the cooling channels and in the cross-flow zone between cooling flow and mainstream, as it is possible to observe in Figure B.1(b). Four different grids have been generated consisting of about $4 \cdot 10^6$, $8 \cdot 10^6$, $15 \cdot 10^6$ and $28 \cdot 10^6$ elements whose main characteristics are reported in Table B.2. The number of circumferential divisions of the cooling channels and the maximum element dimension on the vane surface have been limited to respectively increasing values moving from $4 \cdot 10^6$ to $28 \cdot 10^6$ elements. The presence of 30 prismatic layers adjacent to the vane walls has been enforced for all the investigated meshes in order to obtain the same accuracy in the discretization of the boundary layer. The number of prismatic layers has been maintained unchanged also in channels and plenums, as well as the expansion ratio between each layer. For the first three layers the expansion ratio is 1.0 while it changes to 1.2 from the fourth to the tenth and to 1.25 for the remaining prisms. The height of the first prismatic cell is coherent with a low Reynolds approach, as demonstrated by the $y^+$ values shown in Table B.2.

Results of the grid dependence analysis, in terms of isentropic Mach number distribution along the vane midspan, are shown in Figure B.2. All the grids are almost equivalent except for the coarse one (4M), that shows a different behavior immediately downstream of the last cooling

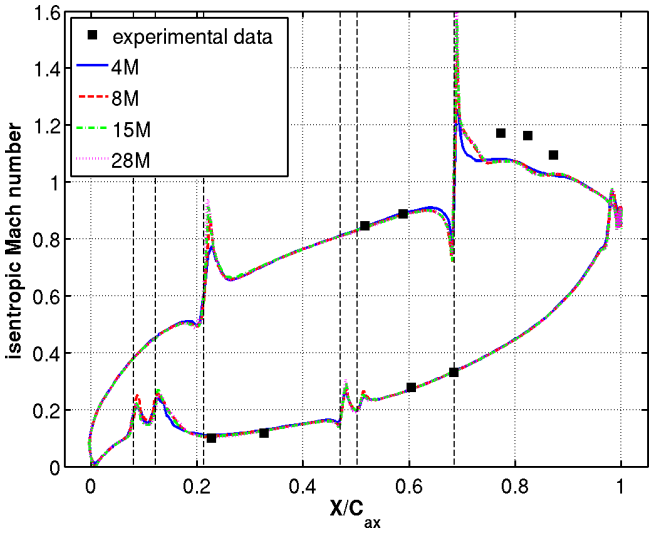


Figure B.2: Effect of grid resolution in determining the isentropic Mach number distribution at midspan of the vane.

row on the suction side. Some differences between the grids are also present downstream of the cooling holes (vertical dashed lines in the image), where peaks are filtered out in the coarser versions. A good agreement with the experimental data is achieved, except in the terminal part of the suction side probably due to the time-averaged exit condition which is not able to mimic the real effect of stator-rotor interaction.

Figure B.3 shows the trend of mass flows of the mainstream and the two plenums. Values are normalized with respect to the result obtained using the 28M grid. All the flow rates show an asymptotic behavior increasing the number of elements. Although the higher discrepancies are individuated on the coolant mass flows, variations of 2.6% for the front plenum and 3.1% for the rear one, between the 15M grid and the 28M grid, are considered acceptable for the objectives of the activity, especially considering that computational costs are doubled.

In Figure B.4 a detailed view of the secondary flow structures down-

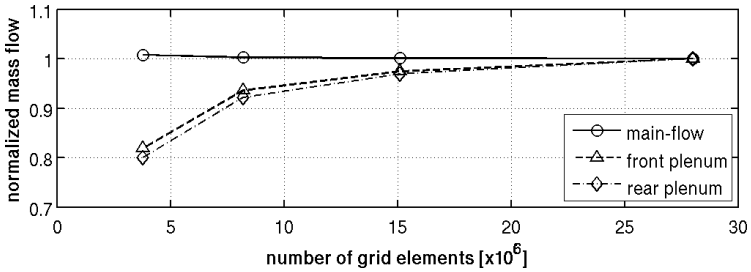


Figure B.3: Normalized mass flow of mainstream, front and rear plenums.

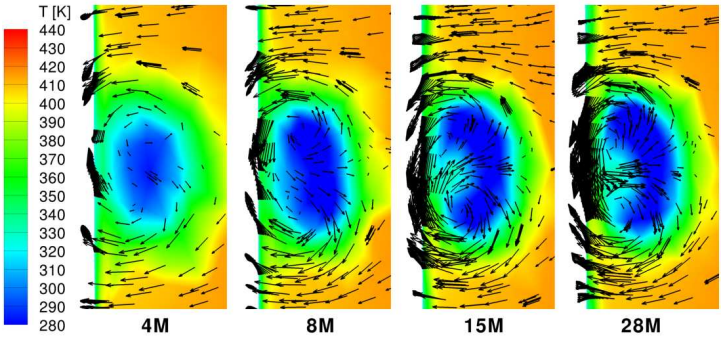


Figure B.4: View of the kidney vortices downstream of a cooling hole on suction side at mid-span as a function of the number of grid elements.

stream of a cooling hole located at mid-span on the suction side is shown. The section is obtained about six diameters downstream to the hole itself. The classical kidney vortex structure is not present in the solution obtained with the 4M grid, while in the 8M grid it is poorly defined. In the 28M grid it appears to be sufficiently well defined, but also in the 15M grid is very similarly.

After the grid dependence analysis it could be concluded that evaluating the adequacy of a grid relying only on aerodynamic parameters like the isentropic Mach number distribution would have been incorrect, because it would lead to select a grid that filters out some of the flow struc-

tures that drive heat transfer. The analysis demonstrates that doubling the computational cost from 15M elements to 28M does not introduce dramatic improvements in the accuracy of the solution, therefore for the subsequent simulations the 15M grid is used.

## B.2 Empirical re-calibration of the $k_T - k_L - \omega$ model

Before to show the results of the calibration it is worth to give a detailed description of the mathematical formulation of the model in order to allow the comprehension of the way in which the calibration goes to act. The $k_T - k_L - \omega$ model proposed by Walters and Cokljat [83] uses three transport equations for turbulent kinetic energy ($k_T$), laminar kinetic energy ($k_L$) and specific dissipation rate $\omega$:

$$\frac{D(\rho k_T)}{Dt} = \rho\big(P_{k_T} + R_{BP} + R_{NAT} - \omega k_T - D_T\big) + \frac{\partial}{\partial x_j}\left[\left(\mu + \frac{\rho\alpha_T}{\sigma_k}\right)\frac{\partial k_T}{\partial x_j}\right] \tag{B.1}$$

$$\frac{D(\rho k_L)}{Dt} = \rho\big(P_{k_L} - R_{BP} - R_{NAT} - D_L\big) + \frac{\partial}{\partial x_j}\left[\mu\frac{\partial k_L}{\partial x_j}\right] \tag{B.2}$$

$$\frac{D(\rho\omega)}{Dt} = \rho\left[C_{\omega 1}\frac{\omega}{k_T}P_{k_T} + \left(\frac{C_{\omega R}}{f_W} - 1\right)\frac{\omega}{k_T}(R_{BP} + R_{NAT}) - C_{\omega 2}\omega^2 + C_{\omega 3}f_\omega\alpha_T f_W^2\frac{\sqrt{k_T}}{d^3}\right] + \frac{\partial}{\partial x_j}\left[\left(\mu + \frac{\rho\alpha_T}{\sigma_\omega}\right)\frac{\partial\omega}{\partial x_j}\right] \tag{B.3}$$

where $d$ is the wall distance. The total "fluctuation" energy is given by $k_{tot} = k_T + k_L$. Having defined $S$ as the magnitude of the strain rate tensor, the production terms for turbulent and laminar kinetic energy are respectively given by:

$$P_{k_T} = \nu_{T,s}S^2 \quad , \quad P_{k_L} = \nu_{T,l}S^2 \tag{B.4}$$

For the production term of turbulent kinetic energy we have:

$$\nu_{T,s} = f_\nu f_{INT} C_\mu \sqrt{k_{T,s}}\lambda_{eff} \tag{B.5}$$

where the effective small-scale turbulence $k_{T,s}$ is given by:

$$k_{T,s} = f_{SS} f_W k_T \tag{B.6}$$

$f_W$ is a wall damping function. $\lambda_{eff}$ is the effective length scale that is calculated using the following limiting function:

$$\lambda_{eff} = min(C_\lambda d, \lambda_T) \tag{B.7}$$

Defining the turbulent length scale $\lambda_T$ using the classical definition $\lambda_T = \frac{\sqrt{k_T}}{\omega}$, the wall damping function is given by:

$$f_W = \frac{\lambda_{eff}}{\lambda_T} \tag{B.8}$$

The function $f_\nu$ is computed by means of the effective turbulent Reynolds number:

$$f_\nu = 1 - e^{-\frac{\sqrt{Re_T}}{A_\nu}} \tag{B.9}$$

$$Re_T = \frac{f_W^2 k_T}{\nu\omega} \tag{B.10}$$

The function $f_{SS}$ that models the so-called "shear-sheltering" effect is defined by:

$$f_{SS} = e^{-\left(\frac{C_{SS}\nu\Omega}{k_T}\right)^2} \tag{B.11}$$

The coefficient $C_\mu$ in the definition turbulent viscosity is defined by:

$$C_\mu = \frac{1}{A_0 + A_s \frac{S}{\omega}} \tag{B.12}$$

The effect of intermittency on the turbulence production is introduced by means of the dampind function:

$$f_{INT} = min\left(\frac{k_L}{C_{INT} k_{tot}}, 1\right) \tag{B.13}$$

Concerning the production of laminar kinetic energy (second definition of B.4), it is assumed to be governed by large-scale near-wall tur-

bulent fluctuations that is obtained from $k_T$ and the previously defined $k_{T,s}$ contribution due to small-scale fluctuations: $k_{T,l} = k_T - k_{T,s}$. The turbulent viscosity associated to the large-scale fluctuations is expressed as:

$$\nu_{T,l} = min\left[ f_{\tau,l} C_{l1} \left( \frac{\Omega \lambda_{eff}^2}{\nu} \right) \sqrt{k_{T,l}} \lambda_{eff} + \right. \\ \left. + \beta_{TS} C_{l2} Re_\Omega d^2 \Omega, \frac{0.5(k_L + k_{T,l})}{S} \right] \tag{B.14}$$

where

$$Re_\Omega = \frac{d^2 \Omega}{\nu} \tag{B.15}$$

$$\beta_{TS} = 1 - e^{-\frac{max(Re_\Omega - C_{TS,crit}, 0)^2}{A_{TS}}} \tag{B.16}$$

$$f_{\tau,l} = 1 - e^{-C_{\tau,l} \frac{k_{T,l}}{\lambda_{eff}^2 \Omega^2}} \tag{B.17}$$

The near-wall dissipation terms for $k_T$ and $k_L$ are expressed respectively as:

$$D_T = \nu \frac{\partial \sqrt{k_T}}{\partial x_j} \frac{\partial \sqrt{k_T}}{\partial x_j} \qquad D_L = \nu \frac{\partial \sqrt{k_L}}{\partial x_j} \frac{\partial \sqrt{k_L}}{\partial x_j} \tag{B.18}$$

For the transport equations of $k_T$ and $\omega$, the effective diffusivity $\alpha_T$ is defined by:

$$\alpha_T = f_\nu C_{\mu,std} \sqrt{k_{T,s}} \lambda_{eff} \tag{B.19}$$

The function $f_\omega$ is defined by:

$$f_\omega = 1 - e^{-0.41 \left( \frac{\lambda_{eff}}{\lambda_T} \right)^4} \tag{B.20}$$

The remaining terms are related to laminar-to-turbulent transition mechanisms and in particular to bypass transition ($R_{BP}$) and natural transition ($R_{NAT}$). Transition is represented by an energy transfer from $k_L$ to $k_T$ and for this reason the terms $R_{BP}$ and $R_{NAT}$ appears with

opposite signs in equations B.1 and B.2. Such terms are defined by:

$$R_{BP} = C_R \beta_{BP} k_L \omega / f_W \tag{B.21}$$

$$R_{NAT} = C_{R,NAT} \beta_{NAT} k_L \Omega \tag{B.22}$$

where

$$\beta_{BP} = 1 - e^{-\frac{\phi_{BP}}{A_{BP}}} \tag{B.23}$$

$$\phi_{BP} = max\left(\frac{k_T}{\nu\Omega} - C_{BP,crit}, 0\right) \tag{B.24}$$

$$\beta_{NAT} = 1 - e^{-\frac{\phi_{NAT}}{A_{NAT}}} \tag{B.25}$$

$$\phi_{NAT} = max\big(Re_\Omega - C_{NAT,crit}/f_{NAT,crit}, 0\big) \tag{B.26}$$

$$f_{NAT,crit} = 1 - e^{-C_{NC}\frac{\sqrt{k_l}d}{\nu}} \tag{B.27}$$

When heat transfer effects are considered, the turbulent thermal diffusivity $\alpha_\theta$ is introduced:

$$\alpha_\theta = f_W \frac{k_T}{k_{tot}} \frac{\nu_{T,s}}{Pr_\theta} + (1 - f_W) C_{\alpha,\theta} \sqrt{k_T} \lambda_{eff} \tag{B.28}$$

The turbulent viscosity to be used in the momentum equation is the sum of the contributions due to large-scale and small-scale fluctuations:

$$\nu_T = \nu_{T,s} + \nu_{T,l} \tag{B.29}$$

All the parameters not explicitly defined are models constants. The complete summary of all the model constants of the original formulation by Walters and Cokljat [83] is reported in Table B.3. Due to the complexity of the physical phenomena involved in laminar-to-turbulent transition, the model is characterized by a considerable amount of parameters (27).

The re-calibration of the $k_T - k_L - \omega$ model is based on the empirical modification of some of the parameters listed in Table B.3 in order to match the experimental distribution of Nusselt number along the midspan

| | | | |
|---|---|---|---|
| $A_0 = 4.04$ | $C_{NC} = 0.1$ | $C_R = 0.12$ | $C_{\omega,R} = 1.5$ |
| $A_s = 2.12$ | $C_{NAT,crit} = 1250$ | $C_{\alpha,\theta} = 0.035$ | $C_\lambda = 2.495$ |
| $A_\nu = 6.75$ | $C_{INT} = 0.75$ | $C_{SS} = 1.5$ | $C_{\mu,std} = 0.09$ |
| $A_{BP} = 0.6$ | $C_{TS,crit} = 1000$ | $C_{\tau,l} = 4360$ | $Pr_\theta = 0.85$ |
| $A_{NAT} = 200$ | $C_{R,NAT} = 0.02$ | $C_{\omega,1} = 0.44$ | $\sigma_k = 1$ |
| $A_{TS} = 200$ | $C_{l1} = 3.4 \cdot 10^{-6}$ | $C_{\omega,2} = 0.92$ | $\sigma_\omega = 1.17$ |
| $C_{BP,crit} = 1.2$ | $C_{l2} = 1.0 \cdot 10^{-10}$ | $C_{\omega,3} = 0.3$ | |

Table B.3: Model constant of the original formulation of the $k_T - k_L - \omega$ model proposed by Walters and Cokljat [83].

of the vane. The Nusselt number definition is:

$$Nu = \frac{\dot{q}}{T_{rec,main} - T_w} \frac{C_{ax}}{k} \tag{B.30}$$

where $q$ is the local heat flux measured along the vane surface, $T_{rec,main}$ is the recovery temperature of the mainstream, $T_w$ is the wall temperature imposed as boundary condition, $C_{ax}$ the axial chord of the profile and $k$ the thermal conductivity of the fluid (air) measured at the stagnation temperature of the mainflow at the inlet of the domain.

The parameters chosen for the re-calibration are $C_{R,NAT}$, $C_{NAT,crit}$, $C_\lambda$ and $C_R$. The choice of these parameters has been dictated by their role in the model. In fact, as shown above, they control directly both natural and bypass transition and also the turbulence production term driven by strain rate. A total amount of twelve runs have been performed varying the selected parameters. Table B.4 summarizes all the configurations tested. For sake of brevity, only the most promising sets of parameters are commented in the follow, referred as SET1, SET2 and SET3 in Table B.4. Figure B.5 reports the Nusselt number distributions along the vane midspan, obtained with the original model constants and with the modified ones. With the original constants (continuous black line) non-negligible discrepancies are present with respect to the experimental data. Nusselt number in the terminal part of the pressure side is completely miss-predicted since CFD results provide an opposite behavior with respect to experiments. Furthermore, downstream of the first cooling row along the suction side a non-physical flat Nusselt number

| run ID | $C_{R,NAT}$ | $C_{NAT,crit}$ | $C_\lambda$ | $C_R$ |
|---|---|---|---|---|
| original model [83] | 0.02 | 1250 | 2.495 | 0.12 |
| test00 | 0.03 | 1000 | 2.495 | 0.24 |
| test01 | 0.03 | 1200 | 2.495 | 0.30 |
| test02 | 0.02 | 1250 | 2.495 | 0.40 |
| test03 | 0.02 | 1250 | 2.495 | 0.60 |
| test04 (SET1) | 0.00 | – | 2.495 | 0.60 |
| test05 | 0.00 | – | 2.000 | 0.60 |
| test06 | 0 | – | 2.000 | 0.80 |
| test07 (SET2) | 0 | – | 2.200 | 0.80 |
| test08 | 0 | – | 2.200 | 1.00 |
| test09 (SET3) | 0 | – | 1.800 | 1.40 |
| test10 | 0 | – | 2.000 | 1.80 |
| test11 | 0 | – | 2.000 | 2.40 |

Table B.4: Summary of all the tests performed for the model calibration.

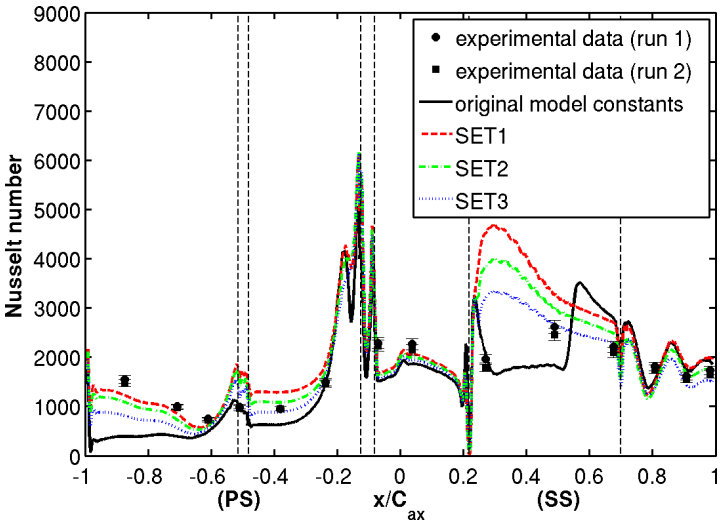


Figure B.5: Nusselt number distributions along the midspan of the cooled vane.

behavior is observed in the interval $0.28 < x/C_{ax} < 0.53$. Since experimental sensors are quite distant it is not easy to state the real behavior of the Nusselt number but, it is reasonable to believe that, due to the interaction between cooling jets and mainstream, turbulent structures are created immediately downstream of the row. Consequently a peak of heat transfer would be expected. Figure B.5 also reports the results of the cases named SET1, SET2 and SET3. The apparent unphysical behavior showed between $0.22 < x/C_{ax} < 0.53$ is no more present and a unique peak appears in this zone for the modified configurations. SET1 and SET3 have an opposite behavior on pressure and suction side with respect to the experimental data. In fact, SET1 predicts more accurately the Nusselt number along the rear part of the pressure side and overestimates the heat transfer along the suction side while SET3 is closer to the experimental data along the suction side and underestimates Nusselt number in the terminal part of the pressure side. SET2 is a good compromise over the entire vane and, for this reason, it has been chosen as the definitive "improved" setting.

SET2 has also been used to reproduce the Nusselt number distribution along the midspan of the same vane geometry but in the un-cooled configuration. Grid of this case has been generated with the same settings of the 15M grid of the cooled case. Results are shown in Figure B.6. The new set of constants allows obtaining a better estimation of Nusselt number along the vane mid-span along the pressure side, if compared with the standard parameters. Along the suction side, both the versions fail in predicting Nusslet number distribution. Although this aspect, both of them move the transition position downstream with respect to the cooled case (vertical line in Figure B.6). This result is physically correct because in the un-cooled case the turbulent production induced by the cross flow interaction between main-flow and cooling jets is absent. Moreover, the modified model allows a better reproduction of the Nusselt number in the zones close to the trailing edge of the vane, especially on the suction side.

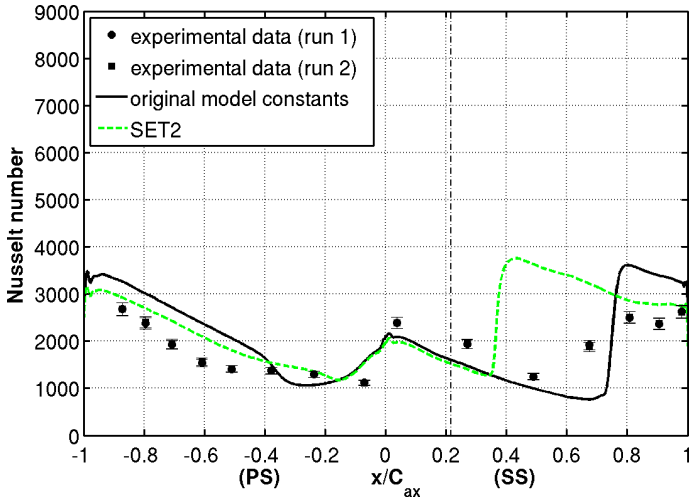


Figure B.6: Nusselt number distributions along the midspan of the un-cooled vane.

## B.3 Remarks

The re-calibration of the model proposed in this Appendix is based on purely empirical considerations related to the reproduction of experimental data of a specific case. However, as demonstrated in Chapter 5, the "improved" set of constants proved a better behavior in the reproduction of experimental data on a different geometry of film cooled vane with respect to both the fully turbulent SST $k-\omega$ model and the original version of the $k_T - k_L - \omega$ model. Nevertheless, the appropriateness of the proposed model parameters should be verified on other geometries and under different operating conditions.

# Bibliography


[1] G. Wilfert, J. Sieber, A. Rolt, N. Baker, A. Touyeras, and S. Colantuoni. New Environmental Friendly Aero Engine Core Concepts. *Proceedings of the 18th ISABE conference,Beijing, China*, 2007.

[2] Advisory Council for Aviation Research and Innovation in Europe. *Activity Summary 2013*. 2013.

[3] T. Povey, K.S. Chana, T.V. Jones, and J Hurrion. The Effect of Hot-Streaks on HP Vane Surface and Endwall Heat Transfer: An Experimental and Numerical Study. *Journal of Turbomachinery*, 129:32–43, 2007.

[4] J. Ong and R.J. Miller. Hot Streaks and Vane Coolant Migration in a Downstream Rotor. *J. Turbomach.*, 134(5), 2012.

[5] S. Shahpar and S. Caloni. Aerodynamic Optimization of High Pressure Turbines for Lean-Burn Combustion System. *ASME Paper No. GT2012-69228*, 2012.

[6] C. M. Cha, S. Hong, P. T. Ireland, P. Denman, and V. Savarianandam. Experimental and Numerical Investigation of Combustor-Turbine Interaction Using an Isothermal,Nonreacting Tracer. *Journal of Engineering for Gas Turbines and Power*, 134(8):081501–081501–18, August 2012.

[7] I. Qureshi, A. Beretta, and T. Povey. Effect of Simulated Combustor Temperature Nonuniformity on HP Vane and End Wall Heat Trans-

fer: an Experimental and Computational Investigation. *Journal of Engineering for Gas Turbines and Power*, 133, March 2011.

[8] C. Koupper, G. Caciolli, L. Gicquel, F. Duchaine, G. Bonneau, L. Tarchi, and B. Facchini. Development of an Engine Representative Combustor Simulator Dedicated to Hot Streak Generation. *J. Turbomach.*, 136(11):111007–10, August 2014.

[9] R.M Mathison, C.W. Haldeman, and M.G. Dunn. Aerodynamics and Heat Transfer for a Cooled One and One-Half Stage High-Pressure Turbine-Part I: Vane Inlet Temperature Profile Generation and Migration. *J. Turbomach.*, 134(1):011006–11, May 2011.

[10] M. Dunn and R. Mathison. History of Short-Duration Measurement Programs Related to Gas Turbine Heat Transfer, Aerodynamics, and Aeroperformance at Calspan and The Ohio State University. *Journal of Turbomachinery*, 136:041004–1–11, 2013.

[11] M.D. Barringer, K.A. Thole, and M.D. Polanka. Experimental Evaluation of an Inlet Profile Generator for High-Pressure Turbine Tests. *J. Turbomach*, 129:382–393, 2006.

[12] T. Povey and I. Qureshi. Developements in Hot-Streak Simulators for Turbine Testing. *Journal of Turbomachinery*, 131, 2009.

[13] M.A. Hilditch, A. Fowler, T.V. Jones, K.S. Chana, M.L.G Oldfield, R.W. Ainsworth, S.I Hogg, S.J. Anderson, and G.C Smith. Installation of a Turbine Stage in the Pyestock Isentropic Light Piston Facility. *Proceeding of the ASME Gas Turbine Conference*, 1994.

[14] T. Shang, G.R. Guenette, and A.H. Epstein. The influence of inlet temperature distortion on rotor heat transfer in a transonic turbine. *31st Joint Propulsion Conference and Exhibit*, AIAA paper 1995-3042, 1995.

[15] H.D. Joslyn and R.P. Dring. A Trace Gas Technique to Study Mixing in a Turbine Stage. *ASME Journal of Turbomachinery*, 110:38–43, 1988.

[16] R.G. Stabe, W.J. Whitney, and T.P. Moffit. Performance of a High-Work Low Aspect Ratio Turbine Tested With a Realistic Inlet Radial Temperature Profile. *20th AIAA Joint Propulsion Conference*, AIAA-84-1161, 1984.

[17] T.L. Butler, O.P. Sharma, H.D. Joslyn, and R.P. Dring. Redistribution of an Inlet Temperature Distortion in an Axial Flow Turbine Stage. *AAIA Journal of Propulsion and Power*, 5:64–71, 1989.

[18] M.M. Rai and R.P. Dring. Navier-Stokes Analysis of the Redistribution of Inlet Temperature Distorsion in a Turbine. *AIAA Journal of Propulsion and Power*, vol.6, no.3:276–282, 1990.

[19] M. Munk and R. Prim. On the Multiplicity of Steady Gas Flow Having the Same Streamline Patterns. *Proceedings of the National Academy of Science*, 33:137–141, 1947.

[20] D.J. Dorney, R.L. Davis, D.E. Edwards, and N.K. Madavan. Unsteady Analysis of Hot-Streak Migration in a Turbine Stage. *AIAA Journal of Propulsion and Power*, 8:520–529, 1992.

[21] F. Martelli, P. Adami, S. Salvadori, K.S. Chana, and L. Castillon. Aero-Thermal Study of the Unsteady Flow Field in a Transonic Gas Turbine With Inlet Temperature Distortions. *ASME Paper No. GT2008-50628*, 2008.

[22] J.L. Kerrebrock and A.A. Mikolajczack. Intra-Stator Transport of Rotor Wakes and Its Effects on Compressor Performance. *ASME J. of Eng. for Power*, 92:359–368, 1970.

[23] L. He, V. Menshikova, and B.R. Haller. Influence of Hot Streak Circumferential Length-Scale in Transonic Turbine Stage. *ASME Paper No. GT2004-53370*, 2004.

[24] I. Qureshi, A. Beretta, K.S. Chana, and T. Povey. Effect of Aggressive Inlet Swirl on Heat Transfer and Aerodynamics in an Unshrouded Transonic HP Turbine. *J. Turbomach*, 134:061023–1–11, 2012.

[25] G. Schmid and H.P. Schiffer. Numerical Investigation of Inlet Swirl in a Turbine Cascade. *ASME Paper No. GT2012-69397*, 2012.

[26] B. Khanal, L. He, J. Northall, and P. Adami. Analysis of Radial Migration of Hot-Streak in Swirling Flow Through HP Turbine Stage. *ASME Paper No. GT2012-68983*, 2012.

[27] L. Giller and P.H. Schiffer. Interactions Between the Combustor Swirl and the High Pressure Stator of a Turbine. *ASME Paper No. GT2012-69157*, 2012.

[28] Y. Hong, Q. Yanmin, R. Jing, and J. Hongde. Effect of Inlet Swirl on the Model Leading Edge of Turbine Vane. *ASME Paper No. GT2013-94471*, 2013.

[29] M.D. Turrel, P.J. Stopford, K.J. Syed, and E. Buchanan. CFD Simulation of the Flow Within and Downstream of a High-Swirl Lean Premixed Gas Turbine Combustor. *ASME Paper No. GT2004-53112*, 2004.

[30] R.W. Radomsky and K.A. Thole. Flowfield Measurements for a Highly Turbulent Flow in a Stator Vane Passage. *J. Turbomach.*, 122(2):255–262, February 1999.

[31] C. M. Cha, P. T. Ireland, P. Denman, and V. Savarianandam. Turbulence Levels are High at the Combustor-Turbine Interface. In *Proceedings of ASME Turbo Expo 2012: Turbine Technical Conference and Exposition*, 2012. GT2012-69130.

[32] B.F. Hall, K.S. Chana, and T. Povey. Design of a Non-Reacting Combustor Simulator With Swirl and Temperature Distortion with Experimental Validation. *ASME Paper No. GT2013-95499*, 2013.

[33] S. Shankaran, J.J. Alonso, M.F. Liou, and N.S. Liu. A Multi-Code-Coupling Interface for Combustor/Turbomachinery Simulations. *39th AIAA Aerospace Sciences Meeting and Exhibit*, AIAA 01-0974, 2001.

[34] J. Schlüter, H. Pitsch, P. Moin, S. Shankaran, S. Kim, and J. Alonso. Towards Multi-Component Analysis of Gas Turbines by CFD: Integration of RANS and LES Flow Solvers. *ASME Paper No. GT2003-38350*, 2003.

[35] J. Schlüter, X. Wu, S. Kim, J.J. Alonso, and H. Pitsch. Integrated RANS-LES Computations of Turbomachinery Components: Generic Compressor/Diffuser. *Center for Turbulence Research, Annual Research Briefs 2003*, pages 357–368, 2003.

[36] S. Kim, J. Schlüter, X. Wu, J.J. Alonso, and H. Pitsch. Integrated Simulations for Multi-Component Analysis of Gas Turbines:RANS Boundary Conditions. *40th AIAA/ASME/SAE/ASEE Joint Propulsion Conference and Exhibit*, AIAA Paper 2004-3415, 2004.

[37] J. Schlüter, X. Wu, E.v.d. Weide, S. Hahn, J.J. Alonso, and H. Pitsch. Multi-Code Simulations: A Generalized Coupling Approach. *17th AIAA Computational Fluid Dynamics Conference, June 43rd AIAA Aerospace Sciences Meeting and Exhibit*, AIAA Paper 2005-4997, 2005.

[38] J. Schlüter, S. Apte, G. Kaltizin, E.v.d Weide, J.J. Alonso, and H. Pitsch. Large-Scale Integrated LES-RANS Simulations of a Gas Turbine Engine. *Center for Turbulence Research, Annual Research Briefs 2005*, pages 111–120, 2005.

[39] G. Medic, G. Kalitzin, D. You, M. Herrmann, F. Ham, E.v.d. Weide, H. Pitsch, and J.J. Alonso. Integrated RANS/LES Computations of Turbulent Flow Through a Turbofan Jet Engine. *Center for Turbulence Research, Annual Research Briefs 2006*, pages 275–285, 2006.

[40] G. Medic, D. You, and G. Kalitzin. An Approach for Coupling RANS and LES in Integrated Computations of Jet Engines. *Center for Turbulence Research, Annual Research Briefs 2006*, pages 287–298, 2006.

[41] E.V. Klapdor. Simulation of Combustor-Turbine Interaction in a Jet Engine. PhD thesis, TU Darmstadt, Institut für Energie und Kraftwerkstechnik, 2011.

[42] E.V. Klapdor, F. di Mare, W. Kollmann, and J. Janicka. A Compressible Pressure-based Solution Algorithm for Gas Turbine Combustion Chambers Using the PDF/FGM Model. *Flow, Turbulence and Combustion*, 91(2):209–247, 2013. ISSN 1386-6184. doi: 10.1007/s10494-013-9451-2.

[43] E. Collado Morata. Impact of the Unsteady Aerothermal Environment on the Turbine Blades Temperature . PhD thesis, Institut National Polytechnique de Toulouse, 2012.

[44] F. Martelli and P. Adami. Recent Developements in Numerical Methods for Turbomachinery Flows. In *Lecture Series 2001-2002*. Von Karman Institute for Fluid Dynamics, 2001.

[45] E. Belardini, P. Adami, and F. Martelli. Developement of an Unsteady Parallel Approach for 3D Stator Rotor Interacion. In *Science and Supercomputing at CINECA*, Report 2001.

[46] *ANSYS® Fluent Theory Guide, Release 15.0*. 2013.

[47] *ANSYS® Fluent UDF Manual, Release 15.0*. 2013.

[48] *ANSYS® Fluent User's Guide, Release 15.0*. 2013.

[49] F. Menter and Y. Egorov. The Scale-Adaptive Simulation Method for Unsteady Turbulent Flow Predictions. Part 1: Theory and Model Description. *Journal Flow Turbulence and Combustion*, 85:113–138, 2010.

[50] F.R. Menter. Two-Equation Eddy-Viscosity Turbulence Models for Engineering Applications. *AIAA Journal*, 8:1598–1605, 1994.

[51] S.B. Pope. Ten Questions Concerning the Large-Eddy Simulation of Turbulent Flows. *New Journal of Physics*, 6:1–24, 2004.

[52] J.T. Salmon, T.J. Bogar, and M. Sajben. Laser Doppler Velocimeter Measurements in Unsteady, Separated Transonic Diffuser Flows. *AIAA*, 21(12):1690–1697, 1983.

[53] NASA 2008. NPARC Alliance Verification and Validation Archive. `http://www.grc.nasa.gov/WWW/wind/valid/transdif/transdif.html`.

[54] Centaur$^{TM}$. *CentaurSoft*. `http://www.centaursoft.com/`.

[55] D.C. Wilcox. Turbulence modeling for CFD. DCW Industries, Inc. La Canada, California, 1998.

[56] C.H. Sieverding, H. Richard, and J.-M. Desse. Turbine Blade Trailing Edge Flow Characteristics at High Subsonic Outlet Mach Number. *J. Turbomach.*, 125(2):298–309, April 2003.

[57] G. Cicatelli and C.H. Sieverding. The Effect of Vortex Shedding on the Unsteady Pressure Distribution Around the Trailing Edge of a Turbine Blade. *J. Turbomach.*, 119(4):810–819, October 1997.

[58] T. Léonard, F. Duchaine, N. Gourdain, and L.Y.M. Gicquel. Steady/Unsteady Reynolds Averaged Navier-Stokes and Large Eddy Simulations of a Turbine Blade at High Subsonic Outlet Mach Number. *ASME Paper No. GT2010-22469*, 2010.

[59] A. Gehrer, H. Lang, N. Mayrhofer, and J. Woisetschläger. Numerical and Experimental Investigation of Trailing Edge Vortex Shedding Downstream of a Linear Turbine Cascade. *ASME Paper No. 2000-GT-434*, 2000.

[60] K.W. Thompson. Time Dependent Boundary Conditions for Hyperbolic Systems. *Journal of Computational Physics*, 68(1):1–24, January 1987.

[61] J. Nordström. The Use of Characteristic Boundary Conditions for the Navier-Stokes Equations. *Computer and Fluids*, 24(5):609–623, June 1995.

[62] G. Lodato, P. Domingo, and L. Vervisch. Three-Dimensional Boundary Conditions for Direct and Large-Eddy Simulation of Compressible Viscous Flows. *Journal of Computational Physics*, 227(10):5105–5143, May 2008.

[63] S. Vagnoli and T. Verstraete. A New Method for Zonal LES-URANS Computations with Exchange of Information Between Different Codes. *Proceedings of the 6th European Conference on Computational Fluid Dynamics (ECFD VI), 20-25 July 2014, Barcelona, Spain*, 2014.

[64] F. Mathey, D. Cokjlat, J.P. Bertoglio, and E. Sergent. Specification of LES Inlet Boundary Condition Using Vortex Method. *Turb. Heat Mass Transfer*, 4, 2003.

[65] F. R. Menter. *Best Practice: Scale-Resolving Simulations in ANSYS CFD.* ANSYS, version 1.0 edition, 2012.

[66] S. Salvadori, F. Montomoli, F. Martelli, K.S. Chana, I. Qureshi, and T. Povey. Analysis on the Effect of a Non-Uniform Inlet Profile on Heat Transfer and Fluid Flow in Turbine Stages. *ASME Paper No. GT2010-23526*, 2010.

[67] M. Insinna, S. Salvadori, and F. Martelli. Simulation of Combustor/NGV Interaction Using Coupled RANS Solvers: Validation and Application to a Realistic Test Case. *ASME Paper No. GT2014-25433*, 2014.

[68] A. Andreini, G. Caciolli, B. Facchini, and L. Tarchi. Experimental Evaluation of the Density Ratio Effects on the Cooling Performance of a Combined Slot/Effusion Combustor Cooling System. *ISRN Aerospace Engineering*, Article ID 423190, 2013.

[69] S. Mendez and F. Nicoud. Adiabatic Homogeneous Model for Flow Around a Multiperforated Plate. *AIAA Journal*, 46:2623–2633, 2008.

[70] Turbine Aero-Thermal External Flows 2. TATEF2. `http://ec.europa.eu/research/transport/projects/items/tatef_2_en.htm`.

[71] S.L. Dixon. *Fluid Mechanics and Thermodynamics of Turbomachinery*. ELSEVIER Butterworth Heinemann, fifth edition, 2005.

[72] M.A.Hilditch, G.C. Smith, and K.S. Chana. Measurements and Predictions of Endwall Heat Transfer in Two High Pressure Turbines. *RTO AVT Symposium on ""Advanced Flow Management: Part B - Heat Transfer and Cooling in Propulsion and Power Systems"*, 2001.

[73] P.F. Beard, T. Povey, and P.T. Ireland. Mass Flow Rate Measurement in a Transonic Turbine Test Facility with Temperature Distortion and Swirl. *journal of Flow Measurement and Instrumentation*, 19:315–324, 2008.

[74] S. Salvadori, F. Montomoli, F. Martelli, K.S. Chana, I. Qureshi, and T. Povey. Analysis on the Effect of a Nonuniform Inlet Profile on Heat Transfer and Fluid Flow in Turbine Stages. *Journal of Turbomachinery*, 134(1):011012.1–0.011012.14, 2012.

[75] N. Peters. Fifteen Lectures on Laminar and Turbulent Combustion. ERCOFTAC Summer School. September 14-28, 1992.

[76] S.M. Correa. Turbulence-Chemistry Interactions in the Intermediate Regime of Premixed Combustion. *Combustion and Flame*, 93:41–60.

[77] V. Zimont, W. Polifke, M. Bettelini, and W. Weisenstein. An Efficient Computational Model for Premixed Turbulent Combustion at High Reynolds Numbers Based on a Turbulent Flame Speed Closure. *J. of Gas Turbines Power*, 120:526–532, 1998.

[78] E. M. Greitzer, C. S. Tan, and M. B. Graf. *Internal Flow: Concepts and Applications*. Cambridge University Press, 2004.

[79] D. You, F. Ham, and P. Moin. Large-Eddy Simulation Analysis of Turbulent Combustion in a Gas Turbine Engine Combustor. *Center for Turbulence Research, Annual Research Briefs 2008*, pages 219–230, 2008.

[80] P. Beard, A. Smith, and T. Povey. Impact of Severe Temperature Distortions on Turbine Efficiency. *Journal of Turbomachinery*, 135 (1):011018–12, 2012.

[81] M. Jonsson and P. Ott. Heat Transfer Experiments on a Heavily Film Cooled Nozzle Guide Vane. *Proc. of the Seventh European Conference on Turbomachinery - Fluid Dynamics and Thermodynamics, March 5-9, Athens, Greece*, pages 1011–1020, 2007.

[82] D. Charbonnier, P. Ott, M. Jonnson, T. Köbke, and F. Cottier. Comparison of Numerical Investigations with Measured Heat Transfer Performance of a Film Cooled Turbine Vane. *ASME Paper No. GT2008-50623*, 2008.

[83] D.K. Walters and D. Cokljat. A Three-Equation Eddy-Viscosity Model for Reynolds-Averaged Navier-Stokes Simulations of Transitional Flow. *ASME Journal of Fluids Engineering*, 130:121401–1/13, 2008.

[84] P.J. Roache, N.G. Kirti, and F. M. White. Editorial Policy Statement on the Control of Numerical Accuracy. *J. Fluids Eng.*, 108, 1986.

[85] M. Insinna, D. Griffini, S. Salvadori, and F. Martelli. Film Cooling Performance in a Transonic High-Pressure Vane: Decoupled Simulation and Conjugate Heat Transfer Analysis. *Energy Procedia*, 45: 1126–1135, 2014.

[86] M. Insinna, D. Griffini, S. Salvadori, and F. Martelli. Conjugate Heat Transfer Analysis of a Film Cooled High-Pressure Turbine Vane Under Realistic Combustor Exit Flow Conditions. *ASME Paper No. GT2014-25280*, 2014.

[87] S. Salvadori, F. Montomoli, F. Martelli, P. Adami, and L. Castillon. Aerothermal Study of the Unsteady Flow Field in a Transonic Gas Turbine With Inlet Temperature Distortions. *Journal of Turbomachinery*, 133(3):031030–1–13, 2011.

[88] *ANSYS® CFX-Solver Theory Guide, Release 14.5.* 2012.

[89] R.B. Langtry and F.R. Menter. Transition Modeling for General CFD Applications in Aeronautics. *AIAA paper 2005-522*, 2005.

[90] G. Wang, F. Duchaine, D. Papadogiannis, I. Duran, Stéphane Moreau, and F.Y.M. Gicquel. An Overset Grid Method for Large Eddy Simulation of Turbomachinery Stages. *Journal of Computational Physics*, 274:333–355, 2014.

[91] *ANSYS® CFX-Solver Modeling Guide, Release 14.5.* 2012.

[92] Zhong-Nan Wang and Xin Yuan. Concurrent Effects of Hot Streak and Gas Species Concentration on Aerothermal Characteristics in a Turbine stage. *ASME Paper No. GT2012-69283*, 2012.

[93] K.S. Chana and A.H. Mole. *Summary of Cooled NGV and Un-cooled Rotor Measurements from the MT1 Single Stage High Pressure Turbine in the DERA Isentropic Light Piston Facility.* Brite-EuRam TATEF project (BRPR-CT97-0519), 2002.

[94] K.S. Chana and U. Singh. A Programme to Investigate the Effects of Film Cooling in a High-Pressure Aeroengine Turbine Stage. *Proc. of the Sixth European Conference on Turbomachinery - Fluid Dynamics and Thermodynamics, Lille, France*, 2005.